High Resolution Flow and Ion Temperature Measurements with Ion Doppler Spectroscopy at SSX

Jerome Fung

March 9, 2006

Abstract

The Swarthmore Spheromak Experiment (SSX) studies magnetic reconnection by merging co- and counter-helicity spheromaks. Typical plasma parameters include electron density $n_e \sim 10^{15}$ cm^{-3}, temperature $T_i + T_e \sim 30$ eV, and magnetic fields $|B| \sim 0.1$ T. This thesis documents the construction of a new high-resolution ion Doppler spectroscopy (IDS) diagnostic. The SSX IDS system features a 1.33 m Czerny-Turner spectrometer with a 316 grooves/mm echelle grating and a 32-channel photomultiplier tube array. On any shot, we can observe any of 10 different chords through the plasma with submicrosecond time resolution and an instrument temperature ~ 3 eV. Current studies have focused on the evolution of the carbon III 229.687 nm line which we observe at 25th order, with dispersion 0.0085 nm/mm using $3.7\times$ magnifying exit optics. We have determined the time dependence of flow velocities and ion temperatures in the plasma. We have also performed Abel inversions to determine radial profiles of the plasma emissivity. In addition, we have observed near-Alfvènic bi-directional flows due to reconnection. These results, as well as a possible model for the flows based on shear, are presented.

Contents

Chapter 1

Introduction

The study of plasmas, the most abundant state of visible matter in the Universe, is exceedingly rich; understanding of some of their basic properties and behaviors remains elusive. One such phenomenon in plasma physics is magnetic reconnection. This thesis will focus on experiments conducted at the Swarthmore Spheromak Experiment (SSX) that investigate the reconnection process. Specifically, this thesis documents optical upgrades to our ion Doppler spectroscopy (IDS) and reports flow and ion temperature measurements with good time and spectral resolution from the IDS system.

Before delving into the details of the IDS system and of the plasmas it investigates, we summarize, for the benefit of readers unfamiliar with plasma physics, some basic plasma properties and parameters. This will be the subject of the next section.

1.1   Plasmas

Plasmas may be loosely defined as ionized gases, heated so hot that some of the gas molecules have their outer electrons stripped off. However, this definition of a plasma as an ionized gas is not entirely satisfactory. How ionized does a gas have to be to be considered a plasma? What about restrictions on density and temperature? And furthermore, what is so special about a plasma? Our subsequent discussion follows Chen [1].

Plasmas are generally considered to consist of both ionized and neutral particles; in many laboratory plasmas in the laboratory, for instance, most of the gas particles are neutral[1]. There must be enough charged particles, however, for the plasma to have enough mobile charge carriers to permit macroscopic currents and magnetic fields. It is precisely the macroscopic electrical and magnetic properties of plasmas that distinguish them from ordinary gases and make their behavior both much richer and much more difficult to study.

One of the most important defining properties of plasmas is that of Debye shielding. Imagine introducing a lone electron into a room full of ordinary air. The electric field of the electron would drop off as $1/r^2$, but its electrical influence would be felt throughout the room. In contrast, there are no large-scale electrostatic

---

[1]The SSX plasmas are mostly ionized.

fields in the bulk volume of a plasma[2]. Rather, positive ions would tend to drift around the lone electron, shielding off its electrical influence. This phenomenon is known as Debye shielding. Assuming that the ions are massive and that the energy distribution of electrons is governed by Boltzmann statistics, it may be shown [2] from Poisson's equation ($\nabla^2 V = -\rho/\epsilon_0$) that in one dimension, the electric potential V of a charged body decreases with the distance x from the body as

$$V \propto \exp(-x/\lambda_D) \tag{1.1}$$

where the Debye length λ_D is given by

$$\lambda_D^2 = \frac{\epsilon_0 k T_e}{n e^2}. \tag{1.2}$$

Here k is Boltzmann's constant, T_e is the plasma electron temperature, and n is the plasma electron density. For reference, we note that in plasma physics, the temperatures are defined as the width of the Maxwellian velocity distribution of the appropriate species (electrons or ions), and as kT are commonly expressed in electron volts. Many books on plasmas suppress Boltzmann's constant and mean kT when they write T. We will not adopt this potentially confusing convention here; in all equations arising in this thesis, we will explicitly include k, but we will freely refer to measurements of T_i or T_e in eV.

For Debye shielding to be meaningful, we must have enough mobile charged particles. This leads us to two useful criteria for a plasma: first, that there be a large ($\gg 1$) number of charged particles in the volume of a Debye sphere, or an imaginary sphere whose radius is a Debye length. Secondly, we also require that λ_D be much smaller than the length scale of the plasma.

One final requirement [1] is that the dynamics of the plasma not be dominated by collisions with neutral particles, as they would be in an ordinary gas.

The reader may ask why, aside from their electromagnetic properties, plasmas are worth studying. One of the best answers is their ubiquity. Plasmas are very important in nuclear fusion research, are omnipresent in astrophysics, and have diverse practical applications on earth.

It is well known that the Earth's supplies of fossil fuels are limited and that there may eventually be critical shortages thereof. Moreover, pollution from burning fossil fuels may be causing serious environmental problems like global warming. Energy from nuclear fusion would, in contrast, would be virtually limitless and would result in less pollution than producing energy from burning fuels or from nuclear fission. To date, however, commercially viable fusion has not yet been achieved, not due to a lack of understanding of fusion, but due to our lack of understanding of plasma physics. Fusing hydrogen, whether on earth or in the stars, requires a hot, dense, ionized gas – a plasma. Thus far we have not succeeded in controlling plasma instabilities and sufficiently confining a fusion plasma to obtain a prolonged positive energy output.

Plasmas are even more important in astrophysics. Stars, the best example of successful fusion reactors, are made of plasma, and understanding their behavior inevitably requires some understanding of plasmas. Furthermore, a diffuse plasma is present in the interstellar medium. Many other astronomical phenomena,

---

[2]There can be inductive electric fields (due to $\frac{\partial \mathbf{B}}{\partial t}$), however.

Figure 1.1: Tangled loops of plasma following a solar flare. Image taken at 17.1 nm by the TRACE (Transition Region And Coronal Explorer) satellite. Figure from `http://trace.lmsal.com`.

such as observed variations in the rings of Saturn, may be attributable to plasmas. Closer to earth, the plasma in the solar wind, the stream of charged particles coming towards the earth from the sun, can dramatically affect global communications during periods of solar activity. Another example of plasmas near earth is in the Van Allen radiation belts, where the earth's magnetic field confines a plasma [1]. Plasma is also found in the ionosphere, which is the outer layer of the earth's atmosphere; the ionosphere is important in facilitating long-range radio communications [3]. Lightning and auroras are yet further examples of naturally occurring plasmas.

Lastly, we should not neglect the practical uses of plasmas. Perhaps the most common use of plasmas formed in gas discharges is in fluorescent light bulbs and other lights, such as neon signs, that rely on glowing gases. The gas laser uses a glow discharge as the lasing medium; the common helium-neon (HeNe) laser is perhaps the best-known example of this type [1]. Plasmas are also finding use in industrial manufacturing processes, particularly in the etching of semiconductors.

Having a sense of why plasmas are worth studying, the reader might well ask why the study of plasmas is so difficult, for are not the laws of classical mechanics and electrodynamics well-established and understood? For even a cubic centimeter of a laboratory plasma which might contain $\sim 10^{15}$ charged particles, it would be both computationally impossible and not very instructive to try to account for all the electromagnetic forces on each particle and then apply Newton's second law. As with the study of even ordinary gases, then, only some type of statistical or macroscopic theory can hope to be analytically tractable. Plasma kinetic theory deals with the former, but it can be extremely difficult to apply to the turbulent, nonequilibrium, and

often nonlinear conditions commonly found in plasmas. In the other approach, just as one might apply fluid mechanics to the study of an ordinary gas, one can apply a fluid theory to plasmas. This theory is called magnetohydrodynamics (MHD) and essentially combines classical electromagnetism with fluid dynamics. We will address MHD more fully later in this thesis, but for now it suffices to remark that as a theory, MHD is not always satisfactory. Thus theoretical, computational, and experimental researches in plasma physics continue.

1.2   The Problem of Magnetic Reconnection

Here, we shall qualitatively describe the problem that lies at the heart of research efforts at SSX: magnetic reconnection. The quantitative details will be deferred to later chapters; the goal here is to give the reader a general sense of the physical problems at hand.

We have already mentioned that plasmas can carry magnetic fields. In ideal MHD, where the plasma is assumed to be a perfectly conducting fluid, we will show in a later Chapter that the magnetic field lines convect with the fluid; this is the so-called frozen-in flux condition. Consider two segments of fluid carrying oppositely directed magnetic fields $\mathbf{B}$ that are moving towards each other. Since magnetic field is a vector, should the frozen-in flux condition hold, one might naïvely expect an arbitrarily large gradient of $\mathbf{B}$ to form when the segments of fluid meet. Ideal MHD is only an idealization, however, and what really happens is that the oppositely directed field lines change their topology, come together, and reconnect. In the reconnection process, the overall amount of magnetic field decreases, and so some of the magnetic energy ($B^2/2\mu_0$) is dissipated. Where this energy goes is one of the questions the research at SSX is seeking to answer. We know that some of the magnetic energy goes into kinetic energy (flow of the plasma) and heating the plasma. A diagram of this process is shown in Fig. 1.2. Chapter 4 will discuss spheromaks and how we use them to study reconnection at SSX in more detail.

Magnetic reconnection is a direct implication of the breakdown of ideal MHD. Theoretically, this can be addressed by dropping the idealized assumption that the plasma has no resistivity, for a real plasma will have a resistivity from collisions. The earliest and simplest model of reconnection, called the Sweet-Parker model, assumes a resistive plasma.

There are two particularly glaring problems with the Sweet-Parker model, however. It is a two-dimensional theory in that it assumes reconnection to only be occurring in a plane. This is problematic because experimental observations, including previous measurements in SSX [4, 5], clearly indicate that magnetic reconnection is a 3D process. Another serious problem with the Sweet-Parker theory is that the reconnection rate it predicts is too slow. The rate of magnetic reconnection has been measured in solar flares [6, 7], but the rate predicted by the Sweet-Parker model is orders of magnitude slower than measured [4]. Although the Sweet-Parker model does not include all the physics that now appears to be necessary to model reconnection, it remains conceptually useful and so we will discuss it in some detail later.
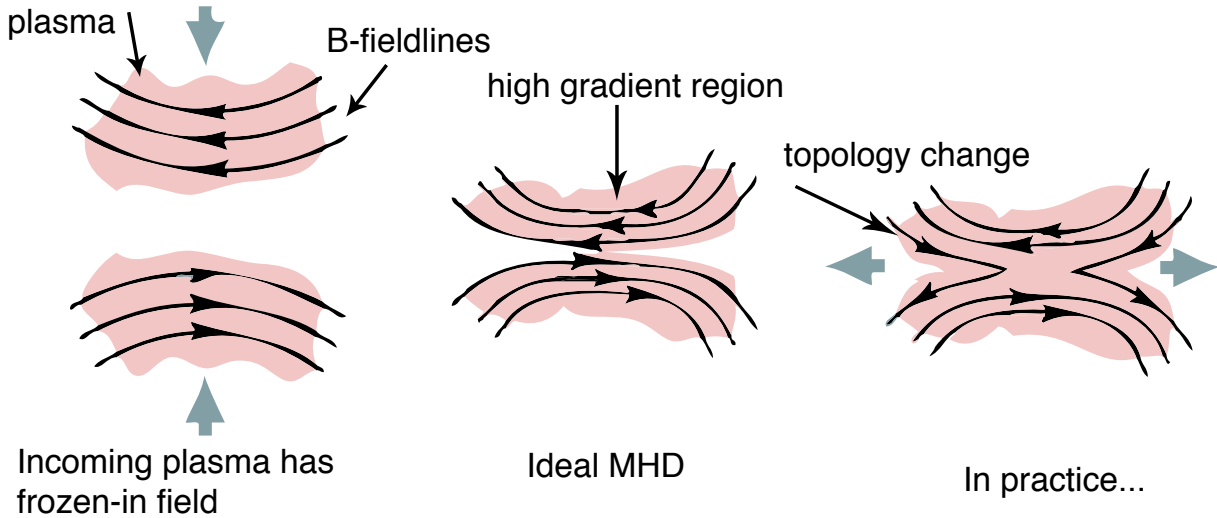
Figure 1.2: Conceptual picture of the magnetic reconnection process. Figure from [4].

1.3 A New Diagnostic: Ion Doppler Spectroscopy

A new diagnostic that will help answer some of the questions about reconnection that SSX is studying has recently been installed. This is the ion Doppler spectroscopy (IDS) system. The IDS measures the ion temperature and plasma flow velocity averaged along any of 10 chords through the plasma. While the details are deferred to a later chapter, it suffices to say for now that the IDS measures flow by observing the Doppler shift of an impurity spectral line, and measures ion temperature by observing the Doppler broadening of the impurity line. The IDS should allow improved, nonperturbative measurements of flow and temperature in SSX, which have only previously been measured using probes.

1.4 Astrophysical Observations of Reconnection

Here we briefly discuss observations of magnetic reconnection in space. Reconnection has been observed by the satellites Polar and Cluster in the Earth's magnetopause and magnetotail, respectively. The reader interested in the comparison of data from these space observations to laboratory results at SSX is referred to [8]. Here, however, we discuss in some more detail an important observation of bi-directional flow in the solar corona due to magnetic reconnection. First, though, let us introduce the solar corona.

1.4.1 Solar Corona

Magnetic reconnection plays a role in a number of phenomena in the solar corona, which is the outermost of the three layers of the "atmosphere" of the sun, above the photosphere, from which most of the sun's visible light is emitted, and the chromosphere. In the corona, the plasma density ranges from 10^7–10^{15} m^{-3}, with higher densities nearest the surface of the sun, and temperatures reach up to 170 eV[9]. The temperature

in the corona is notable because the plasma temperature is only about ~ 0.4 eV in the photosphere [9]. Magnetic reconnection is one possible mechanism for heating the corona. In particular, reconnection might occur between current sheets as the coronal plasma evolves to minimize its energy; this possibility has been confirmed by MHD simulations, such as those of Mikik *et al* [10].

Solar prominences are stable loops of cooler, dense plasma erupting above the corona that are often accompanied by coronal mass ejections. One possible theory proposed by Priest is that coronal prominences involve twisting tubes of magnetic flux that violently erupt [11]. Again, magnetic reconnection may be involved here.

X-ray telescopes have allowed dramatic observations of solar flares, during which magnetic reconnection is believed to occur. As the loop of plasma in a solar flare gets stretched out above the surface of the corona, the field lines get stretched out, break apart, and then reconnect [9]. It was actually the study of solar flares motivated the first theory of magnetic reconnection, that of Sweet and Parker.

One particularly relevant set of observations have been those of D. E. Innes *et al* [12, 13]. They made observations of the Si IV 139.3 nm emission line with the ultraviolet spectrometer SUMER (Solar Ultraviolet Measurements of Emitted Radiation) on the satellite SOHO (Solar and Heliospheric Observatory), located at the Lagrange point L1. SUMER observed small but explosive events such as microflares, which had previously been thought to be associated with reconnection. During scanning, SUMER's slit, which was oriented in the north-south direction of the solar disk, was rastered east and west. The instrument had a resolution of ~ 1 arcsec, corresponding to 715 km on the sun. Observations were made both at the center of the solar disk and at $60°$ latitude. SUMER essentially functions like our IDS system.

An example of the measurements made by SUMER is shown in Fig. 1.3. The composite image shows a series of spectra scanned horizontally in position and with time running vertically. Looking at any one vertical column (spatial position), such as the third from the left, one can see plasma first being blueshifted and then from about 120-180 seconds being both blueshifted and redshifted.

At both positions on the sun, the spectral line was observed to be simultaneously redshifted and blueshifted. The double-peaked lineshapes persisted for well over 1 minute. Innes proposed that their observations were due to bi-directional jets in the corona. Although they could not make simultaneous measurements of reconnecting magnetic fields, such bi-directional flows would be consistent with the Alfvénic outflows due to reconnection.

1.5   Previous Laboratory Reconnection Experiments

Here we review several prior laboratory studies of magnetic reconnection. We particularly focus on the UCLA experiment of Stenzel and Gekelman, the TS-3 experiment at the University of Tokyo, and the MRX experiment at Princeton. But we will defer the discussion of prior work on reconnection at SSX to Chapter 4.
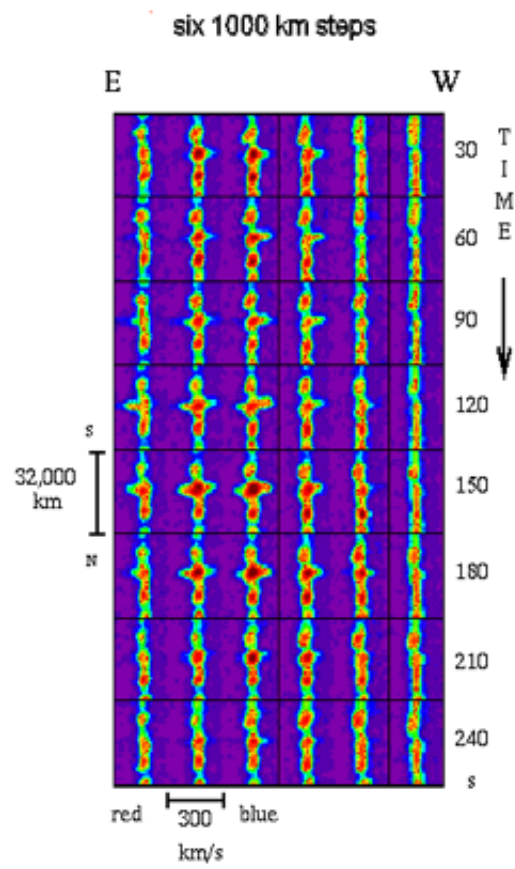
Figure 1.3: Sample of data from the SUMER spectrometer. Details are in the text; figure from [12].
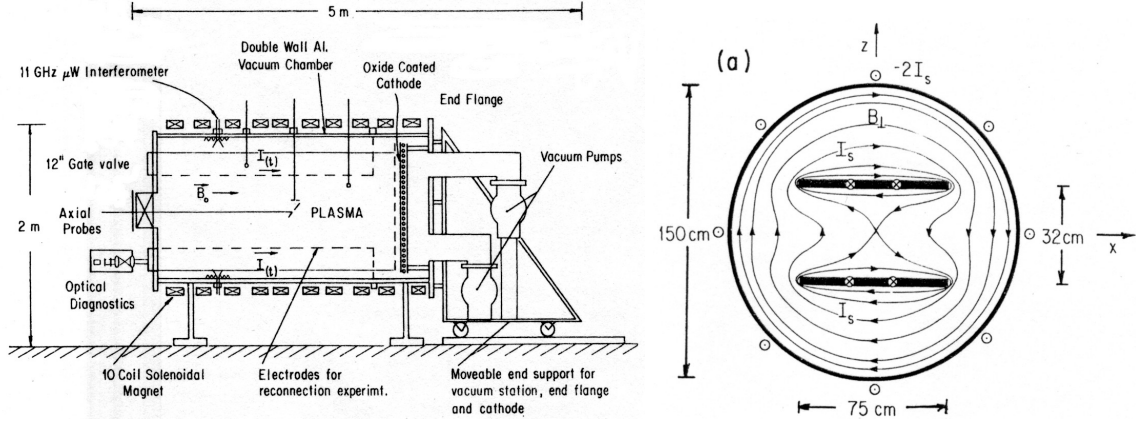
Figure 1.4: Left): Side view schematic of UCLA experiment. Right): Axial view of UCLA experiment. Magnetic field lines shown are vacuum fields, without plasma present. Figures from [14].
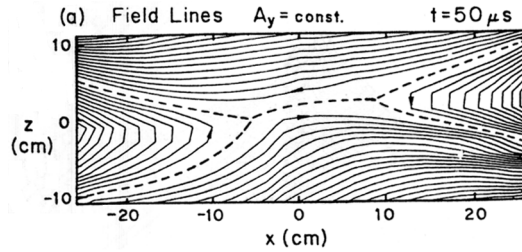
Figure 1.5: Magnetic field lines in a cross-sectional plane of the UCLA plasma. Note the resemblance of the field lines to the initial conditions of the Sweet-Parker model. Figure from [14].

1.5.1 UCLA Experiment

One of the first laboratory studies of magnetic reconnection was conducted by Stenzel and Gekelman at UCLA in the early 1980's [14]. They studied a cylindrically symmetric plasma 2 m long and $\sim$1 m in diameter [15]. A schematic of the experiment, showing a side view and an axial view is shown in Fig. 1.4. Typical plasma parameters included electron density $n_e \simeq 10^{12}$ cm^{-3}, electron temperature $T_e \simeq 5$ eV, ion temperature $T_i \simeq 0.5$ eV, magnetic fields $B \simeq 20$ G, and magnetic Reynolds number $R_m \simeq 20$ [14].

Stenzel and Gekelman created an X-type reconnection geometry in their experiment and performed detailed studies of the reconnection magnetic fields, temperatures, and flows. Rather than measuring everything at once, they made their plasma reproducible and moved their probes around from shot to shot. They also averaged together 10 shots per data point. This allowed the effective measurement of the general, average picture from reconnection, but would have averaged out local fluctuations. Magnetic structure corresponding to the Sweet-Parker model was measured; one set of field lines is shown in Fig. 1.5. In addition, using electrostatic probes, Stenzel and Gekelman measured a Sweet-Parker like flow pattern with near-Alfvénic outflows. Notably, Stenzel and Gekelman were able to measure every term in the generalized Ohm's law except for the resistivity; they were thus able to calculate the resistivity. When they compared their calculated

10
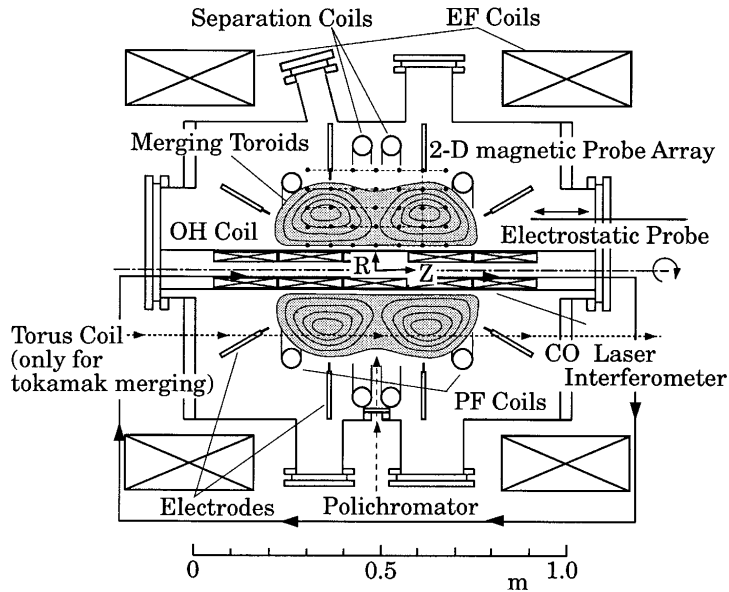
Figure 1.6: Side view schematic diagram of the TS-3 experiment. Note the central core as well as the midplane polychromator. Figure from [18].

resistivity to the classical Spitzer resistivity from collisions, they sometimes found their plasma resistivity to be as much as 200 times larger than the Spitzer resistivity. The anomalous resistivity that they measured would likely have come from small-scale instabilities and fluctuations in the plasma – which their measuring techniques, dependent on averaging, would not have been able to observe. Moreover, only the electrons in the plasma were magnetized – the ion gyroradii were sufficiently large that the ions tended to collide with the walls or electrodes before gyrating around a field line. The relatively low magnetic Reynolds number of the UCLA experiment also limited the applicability of its results to many space plasmas of interest. Hence, while the results of Stenzel and Gekelman were pioneering, more experimental studies were necessary.

1.5.2 Tokyo TS-3 Experiment

The TS-3 experiment at the University of Tokyo [16, 17, 18] came online in the early 1990's and studied reconnection in a very different way. It was consequently able to better study some aspects of reconnection physics than the UCLA experiment. Primary findings included the importance of the third dimension in reconnection, the importance of global plasma parameters as well as local parameters, significant ion heating, and the acceleration of fast individual ions due to reconnection.

TS-3 was a cylindrical device that coaxially merged toroidal plasmas such as spheromaks. Typical plasma parameters were $n_e \sim 3 \times 10^{14}$ cm^{-3}, $T_e \sim 10$ eV, $B \sim 0.5 - 1.0$ kG, and Lundquist number $S \sim 300$ [16]. Their plasmas were solidly in the MHD regime, with both the electrons and ions magnetized. A schematic diagram of the experiment is shown in Fig. 1.6. Their spheromak merging experiments (they were also able to merge tokamaks or reversed field pinches) were very similar to the experiments done at SSX. It is important

11
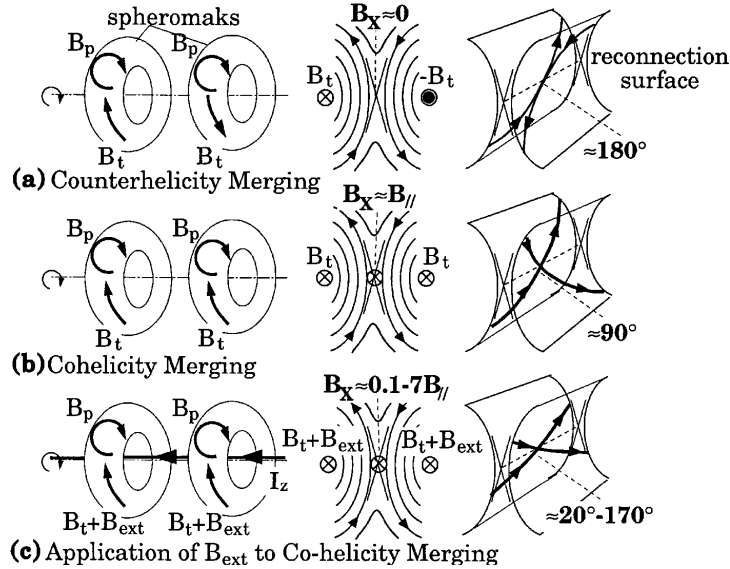
Figure 1.7: Reconnection geometries for counter- and co-helicity merging at TS-3. While reconnection looks similar in local 2D planes, the fields are globally different for counter-helicity merging, co-helicity merging, and co-helicity merging with external field. Note in the latter 2 cases the variable angle of the reconnecting fields and the substantial out-of-plane field components, B_X. Figure from [18].

to note, however, that TS-3 had a central column solenoid to help stabilize their toroids. Ono *et al.* were able to independently control the helicity of the two toroids they were merging. Thus, they could perform counter-helicity as well as co-helicity merging experiments. In both cases, there were similar 2D "slices" where the reconnecting poloidal fields formed a Sweet-Parker like reconnection region. But in co-helicity merging, they could vary the angle of the reconnecting fields by applying an external toroidal field, such that the fields had a substantial out-of-plane component, as large as 70% of the total field strength [18]. Thus, TS-3 was able to study the 3D effects in reconnection. A picture of the differing reconnection geometries is shown in Fig. 1.7.

Diagnostics on TS-3 included a 2D magnetic probe array in an r-z plane as well as a polychromator at the midplane that observed H_β and C_{II} spectral lines. This allowed the measurement of radial profiles of ion temperature and velocity. It was found that the reconnection rate strongly depended on the strength of the out-of-plane field component; the stronger this component, the slower the reconnection rate. They also found that the reconnection rate depended on the speed with which the toroids were accelerated towards each other [18]. Other significant findings of the TS-3 experiment included marked ion heating and acceleration. Through measuring the Doppler width of the spectral lines observed by the polychromator, ion heating of up to 200 eV was measured. Through observing Doppler shifts, near-Alfvénic ion speeds were measured, indicating that the kinetic energy of ions was a significant outlet for the magnetic energy dissipated by reconnection.

More recently, the researchers at Tokyo have constructed an upgrade to their experiment, TS-4. Thus
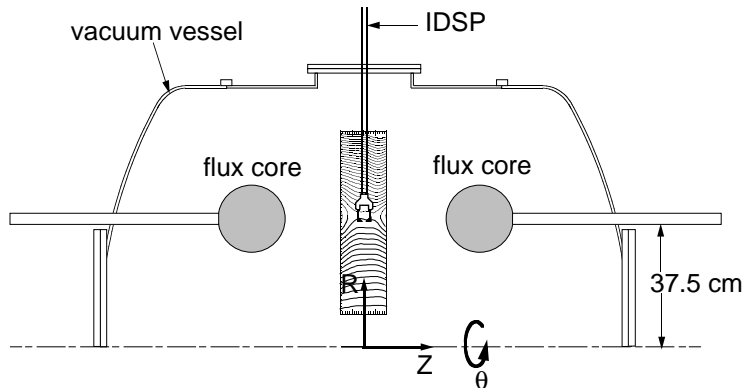
Figure 1.8: Schematic diagram of MRX. The MRX is rotationally symmetric about the dashed line at the bottom, which is the central axis. The location of the flux cores in an $r-z$ plane is shown in grey. Note the position of the Ion Dynamics Spectroscopy Probe (IDSP). Figure from [26].

far TS-4 has conducted studies of sheared flow in FRC's formed through spheromak merging [19].

1.5.3 Princeton MRX Experiment

The Magnetic Reconnection Experiment (MRX) came online at the Princeton Plasma Physics Laboratory in 1995 and was the next important laboratory device for studying reconnection [20]. The configuration of MRX was similar to TS-3. We first describe the setup and reconnection geometry of MRX, before briefly discussing the physics it has revealed. In particular, MRX has tested the Sweet-Parker model and found that their measured reconnection rates agree with a *modified* Sweet-Parker model incorporating more effects, such as enhanced resistivity [21, 22]. Also, MRX has conducted detailed studies of ion heating and flow with an Ion Dynamics Spectroscopy Probe [23, 24].

Like TS-3, MRX forms and merges a pair of toroidal plasmas. Typical plasma parameters include $n_e \sim 0.5 - 1 \times 10^{14}$ cm^{-3}, $T_e \sim 5 - 20$ eV, $B \sim 0.5 - 1$ kG, and Lundquist number $S \sim 500$ [25]. The plasmas are formed in a cylindrical vacuum chamber with the reconnecting fields formed by a pair of coaxial "flux cores", as shown in Fig. 1.8. The flux cores contain coils which generate toroidal and poloidal magnetic fields. The fields generated by the flux cores can be thought of as dividable between "private flux" pertaining to each individual toroid as well as "public flux" belonging to both. By first increasing the toroidal fields and then decreasing the poloidal fields, MRX is capable of generating "push-pull" reconnection in which the private flux of the two toroids is pushed together into the public region and then pulled back towards the individual toroids [26]. The reconnection sequence is shown in Fig. 1.9. It is the pull reconnection phase, in which a Sweet-Parker-like geometry is formed, that has been most extensively studied. The MRX group is capable of performing null-helicity, co-helicity, and counter-helicity merging and thus can vary the angle of the reconnecting fields, much like TS-3. Early experiments confirmed the findings of TS-3 concerning the dependence of the reconnection rate on the angle of the merging fields [20].

13
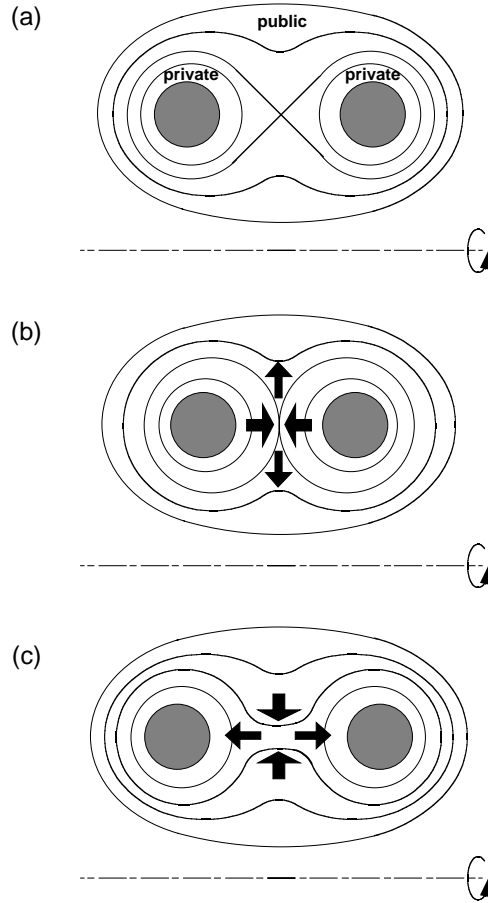
Figure 1.9: "Push-pull" reconnection sequence at MRX. Cross-sectional $r - z$ views are shown; they are rotationally symmetric about the central axes (dashed lines). "Private" magnetic flux exists near each flux core (in grey), and "public" flux exists between them, shown in (a). Increasing toroidal fields result in the private fluxes merging in the "push" phase, (b). Then, decreasing poloidal fields result in the fluxes being stretched back towards the flux cores in the "pull" phase, (c). Note the formation of a Sweet-Parker like 2D reconnection geometry in pull reconnection. The drawings are not identically scaled. Figure from [26].

One of the early goals of MRX was to experimentally test the validity of the Sweet-Parker reconnection model. This work is fully described by Ji [21]. During pull reconnection, they were able to measure whether or not the reconnection rate indeed scaled as $1/\sqrt{S}$, as predicted by the Sweet-Parker model. Here S is the Lundquist number, a dimensionless parameter which in some sense measures how much a plasma deviates from ideal MHD; we will explain this in the next chapter.

The reconnection rates measured at MRX clearly disagreed with the Sweet-Parker prediction. Consequently, the group examined where the assumptions of the Sweet-Parker model broke down. By measuring the strength of the terms in the generalized Ohm's law, they found, as did Stenzel and Gekelman, an enhanced resistivity much larger than the expected classical value. The MRX group also investigated the Sweet-Parker model's assumption of an incompressible plasma, and found the assumption invalid. Finally, it was determined that the model's assumption of constant plasma pressure outside the reconnection layer also failed to hold. The MRX group did find good agreement between their measurements and a generalized Sweet-Parker model incorporating these other effects. In particular, they calculated an effective Lundquist number S_{eff} and found that the measured reconnection rates indeed scaled as $1/\sqrt{S_{\text{eff}}}$.

The other important finding of MRX bearing on the present work is their study of ion flow and heating. This was accomplished using a novel Ion Dynamics Spectroscopy Probe (IDSP) developed at the University of Wisconsin [27]. In their experiments with the IDSP, MRX made their plasmas from helium, rather than hydrogen, which allowed them to observe the 468.6 nm He II spectral line. The probe, which allowed the local observation of plasma light, was installed on one side of the machine, directly between the flux cores. The radial location of the IDSP could be varied, but was close to the radius of the flux cores. The placement of the IDSP is shown in Fig. 1.8. This therefore allowed the local observation of plasma light from the location of pull reconnection. However, the detector for the IDSP was a gated charge-coupled device (CCD) camera – which could not continually monitor the spectral line throughout a single shot. Consequently, temporal studies with the IDSP relied on changing the CCD timing to observe light at different times on multiple shots, which hinged on the reproducibility of the MRX plasma.

Several key results were observed in the IDSP experiments, the first of which was the direct correlation of ion heating with magnetic reconnection. When pull reconnection was not induced, T_i was found to remain approximately constant at about 5 eV, but T_i increased up to about 15 eV when reconnection occurred. When reconnection happened, good temporal correlation was also found between increasing T_i and increasing total dissipated magnetic energy density [24]. Furthermore, radial scans of the IDSP found the ion temperature to increase the most at the reconnection layer. These measurements provided clear evidence that ion heating was being caused by magnetic reconnection.

But what was the mechanism responsible for ion heating? Using the IDSP and Mach probes, the MRX group measured both downstream ion flow in the reconnection plane as well as out-of-plane flow. Unlike TS-3 and SSX, however, MRX did not observe near-Alfvénic outflows. They then computed the kinetic energy density of the flows ($\rho v^2/2$, where ρ is mass density and v is speed) and found this to be an order

of magnitude below the change in thermal energy density ($3nk\Delta T_i/2$, where n is the particle density). Consequently, they concluded that classical viscous dissipation of the ion flows was probably not responsible for the bulk of the heating. Thus, much of the heating was likely caused by nonclassical mechanisms. Recall that the MRX group clearly detected enhanced plasma resistivities beyond the classical Spitzer resistivity. It is likely that the nonclassical heating and nonclassical resistivity are connected, and are perhaps caused by plasma turbulence or instabilities [24]. Recent investigations at MRX have measured the Hall effect, which could be another important mechanism not accounted for by ideal or resistive MHD [28].

1.6   Reconnection and Fusion: Sawtooth Crashes

Sawtooth oscillations occur in toroidal plasmas, such as tokamaks, which seem to offer the most promise for achieving magnetic confinement fusion. They are so called because they involve rapid, edge-like "crashes" in temperature following a slow temperature rise. The sawtooth instability can disrupt a tokamak plasma. Magnetic reconnection is thought to play a role in sawtooth crashes. To fully describe the theory of sawtooth disruptions would require a discussion of tokamak physics beyond the scope of this thesis; the interested reader is referred to the discussion in [29].

1.7   Laboratory Spectroscopy Experiments

Ion Doppler spectroscopy is a well-established diagnostic technique that has been used in many previous plasma physics experiments. Its use has been sufficiently widespread that we cannot hope to give an exhaustive listing of all its uses, but here we briefly describe some of the previous experiments IDS has been used on. In so doing we will also survey some of the capabilities and technologies that have been used with IDS.

IDS has been useful in tokamaks and other fusion plasmas. One example is the ASDEX Upgrade divertor tokamak in Garching, Germany, which observed the C III 229.687 nm line through up to 74 lines of sight through the tokamak [30]. The ASDEX IDS system used an echelle grating spectrometer, as did SSX, but used a CCD detector. In Japan, the Large Helical Device (LHD) stellarator, which is toroidal but non-axisymmetric, has used IDS in a somewhat different way. LHD observed x-ray emissions from heavy elements like Ti, Cr, and Fe and made spectroscopic determinations of ion temperature using quartz crystals as the diffractive element [31]. The Doppler broadening of x-ray emissions has also been observed at other tokamaks, such as Alcator C-Mod at MIT [32].

Another toroidal device that also shows promise for fusion, but has not been as extensively studied as the tokamak, is the reversed field pinch (RFP). IDS has been used extensively at the Madison Symmetric Torus (MST) at the University of Wisconsin-Madison. At MST, the 227.9 nm line of C V has been observed using a duo-spectrometer [33]. This instrument observes the same chord through the plasma from two opposite directions, such that a given flow would appear blueshifted in one direction and redshifted in the other. MST has also developed the ingenious IDS probe that was used both there and at MRX [27]; the IDS probe has

the advantage of being able to make local measurements. While on the subject of MST, we mention that significant efforts there have been made to experimentally study the mechanism of sawtooth oscillations.

IDS has also been used before on spheromak plasmas, such as the Sustained Spheromak Physics Experiment (SSPX) at Lawrence Livermore National Lab [34]. The SSPX IDS instrument used a 16-element PMT array as a detector, not unlike SSX. Other plasma experiments have used IDS as well. We mention the Maryland Centrifugal Experiment (MCX), which is testing the idea of using the centrifugal forces from rotating a plasma for confinement. At MCX, impurity carbon and nitrogen lines have been observed [35]. Finally, the ZaP z-pinch at the University of Washington has used IDS to measure flow profiles in studying the stabilization of various MHD instabilities with flow [36, 37]

Chapter 2

Plasma Theory: Reconnection

The primary theoretical model we will use to deal with the problem of magnetic reconnection will be the fluid description of plasma: magnetohydrodynamics. Thus we begin by listing and briefly describing the equations of MHD. The reader is referred to [1], [2], or [3] for more thorough but still accessible discussions of MHD and its implications.

2.1 Magnetohydrodnamics

How is one to theoretically study a plasma? One might at first think that given a set of electric or magnetic fields, it would not be too difficult to integrate the equations of motion for a charged particle. While the study of single-particle motions (which in the interest of brevity we do not discuss here) does yield important insights, the problem is complicated by the fact that the moving particles in a plasma affect the fields therein. Indeed, trying to fully track the motion of individual particles in a plasma under the fields they produce would quickly result in an analytically intractable set of coupled differential equations. There are two main ways to surmount this obstacle.

The first way, and one of the most useful, is to consider the plasma as a fluid. Then, the results of fluid dynamics can be applied. But since plasmas are electrically conducting and support magnetic fields, it is also necessary to include the equations of classical electromagnetism. The result is known as magnetohydrodynamics. MHD tends to be most applicable to highly collisional plasmas, particularly at higher densities. However, MHD also can be applied to collisionless plasmas, as we will discuss in Sec. 2.6

At lower densities, where collisions between plasma particles are less common, the MHD approach is not so valid. It is still possible to analyze such plasmas using plasma kinetic theory, which relies on statistical mechanics. Again, we will not discuss this approach to plasma theory in detail here. We will also focus on single-fluid MHD, which treats the electrons and ions as a single fluid species, rather than two-fluid models.

Let us then begin by stating the equations for single-fluid MHD. Our discussion here will follow Chen, Goldston, and Gurnett [1], [2], [3]. First of all, neglecting the effects of the creation or destruction of charged particles in the plasma (e.g. through ionization or recombination events), the plasma density should obey a

continuity equation. Let n be the plasma density and $\mathbf{u}$ be the fluid velocity[1]. Then,

$$\frac{\partial n}{\partial t} + \nabla \cdot \mathbf{nu} = 0 \tag{2.1}$$

Next, we can also write Newton's second law for the plasma. Let m be the mass of a species in the plasma and let q be its charge. Then, considering only the forces due to pressure gradients, electric fields, and the Lorentz force, we may write the momentum equation for a single species, say the electrons, which have mass m_e, density n_e, and velocity $\mathbf{v}_e$. This is given by

$$m_e n_e \left[\frac{\partial \mathbf{v}_e}{\partial t} + (\mathbf{v}_e \cdot \nabla) \mathbf{v}_e \right] = -e n_e (\mathbf{E} + \mathbf{v}_e \times \mathbf{B}) - \nabla p_e \tag{2.2}$$

On the left hand side, we have what is called a convective derivative. This is necessary because Newton's second law applies for $\mathbf{u}$ at the position of a set of particles in the fluid, as they move. It is more convenient to consider a fixed spatial point in the fluid, and the convective derivative is thus needed to account for particle motions[2]. Also, we have only considered the gradient of a scalar pressure p here. In full generality, accounting for shearing as well, we would replace ∇p with the divergence of a pressure tensor $\overset{\leftrightarrow}{\mathbf{P}}$.

Now, we can write an analogous equation to (2.2) for the ions in the plasma:

$$m_i n_i \left[\frac{\partial \mathbf{v}_i}{\partial t} + (\mathbf{v}_i \cdot \nabla) \mathbf{v}_i \right] = e n_i (\mathbf{E} + \mathbf{v}_i \times \mathbf{B}) - \nabla p_i \tag{2.3}$$

where the subscript i denotes parameters of the ions. Then, adding the two single-species equations (2.2) and (2.3 gives the MHD single-fluid equation of motion:

$$\rho e \left[\frac{\partial \mathbf{u}}{\partial t} + (\mathbf{u} \cdot \nabla) \mathbf{u} \right] = \mathbf{J} \times \mathbf{B} - \nabla p \tag{2.4}$$

Here, ρ is the mass density of the plasma, we have turned $en\mathbf{v}$ into a current density $\mathbf{J}$, and the electric field terms in both equations cancel.

We will also need a thermodynamic equation of state for the plasma, which will give us more information about the pressure p. It turns out that it is convenient to assume an equation of state

$$p n^{-\gamma} = C \tag{2.5}$$

where C is a constant and γ, familiar from thermodynamics, is the ratio of the specific heat at constant pressure to the specific heat at constant volume. From thermodynamics, for an adiabatic system with three degrees of freedom, $\gamma = 5/3$. For an isothermal system, $\gamma = 1$. Which value of γ to use depends in part on the time scale of the physical problem under consideration.

Thus far we have not really considered any electromagnetic effects, save for the Lorentz force in Newton's second law. Let us now begin to do so. One might initially think that one should just treat plasmas as electric and magnetic media characterized by some permeability ϵ and permittivity μ. In plasmas, it turns

---

[1]In this section we will use $\mathbf{u}$ to distinguish the fluid velocity from the velocity $\mathbf{v}$ of individual species. But in general we will use $\mathbf{v}$ for the fluid velocity, where the context is clear.

[2]In a favorite analogy of M. Brown, consider the change in air pressure in some city in the US. The air pressure can change both due to something happening in the city and due to a low-pressure system moving towards it.

out, the relationship between the magnetization $\mathbf{M}$ and the magnetic field $\mathbf{B}$ turns out to be nonlinear (see Chen [1] for the details). For this and other reasons, it turns out to be most useful to work with Maxwell's equations in vacuum. For charge density ρ_q and current density $\mathbf{J}$, Maxwell's equations read

$$\nabla \cdot \mathbf{E} = \frac{\rho_q}{\epsilon_0} \tag{2.6}$$

$$\nabla \times \mathbf{E} = -\frac{\partial \mathbf{B}}{\partial t} \tag{2.7}$$

$$\nabla \cdot \mathbf{B} = 0 \tag{2.8}$$

$$\nabla \times \mathbf{B} = \mu_0 \left(\mathbf{J} + \epsilon_0 \frac{\partial \mathbf{E}}{\partial t} \right) \tag{2.9}$$

with the above equations being Gauss's law, Faraday's law, no magnetic monopoles, and Ampère's law. It turns out that not all of these will be relevant. The charge density ρ_q will not appear in any of the other necessary equations, so Gauss's law can be dropped. We will also show that $\nabla \cdot \mathbf{B} = 0$ is an initial condition rather than an equation of its own. Particularly, consider taking the divergence of both sides of Faraday's law:

$$\nabla \cdot \nabla \times \mathbf{E} = \nabla \cdot -\frac{\partial \mathbf{B}}{\partial \mathbf{t}} \tag{2.10}$$

But, the divergence of a curl is always 0. Reversing the order of the temporal and spatial derivatives, we can then write,

$$\frac{\partial}{\partial t}(\nabla \cdot \mathbf{B}) = 0 \tag{2.11}$$

which states that the divergence of $\mathbf{B}$ is constant in time. So, if $\nabla \cdot \mathbf{B}$ is zero at any one time, it stays zero forever. It is in this sense that $\nabla \cdot \mathbf{B} = 0$ should be viewed as an initial condition.

Finally, the displacement current term ($\frac{\partial \mathbf{E}}{\partial t}$) in Ampère's law can be neglected, as we will show once we have introduced some other necessary equations.

One more equation is needed. We have so far 14 unknowns: the vectors $\mathbf{E}$, $\mathbf{B}$, $\mathbf{J}$, $\mathbf{u}$, with three components each, and the scalar density n and pressure p. We have 3 vector equations, each of which can be counted threefold: momentum, or Newton's second law (2.4), Faraday's law, and Ampère's law without displacement current. The thermodynamic equation of state (2.5) and the continuity equation (2.1) are scalar, for a total of 11 equations. We can get another equation by introducing Ohm's law[3]. Empirically, some sort of force is needed to cause stationary charges to move to form a current density. The force is given by electrostatic force and the Lorentz force, and the proportionality is given by the resistivity η. This gives

$$\eta \mathbf{J} = \mathbf{E} + \mathbf{u} \times \mathbf{B} \tag{2.12}$$

The reader is probably familiar with Ohm's law for a resistive circuit element, $V = IR$, to which the above reduces (see Griffiths [38]). If the plasma resistivity is small enough to be negligible, (2.12) reduces to

$$\mathbf{E} + \mathbf{u} \times \mathbf{B} = 0 \tag{2.13}$$

---

[3]Ohm's law not being a fundamental physical relationship in the way that Maxwell's equations are, we should probably say "Ohm's 'law'" as does Landreman [4]. But this usage seems clumsy, and so we will continue to write "Ohm's law."

which is called the ideal Ohm's law. MHD using this equation is known as ideal MHD. As this is a vector equation, this completes our set of MHD equations.

Having introduced the ideal Ohm's law, we can now show that the displacement current term in Ampère's law is negligible. We include this argument, which is tangential to our main development, because it is a nice example of the approximate calculations that are frequently useful in plasma physics. We will show that the ratio of the displacement current term to the curl of $\mathbf{B}$ is small. This we can do by approximating $\nabla \times \mathbf{B}$, a spatial derivative, with B/L, where L is a characteristic length in the plasma. Likewise, we can approximate $\frac{\partial \mathbf{E}}{\partial t}$ by E/τ, where τ is a characteristic MHD time scale in the plasma (such as the Alfvén time, for instance, which will be explained shortly). Then, using the fact that the speed of light $c = 1/\sqrt{\epsilon_0 \mu_0}$,

$$\frac{|\frac{\partial}{\partial t}\mu_0\epsilon_0\mathbf{E}|}{|\nabla \times \mathbf{B}|} = \frac{E}{c^2\tau} \cdot \frac{L}{B} \tag{2.14}$$

Now, it is possible to show (see, for instance, Chen [1]) that the single particle guiding center drift due to crossed electric and magnetic fields is given by $\mathbf{v} = \mathbf{E} \times \mathbf{B}/B^2$. Thus, we may take $v = E/B$ (which also is a consequence of the ideal Ohm's law), and so we have

$$\frac{|\mu_0\epsilon_0\mathbf{E}|}{|\nabla \times \mathbf{B}|} = \frac{v}{c} \cdot \frac{L}{c\tau} = \left(\frac{v}{c}\right)^2 \tag{2.15}$$

since L/τ can be taken to be comparable to the speed v. For a nonrelativistic plasma, $(v/c)^2$ will surely be small, so the entire displacement current term will be negligible.

The astute reader might feel somewhat uncomfortable with the approximations we have made in developing ideal MHD, particularly in neglecting the plasma resistivity η. The discomfort is justified. As we have mentioned, magnetic reconnection cannot happen in ideal MHD, as we show in the next section. It turns out that there is a generalized Ohm's law including other effects including plasma resistivity, the Hall effect, pressure gradients, and electron inertia. We will not include the lengthy derivation of the generalized Ohm's law, but we state it here for reference in all its glory:

$$\mathbf{E} + \mathbf{u} \times \mathbf{B} = \eta\mathbf{J} + \frac{1}{ne}\mathbf{J} \times \mathbf{B} - \frac{1}{ne}\nabla \cdot \overleftrightarrow{\mathbf{P}} + \frac{m_e}{ne^2}\frac{\partial \mathbf{J}}{\partial t} \tag{2.16}$$

2.2 Alfvén Speed

We digress to define an important plasma parameter that will often arise in the rest of this thesis. This is the Alfvén speed, denoted v_A. The Alfvén speed is most often encountered as the phase velocity of a particular type of MHD wave. It is convenient, however, to think of the Alfvén speed as a sort of speed limit in a magnetized plasma. It is the speed a plasma would attain if it converted all of its magnetic energy into kinetic energy. If a plasma has magnetic fields B, then it has magnetic energy density $B^2/2\mu_0$. Suppose all of this energy were converted into kinetic energy, $\frac{1}{2}\rho v_A^2$, where ρ is a mass density. Then, by equating these energy densities, we find that

$$v_A = \frac{B}{\sqrt{\rho\mu_0}} \tag{2.17}$$

We also define the Alfvén time $\tau_A \equiv v_A/L$, where L is some characteristic length scale in the plasma.
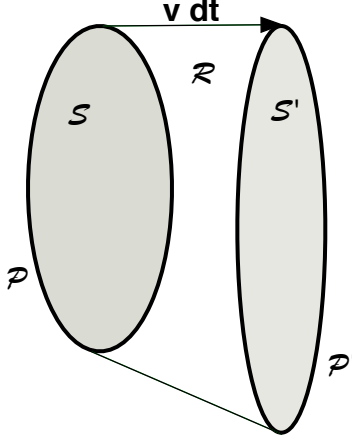
Figure 2.1: Figure for proof of the frozen-in flux theorem of ideal MHD.

2.3 The Frozen-in Flux Theorem

An important result of ideal MHD is the frozen-in flux theorem, also known as Alfvén's theorem. This result is violated during magnetic reconnection and reveals the failure of ideal MHD to adequately describe plasma phenomena.

Following Griffiths' [38] approach, we will argue that the following version of Alfvén's theorem holds: In an ideal MHD plasma, the magnetic flux through a closed loop moving with the plasma is constant in time.

Consider then an imaginary loop $\mathcal{P}$ in the plasma. Let $\mathcal{S}$ be the surface bounded by $\mathcal{P}$. In a short time interval dt, $\mathcal{P}$ moves due to the plasma velocity. Let $\mathcal{P}'$ and $\mathcal{S}'$ be the loop and enclosed surface after time interval dt. This setup is shown in Fig. 2.1. Then, the change in magnetic flux through the enclosed surface $d\Phi$ over this time interval is given by

$$d\Phi = \int_{\mathcal{S}'} \mathbf{B}(t+dt) \cdot d\mathbf{a} - \int_{\mathcal{S}} \mathbf{B}(t) \cdot d\mathbf{a} \tag{2.18}$$

Now, let $\mathcal{R}$ be the "ribbon" joining $\mathcal{S}$ and $\mathcal{S}'$. Since $\mathbf{B}$ is divergenceless, by Gauss's theorem, the surface integral of B through any closed surface is zero. So, since the total flux through the closed surface made up of $\mathcal{S}$, $\mathcal{S}'$, and $\mathcal{R}$ is zero, when we account for the change in sign in $d\mathbf{a}$ for $\mathcal{S}$, because of the sense in which flux is computed, we find at time $t + dt$ that

$$-\int_{\mathcal{S}} \mathbf{B}(t+dt) \cdot d\mathbf{a} + \int_{\mathcal{R}} \mathbf{B}(t+dt) \cdot d\mathbf{a} + \int_{\mathcal{S}'} \mathbf{B}(t+dt) \cdot d\mathbf{a} = 0 \tag{2.19}$$

Substituting into (2.18) to eliminate the integral over $\mathcal{S}'$, we have

$$d\Phi = \int_{\mathcal{S}} \mathbf{B}(t+dt) \cdot d\mathbf{a} - \int_{\mathcal{R}} \mathbf{B}(t+dt) \cdot d\mathbf{a} - \int_{\mathcal{S}} \mathbf{B}(t) \cdot d\mathbf{a}$$
$$= \int_{\mathcal{S}} [\mathbf{B}(t+dt) - \mathbf{B}(t)] \cdot d\mathbf{a} - \int_{\mathcal{R}} \mathbf{B}(t+dt) \cdot d\mathbf{a}$$
$$= dt \int_{\mathcal{S}} \left(\frac{\partial \mathbf{B}}{\partial t}\right) \cdot d\mathbf{a} - \int_{\mathcal{R}} \mathbf{B}(t+dt) \cdot d\mathbf{a}$$

We can transform the last integral on the right, the one over $\mathcal{R}$. This is done by rewriting $d\mathbf{a}$. In particular, since a point on $\mathcal{P}$ in the plasma moves a distance $\mathbf{v}dt$ in time dt, by the parallelogram rule we can express the area element on $\mathcal{R}$ as

$$d\mathbf{a} = \mathbf{v}dt \times d\mathbf{l} = (\mathbf{v} \times d\mathbf{l})dt \tag{2.20}$$

where $d\mathbf{l}$ is a length element on the loop $\mathcal{P}$. Then, substituting for $d\mathbf{a}$ and using a vector identity,

$$\int_{\mathcal{R}} \mathbf{B}(t + dt) \cdot d\mathbf{a} = dt \int_{\mathcal{P}} \mathbf{B}(t + dt) \times \mathbf{v} \cdot d\mathbf{l} \tag{2.21}$$

$$= -\int_{\mathcal{S}} \nabla \times \mathbf{v} \times \mathbf{B} \cdot d\mathbf{a} \tag{2.22}$$

where in the second step we have used Stokes's theorem. We can now substitute this back into our equation for $d\Phi$, reversing the sign to account for the appropriate convention in computing the flux through $\mathcal{S}$. Dividing through by dt then gives

$$\frac{d\Phi}{dt} = \int_{\mathcal{S}} \left(\frac{\partial \mathbf{B}}{\partial t} - \nabla \times \mathbf{v} \times \mathbf{B} \right) \cdot d\mathbf{a} \tag{2.23}$$

Now we will invoke the ideal Ohm's law. From Faraday's law,

$$\nabla \times \mathbf{E} = -\frac{\partial \mathbf{B}}{\partial t} \tag{2.24}$$

But, since $\mathbf{E} = -\mathbf{v} \times \mathbf{B}$, from the ideal Ohm's law, Faraday's law becomes

$$\nabla \times \mathbf{v} \times \mathbf{B} = \frac{\partial \mathbf{B}}{\partial t} \tag{2.25}$$

This equality makes the integrand in (2.23) vanish. It follows that the flux through $\mathcal{S}$ is constant in time:

$$\frac{d\Phi}{dt} = 0 \tag{2.26}$$

proving Alfvén's theorem.

2.4   Resistive MHD and the Induction Equation

Given that ideal MHD, where the right hand side of the generalized Ohm's law (2.16) is taken to be zero, makes strong assumptions and is not always valid, the conceptually and mathematically simplest modification to the theory is to add the resistive term to Ohm's law:

$$\mathbf{E} + \mathbf{v} \times \mathbf{B} = \eta \mathbf{J} \tag{2.27}$$

MHD using the form of Ohm's law above is called resistive MHD.

Recall that from the frozen-in flux theorem of ideal MHD, we found that magnetic fields changed in time only because the fluid moved and the field convected with the fluid. We will show that this is not so in resistive MHD, and that the resistivity causes a *diffusion* of the magnetic field.

It turns out to be fruitful to begin by taking the curl of the resistive Ohm's law (2.27). Assuming the resistivity to be constant through the plasma, we find that

$$\nabla \times (\mathbf{E} + \mathbf{v} \times \mathbf{B}) = \eta \nabla \times \mathbf{J}. \tag{2.28}$$

But, from Ampère's law, we know that $\mu_0 \mathbf{J} = \nabla \times \mathbf{B}$, and from Faraday's law, we have $\nabla \times \mathbf{E} = -\frac{\partial \mathbf{B}}{\partial t}$. Substituting these into the above then yields

$$-\frac{\partial \mathbf{B}}{\partial t} + \nabla \times (\mathbf{v} \times \mathbf{B}) = \frac{\eta}{\mu_0} \nabla \times (\nabla \times \mathbf{B}). \tag{2.29}$$

Recalling the identity for a vector field $\mathbf{C}$

$$\nabla \times (\nabla \times \mathbf{C}) = \nabla(\nabla \cdot \mathbf{C}) - \nabla^2 \mathbf{C} \tag{2.30}$$

and noting that $\nabla \cdot \mathbf{B} = 0$, we find after a little rearranging that

$$\frac{\partial \mathbf{B}}{\partial t} = \nabla \times (\mathbf{v} \times \mathbf{B}) + \frac{\eta}{\mu_0} \nabla^2 \mathbf{B}. \tag{2.31}$$

This result is often called the induction equation. The first term on the right hand side has to do with magnetic field convection, for it arose under ideal MHD when we derived the frozen-in flux theorem. That is, in ideal MHD, the field is frozen into the fluid, so $\mathbf{B}$ only changes in time because of the plasma being convected from place to place. The second term describes diffusion, for if we ignore the convective term,

$$\frac{\partial \mathbf{B}}{\partial t} = \frac{\eta}{\mu_0} \nabla^2 \mathbf{B} \tag{2.32}$$

mathematically has the form of a diffusion equation. It follows, then, that in resistive MHD, magnetic fields can not only convect but also diffuse, with the diffusion being governed by the resistivity η.

Naturally, one might want to characterize, for a given plasma, whether convection or diffusion is the dominant process affecting the magnetic field. We can do this by taking the ratio, in an approximate sense, of the convection and diffusion terms in the induction equation (2.31). In so doing, it will be convenient to approximate the vector operator ∇, which is a spatial derivative, with $1/L$, where L is the length scale of the plasma, just as we did when we justified neglecting the displacement current term in Ampère's law. We then find

$$\frac{\text{convection}}{\text{diffusion}} \approx \frac{(1/L)vB}{\frac{\eta B}{\mu_0 L^2}}. \tag{2.33}$$

This dimensionless quantity is called the magnetic Reynolds number, denoted R_M:

$$R_M \equiv \frac{\mu_0 L v}{\eta}. \tag{2.34}$$

When the fluid velocity v in the above is taken to be the Alfvén velocity, the result is termed the Lundquist number, S:

$$S \equiv \frac{\mu_0 L v_A}{\eta}. \tag{2.35}$$

The Lundquist number is, in some sense, a measure of how well the field lines are frozen to the plasma, for a perfectly conducting plasma would have $S = \infty$. At SSX, $S \approx 1000$, but in the solar corona and other astrophysical contexts, S can be as high as 10^{14}.

Throughout this section, we have been discussing the resistivity of a plasma without mention of its underlying physical cause. Just as the resistivity in an ordinary solid conductor may (in classical physics) be explained as coming from collisions between conduction electrons and the fixed ions of the solid, in classical theory, the resistivity of a plasma comes from Coulomb collisions between the charged particles in the plasma. This classical plasma resistivity is called the Spitzer resistivity, after Lyman Spitzer, who was the first to derive it [39]. For current densities perpendicular to a magnetic field, the Spitzer resistivity turns out to be

$$\eta_\perp = 1.03 \times 10^{-2} \frac{Z \ln \Lambda}{(kT_e)^{3/2}} \ \Omega \ \text{cm} \tag{2.36}$$

where kT_e is in eV, Z is the charge of the ions, and where $\ln \Lambda$ is the Coulomb logarithm. The Coulomb logarithm is a quantity having to do with the maximum meaningful impact parameter for a Coulomb collision; it depends weakly on density and temperature. In Appendix A we perform a calculation in which the Coulomb logarithm arises, and in that context the physical significance of $\ln \Lambda$ will become more clear. The interested reader is referred to Goldston for more details on both the Coulomb logarithm and on plasma resistivity [2].

In plasmas where collisions are rare, however, the Spitzer resistivity would not seem to be valid. Classical resistivity causes currents, and hence magnetic fields, to dissipate. It turns out that there are many other phenomena that also dissipate magnetic fields and thus effectively function as nonclassical or anomalous resistivities. Microscale turbulence is one example. Other possibilities include an "inertial resistivity" in which a perpendicular magnetic field causes particles to drift out of a current sheet and thus decrease the total momentum in the current sheet [26]. Other possible causes of anomalous resistivity include various types of wave-particle interactions. Anomalous plasma resistivities have been definitively measured in the laboratory. For instance, recall that at MRX, Ji *et al.* measured an effective resistivity that was up to 10 times the Spitzer resistivity [21, 22].

2.5 Plasma β

In the previous section we met the dimensionless parameters R_M and S, the magnetic Reynolds and Lundquist numbers. Dimensionless quantities are useful in plasma physics because they allow the comparison of different plasmas, such as experiments with different length scales. Another such useful dimensionless parameter is β, which is defined as the ratio of plasma pressure to magnetic pressure:

$$\beta \equiv \frac{2\mu_0 p}{B^2} \tag{2.37}$$

Here, the magnetic energy density $B^2/2\mu_0$ has units of energy per unit volume, which is dimensionally equivalent to pressure.

The plasma β is particularly useful in the context of fusion. Many of the currently proposed schemes for fusion require magnetic confinement of a hot plasma.[4] One necessary, but not sufficient, condition for achieving magnetic confinement fusion is to balance the kinetic pressure p of the plasma with the magnetic pressure $B^2/2\mu_0$. Thus, in order to magnetically confine a plasma at some pressure p, the smaller the required magnetic fields, the larger the β. Since generating magnetic fields requires energy (i.e. the energy needed to drive the external current coils of a tokamak), plasmas with higher β are attractive for fusion. We note that tokamaks typically have $\beta \approx 0.05$, while spheromaks tend to have β between 0.01 and 0.2 [4, 40].

Another way to think about β is that low-β plasmas are dominated by magnetic forces, whereas they are less important in high-β plasmas.

2.6   MHD in Collisionless Plasmas

In deriving MHD, we assumed that the plasma behaved like a fluid. In most fluids, collisions (such as the Coulomb collisions between charged particles) dominate the interactions. Many plasmas, particularly in astrophysical contexts like the earth's magnetotail, have such low densities that interparticle collisions are rare. It turns out, however, that MHD works quite well for describing the large-scale properties of such plasmas. Here, we briefly argue why, following Priest and Forbes, to which the interested reader is referred for a much fuller discussion [41].

A fluid theory would clearly be invalid if the particles in the fluid were able to travel distances comparable to the scale length of the plasma without interactions (which is not the case in a fluid). We will now give a plausibility argument for the applicability of MHD in collisionless but magnetized plasmas by arguing that large-scale motions of particles in a plasma is impeded. First of all, we know from the study of single-particle motions that the charged particles in a plasma tend to gyrate around the magnetic field lines. Thus, motion perpendicular to **B** is relatively impeded. In addition, interactions with plasma waves tends to hinder the motion of particles along the field lines [41].

Moreover, many of the MHD equations, such as Maxwell's equations, the continuity equation, and the momentum equations, come from physical laws or conservation principles that hold regardless of the collisionality of the plasma. Ultimately, however, the ability of MHD to make good predictions even about collisionless plasmas is the best justification for its applicability.

2.7   Sweet-Parker Reconnection

The basic theory of reconnection was developed by Sweet and Parker [42]. Although the Sweet-Parker model predicts an overly slow reconnection rate, it is a useful paradigm for reconnection in that it is simple. Our discussion of the Sweet-Parker model will follow Priest [41].

---

[4]We do not here discuss a totally different approach, inertial confinement fusion, which in recent years has had significant advances.
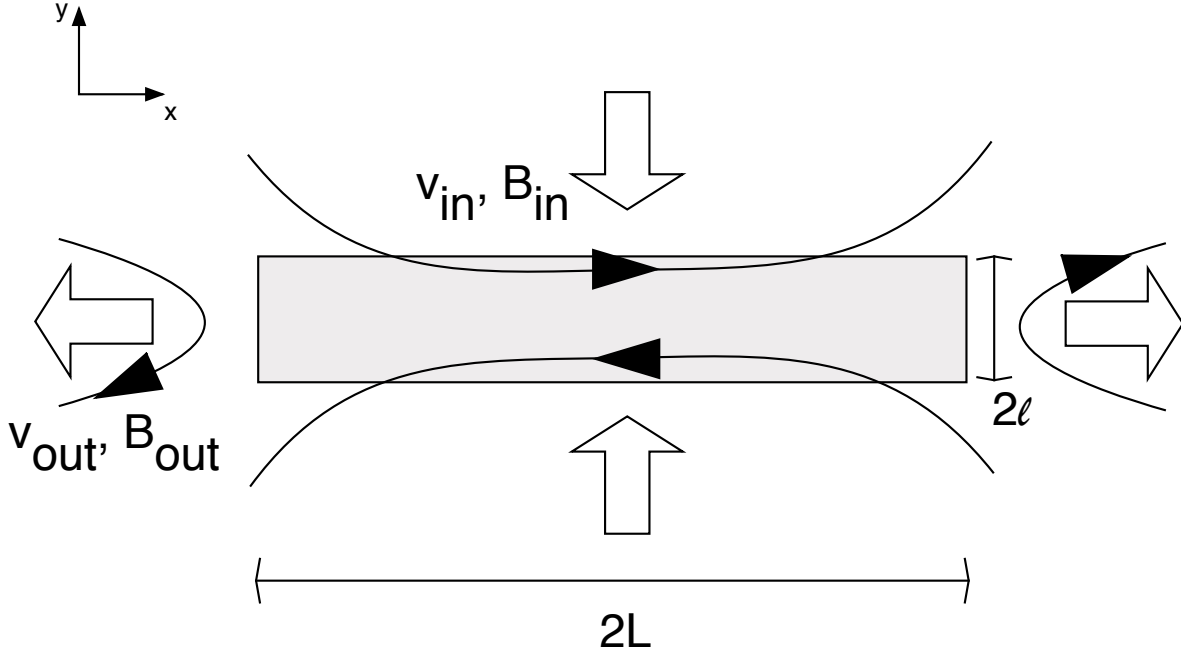
Figure 2.2: Geometrical setup for the 2D Sweet-Parker reconnection model. The z-axis points out of the page. Reconnection is assumed to occur in a rectangular region of width $2L$ and thickness 2ℓ, which is shaded in the figure. The thick unshaded arrows represent the velocity of the flowing plasma. The thin black lines represent magnetic fields.

The Sweet-Parker model makes the simplifying assumption of a two-dimensional reconnection geometry. Plasma carrying oppositely directed magnetic fields in the x direction is flowing together. The magnetic field lines are assumed to be basically straight, but have just enough curvature such that the field lines meet in a well-defined reconnection layer of width $2L$ and thickness 2ℓ, where $L \gg \ell$. As shown in the figure, the plasma flows into the side of the reconnection layer that has length $2L$ in the y direction, with speed v_{in}. The outflow, in the x direction, then occurs through the sides of the layer that have length 2ℓ with speed v_{out}. This geometry is shown in Fig. 2.2. The Sweet-Parker model considers steady-state reconnection (although the mechanisms by which reconnection begins remain an open question), so all time derivatives will be zero. We will also assume an incompressible plasma.

The basic goal in the Sweet-Parker model will be to derive a dimensionless reconnection rate that gives some indication of how quickly reconnection is occurring. What parameters might be worth considering to do this? One possibility that comes to mind is the plasma inflow speed v_{in}, for this determines how quickly magnetic field is carried into the reconnection layer. The inflow speed, however, may vary greatly from plasma to plasma, and so is not the best way to compare reconnection occurring in different contexts. The Alfvén speed v_A, however, also varies from plasma to plasma. So, by dividing v_{in} by v_A, we may obtain a dimensionless parameter that may be better compared between plasmas. Thus, we define the dimensionless

reconnection rate

$$M \equiv \frac{v_{\text{in}}}{v_A} \tag{2.38}$$

With this in mind, let us determine the reconnection rate M. We begin by considering the resistive Ohm's law (2.27). Outside the reconnection layer, the magnetic field lines are approximately straight, so $\nabla \times \mathbf{B} = 0$. By Ampère's law, this implies that $\mathbf{J} = 0$. It then follows, for the z component of Ohm's law, that

$$E_z = v_{\text{in}} B_{\text{in}} \tag{2.39}$$

where B_{in} is the magnetic field in the inflow plasma. Inside the reconnection layer, the magnetic field is zero, and one would also expect v to stagnate to zero. So, Ohm's law reduces to

$$E_z = \eta J_z \tag{2.40}$$

We can use Ampère's law to determine the current density J_z in the reconnection layer. Consider an Ampèrian loop running around the boundary of the reconnection layer. Assuming the magnetic fields to be primarily in the x direction, the segments of the line integral along the short sides of the reconnection layer contribute nothing. Then, equating the line integral of $\mathbf{B}$ to the enclosed current density,

$$B_{\text{in}} \cdot 4L = \mu_0 J_z \cdot 2L \cdot 2\ell \tag{2.41}$$

It follows that

$$J_z = B_{\text{in}}/\mu_0 \ell \tag{2.42}$$

We can now eliminate E_z and J_z. If we assume a steady state situation, then $\frac{\partial \mathbf{B}}{\partial t} = 0$ and thus $\nabla \times \mathbf{E} = 0$. This requires the electric field outside the reconnection layer, given by (2.39), to equal the electric field inside the reconnection layer, given by (2.40). Thus $v_{\text{in}} B_{\text{in}} = \eta J_z$. Using (2.42) to eliminate J_z and solving for v_{in}, we find

$$v_{\text{in}} = \frac{\eta}{\mu_0 \ell} \tag{2.43}$$

We would like to eliminate ℓ from our result for v_{in}, however. By continuity and assuming an incompressible plasma, the amount of plasma flowing into the reconnection layer must equal the amount of plasma flowing out. It follows that

$$v_{\text{in}} L = v_{\text{out}} \ell \tag{2.44}$$

where v_{out} is the outflow speed. Solving (2.43) for ℓ and substituting into the above gives

$$v_{\text{in}}^2 = \frac{\eta}{\mu_0 L} v_{\text{out}} \tag{2.45}$$

To determine the outflow speed, we will need the MHD equation of motion, (2.4). In the steady state, this becomes

$$\rho(\mathbf{v} \cdot \nabla)\mathbf{v} = -\nabla p + \mathbf{J} \times \mathbf{B} \tag{2.46}$$

Assuming pressure gradients to be negligible, the right side of the above approximately reduces to JB_{out} in the outflow region. On the left side, approximate the derivative by $1/L$. Then, using (2.42), we find approximately that

$$\rho \frac{v_{\text{out}}^2}{L} = \frac{B_{\text{in}} B_{\text{out}}}{\mu_0 \ell} \tag{2.47}$$

Since $\nabla \times \mathbf{E} = 0$, the electric field must be everywhere uniform. Outside the reconnection layer, where $\mathbf{J}$ is zero, the electric field in the inflowing plasma is given by (2.39) in the inflowing plasma and

$$E = v_{\text{out}} B_{\text{out}} \tag{2.48}$$

in the outflowing plasma. Both of these electric fields must be equal, so

$$v_{\text{in}} B_{\text{in}} = v_{\text{out}} B_{\text{out}} \tag{2.49}$$

Consequently, invoking continuity (2.44), this becomes

$$B_{\text{in}} \ell = B_{\text{out}} L \tag{2.50}$$

It then follows from (2.47) and (2.50) that the outflow speed

$$v_{\text{out}}^2 = \frac{B_{\text{in}}^2}{\mu_0 \rho} = v_A^2 \tag{2.51}$$

is exactly equal to the Alfvén speed for the inflowing plasma.

We could have just assumed that the reconnection process effectively converts all of the incoming plasma's magnetic energy density into kinetic energy, and thus would also find $v_{\text{out}} = v_A$. This, like (2.50), must also be viewed as approximate as this neglects effects such as heating due to reconnection.

Either way, (2.45) then becomes

$$v_{\text{in}}^2 = \frac{\eta}{\mu_0 L} v_A \tag{2.52}$$

and the dimensionless Sweet-Parker reconnection rate, M_{SP}, is given by

$$M_{SP} = \frac{v_{\text{in}}}{v_A} = \sqrt{\frac{\eta}{\mu_0 L v_A}} \tag{2.53}$$

But, recalling the definition of the Lundquist number S (2.35), and taking the width L of the reconnection layer to be the characteristic plasma length, we see that

$$M_{SP} = \frac{1}{\sqrt{S}} \tag{2.54}$$

This is the fundamental prediction of the Sweet-Parker model.

2.8   Petschek and Other Reconnection Theories

Even when Sweet and Parker proposed their reconnection model, they realized that the normalized reconnection rate it predicted, $M_{SP} = 1/\sqrt{S}$, was far too slow. The first model to predict a faster reconnection rate

was developed by Petschek in 1964. Like the Sweet-Parker model, the Petschek model considers a reconnection region of width $2L$. However, the magnetic fields only merge in a diffusion region of width $2L'$, where $L' \ll L$, unlike the Sweet-Parker model in which the diffusion region extends along the full width of the reconnection region. In the rest of the reconnection region, plasma is accelerated by four magnetoacoustic shock waves, which are analogous to sonic booms. These shocks are another means of converting magnetic energy into kinetic energy and heat. Petschek reconnection predicts the following reconnection rate [43]:

$$M_{\text{Petschek}} = \frac{1}{\sqrt{S}} \sqrt{\frac{L}{L'}} \tag{2.55}$$

where as before S is the Lundquist number. The Sweet-Parker reconnection rate is thus enhanced by $\sqrt{L/L'}$ in this model, where L' has not yet been physically determined. It may be shown that the fastest possible Petschek reconnection rate is

$$M_{\text{Petschek,max}} = \frac{\pi}{8 \ln S} \tag{2.56}$$

which yields a much closer reconnection rate to observations [7].

While the shocks that are critical to Petschek's model have been seen in numerical simulations [41], they have never been physically observed. Consequently, the Petschek model has not been fully accepted. Still, other theorists, such as Vasyliunas, have modified Petschek's theory by adopting different boundary conditions to derive other models for fast reconnection.

Yet other possibilities for 2D reconnection include moving beyond resistive MHD. It turns out that the $\mathbf{J} \times \mathbf{B}$ Hall term can play a significant reconnection. Hall effects may be shown to lead to a separation of ion and electron layers. Furthermore, there is an out-of-plane quadrupole magnetic field. These have both been measured at SSX.

We mention also that reconnection has been extensively studied computationally. Any detailed discussion of computational studies of reconnection would be beyond the scope of this thesis, but the recent work of Birn *et al.* comparing different simulations (resistive MHD, Hall MHD, hybrid MHD, and particle) of the same reconnection setup perhaps gives some sense of the present state of the field [44].

2.9   Physics of the Spheromak

We are interested in equilibrium solutions to the MHD equations. It turns out that the spheromak is one possible equilibrium. To have an equilibrium without bulk flows, it follows from by setting $\mathbf{v} = 0$ in (2.4) that we require

$$\nabla p = \mathbf{J} \times \mathbf{B} \tag{2.57}$$

Alas, this partial differential equation, called the Grad-Shafranov equation, is essentially analytically intractable, although numerical studies of spheromaks as Grad-Shafranov equilibria are possible [45]. But recall our discussion of β. In a spheromak, β is small, so it is a reasonable approximation to neglect the pressure gradient ∇p. Then, the Grad-Shafranov equation reduces to $\mathbf{J} \times \mathbf{B} = 0$. But, from Ampère's law,

we then have

$$(\nabla \times \mathbf{B}) \times \mathbf{B} = 0 \tag{2.58}$$

Assuming that both $\mathbf{J}$ and $\mathbf{B}$ are nonzero, it must follow that $\nabla \times \mathbf{B}$ and $\mathbf{B}$ are parallel. Equivalently, the equilibrium magnetic field must be a multiple of $\nabla \times \mathbf{B}$, giving us the "eigenvalue" equation

$$\nabla \times \mathbf{B} = \lambda \mathbf{B} \tag{2.59}$$

Here, λ is a scalar field, but is not necessarily a constant. This is the condition for what is known as a force-free equilibrium. It is possible to show that the spheromak is a solution of this equation.

An important quantity in this theory is the magnetic helicity K, which is a measure of how topologically twisted together the magnetic flux tubes in a plasma are. The helicity is given by

$$K = \int_V \mathbf{A} \cdot \mathbf{B} \, d^3\mathbf{r} \tag{2.60}$$

where $\mathbf{A}$ is the magnetic vector potential and the integral is over the volume of plasma of interest.[5]

The magnetic helicity is useful because under most circumstances, it is a robust quantity that is approximately "conserved" in the sense that it decays no faster than the magnetic energy density. Fortuitously, it turns out that the solutions of (2.59) that minimize the magnetic energy for a given, fixed K are the solutions where λ is a constant [46]. It is then possible to solve (2.59) directly; the reader is referred to [45] or [40] for the details. This is how the analytical force-free equilibrium for the spheromak may be found.

---

[5]It may be shown that, so long as no field lines penetrate the surface of the plasma, K is independent of the choice of gauge for $\mathbf{A}$[40].

Chapter 3

The IDS System

In this chapter, we describe the details of the ion Doppler spectroscopy (IDS) system as well as the calibration measurements that have been performed with it. Recall that the Doppler shift of the spectral line provides a measure of the flow velocity of the plasma, while the Doppler broadening of the line indicates the ion temperature. We first discuss what we expect to measure with the IDS system, and the consequent design requirements. After this we describe the physics of the IDS in detail. We then describe the components of the IDS system, a schematic diagram of which we show in Fig. 3.1. Lastly, we describe the calibration of the IDS.

3.1 Estimation of Design Requirements for the IDS System

What do we need the IDS system to be capable of doing? Briefly, we want the IDS to be able to measure rapid flows in either direction along the line of sight, have the spectral resolution to accurately measure ion temperatures, and have enough time resolution to be able to observe fast changes in an ever-changing reconnection plasma. Let us try to quantitatively estimate what these design goals must be and the performance requirements it will take to satisfy them.

First of all, we must know what spectral lines exist in the plasma. Previous studies by V. Lukin with a VUV monochromator have indicated the presence of significant emission from carbon impurities in the plasma. In particular, the C III 229.687 nm line seemed to be a good candidate.

Now let us address the requirement that the IDS be sensitive to measuring a sufficiently wide range of flow speeds. Recall that the Alfvén speed v_A is a physical speed limit imposed by energy conservation. But plasma could be flowing either towards or away from the line of sight with speed v_A. Thus, we should require the total range of speeds to which the IDS is sensitive to be be $2v_A$. As we will soon show, it turns out that the Doppler shift $\Delta\lambda$ of a line of wavelength λ due to source motion at speed v is

$$\frac{\Delta\lambda}{\lambda} = \frac{v}{c} \tag{3.1}$$

Since the Alfvén speed in SSX is approximately $v_A \sim 100$ km/s, we will require that $\Delta\lambda/\lambda \sim 3 \times 10^{-4}$. For $\lambda = 229.687$ nm, this requires that the IDS have a bandwidth of $\Delta\lambda \sim 0.07$ nm.
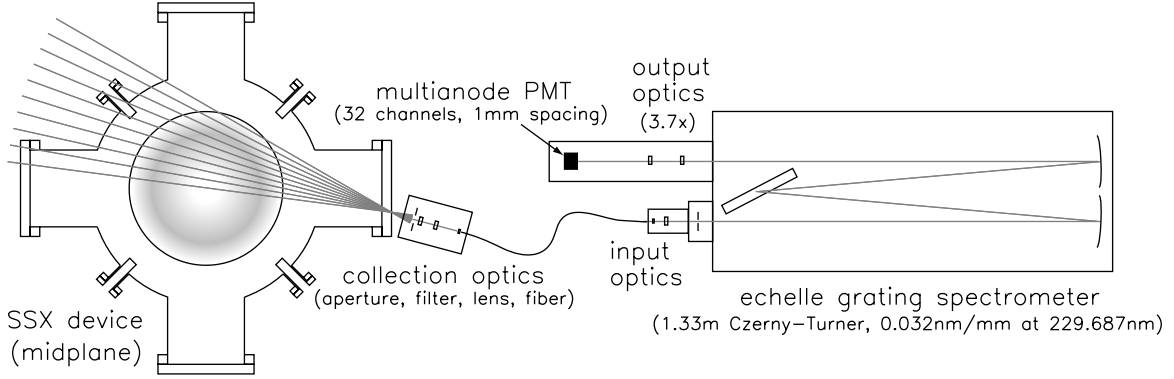
Figure 3.1: Schematic diagram of the IDS system at the SSX. Any of 10 chords through the plasma can be observed.

We will also show that the ion temperature T_i is given by

$$\frac{\Delta\lambda_{\text{FWHM}}}{\lambda_0} = 2\left(\frac{2kT_i \ln 2}{mc^2}\right)^{1/2} \tag{3.2}$$

For the purposes of making an estimate, we can drop various small numerical factors and assert that we must surely have

$$\frac{\Delta\lambda}{\lambda} < \sqrt{\frac{kT_i}{mc^2}} \tag{3.3}$$

For $kT_i \sim 20$ eV and $mc^2 \sim 12$ GeV for carbon ions, we require from the above that the minimum wavelength resolution be $\Delta\lambda/\lambda \sim 4 \times 10^{-5}$. For the C III 229.687 nm line, this requires that the IDS have the resolution to detect broadening as narrow as 0.009 nm.

Finally, let us consider the time resolution the instrument must have. The maximum speed of moving plasma would be the Alfvén speed $v_A \sim 100$ km/s, and a characteristic length scale in SSX is about $L = 0.2$ m. We can define an Alfvén time $\tau_A \equiv v_A/L$; for SSX, $\tau_A \sim 2$ μs. To not miss any large-scale plasma dynamics, then, the IDS must be able to observe the plasma at least every 2 μs, and preferably faster.

3.2 Physics of IDS

Here we briefly review the physics of the Doppler effect and then discuss the physics behind the IDS. Bear in mind that the IDS system observes well-defined spectral lines from impurity ions in the plasma.

The Doppler effect for sound waves is an effect familiar to anyone who has ever heard the pitch of a car horn change as the car drives by. This effect occurs because an observer at rest perceives the wavelength of the sound waves emitted by a moving source to be different than they are in the frame of the source. Essentially the same physics applies when one considers the Doppler effect in for moving sources of light. It is necessary, however, to use special relativity. In the case of a source moving relative to an observer, it is necessary to account for the effect of there being a difference between the proper time measured by the

moving source and the coordinate time measured in the observer's frame, which is commonly known as time dilation.

Let us quantitatively consider a light source moving directly towards or away from an observer with speed v, where positive v denote motion towards the observer, and let $\beta \equiv v/c$. Then, it may be shown [47] that the frequency ν in the observer's frame differs from the frequency in the source's frame ν_0:

$$\nu = \frac{\sqrt{1+\beta}}{\sqrt{1-\beta}}\nu_0 \tag{3.4}$$

If, however, the speed of the source is nonrelativistic, then $\beta \ll 1$ and Equation (3.4) may be simplified. Applying the binomial expansion and keeping terms only to first order in β,

$$\Delta\nu \equiv \nu - \nu_0 = \frac{v}{c}\nu_0 \tag{3.5}$$

Experimentally, we will be more interested in wavelength than frequency. Using the chain rule, and assuming $\Delta\nu$ to be small, we find that

$$\frac{\Delta\lambda}{\lambda} = -\frac{\Delta\nu}{\nu} \tag{3.6}$$

Thus we find that for plasma uniformly moving towards or away from the observer, a given spectral line will have its wavelength shifted with

$$\Delta\lambda = -\frac{v}{c}\lambda_0 \tag{3.7}$$

Thus far we have only considered the effect of a Doppler shift, implicitly assuming that all the emitting ions in the plasma have the same velocity. This is equivalent to assuming that the plasma has zero ion temperature, which is unphysical. Thus we must consider the effect of temperature, whereupon there will be a distribution of ion velocities. As the temperature increases, there is an increasing spread in the distribution of particle velocities. This leads to light emitted by individual ions having slightly different Doppler shifts, which results in the spectral line being Doppler broadened.

It may be shown that a plasma with some equilibrium ion temperature T is governed by the Maxwellian velocity distribution, $f(\mathbf{v})$. In this distribution, $f(\mathbf{v})\,d^3\mathbf{v}$ gives the mean number of particles per unit volume with velocity between $\mathbf{v}$ and $\mathbf{v} + d\mathbf{v}$. The Maxwellian distribution of particle velocities $\mathbf{v}$ for particles of mass m is given by [48]

$$f(\mathbf{v})\,d^3\mathbf{v} = n\left(\frac{m}{2\pi kT}\right)^{3/2} \exp\left[-\frac{m\mathbf{v}^2}{2kT}\right] d^3\mathbf{v} \tag{3.8}$$

where n is the number of particles per unit volume in the system.

In IDS, however, we observe Doppler shifts along a fixed line of sight. So, what we really need is not a distribution of 3-dimensional particle velocities $\mathbf{v}$ but the distribution of one component of velocity, the component along the line of sight. Calling this component v, we compute the distribution $f(v)$ by integrating (3.8) over 2 of the 3 velocity components. Then, in one dimension, the Maxwellian distribution of one component of velocity is given by

$$f(v)\,dv = n\left(\frac{m}{2\pi kT}\right)^{1/2} \exp\left[\frac{-mv^2}{2kT}\right] dv \tag{3.9}$$

Here m is the mass of the radiating impurity ion.

Now, we know from (3.5) that light of frequency ν will be emitted by particles moving with velocity $c[1 - \nu/\nu_0]$. Then, the intensity distribution of frequencies $I(\nu)$, which is the measured lineshape, may be given by substituting the above into (3.9), whereupon we find that

$$I(\nu) = I_0 \exp\left[-\frac{m(\nu_0 - \nu)^2 c^2}{2kT\nu_0^2}\right] \tag{3.10}$$

where I_0 is the peak intensity. This lineshape is a Gaussian whose width depends on T. Then, the full width at half maximum of this Gaussian, $\Delta\nu_{\text{FWHM}}$, is given by

$$\frac{\Delta\nu_{\text{FWHM}}}{\nu_0} = 2\left(\frac{2kT\ln 2}{mc^2}\right)^{1/2} \tag{3.11}$$

Of course, we may express the above in terms of wavelength, which will be of greater practical utility. Then,

$$\frac{\Delta\lambda_{\text{FWHM}}}{\lambda_0} = 2\left(\frac{2kT\ln 2}{mc^2}\right)^{1/2} \tag{3.12}$$

Measuring the line width will thus allow us to determine the ion temperature T, and measuring the line shift will allow us to determine the net flow velocity. Having familiarized ourselves with the basic physics involved, we now consider the optical elements involved in the IDS.

3.3   The Spectrometer

Our Ion Doppler Spectrometer is a 1.33 m McPherson Model 209 monochromator with a blazed echelle grating with 316 grooves/mm, operated at 25th order. The blaze angle is $\theta_b = 63.43°$. The spectrometer is in a Czerny-Turner configuration, which uses spherical focusing and collimating mirrors, and has $f/9.4$.

We proceed to analyze the diffraction problem. The geometry of the problem is shown in Fig. 3.2. With the echelle grating, we must distinguish between the normal to the grating and the normal to the blaze. In the subsequent analysis, we note that the incident and diffracted rays are on the same side of the grating normal, which is different from the situation usually shown in books on optics. We first derive the fundamental grating equation. Let the groove separation be d, and denote by θ_i and θ_d the angles of incidence and diffraction, measured relative to the grating normal. Consider the two rays marked 1 and 2. There are two path length differences for ray 1. First, ray 1 must travel a distance $d\sin\theta_i$ further than ray 2 to reach the grating. Then, to reach a point on a line perpendicular to the diffracted rays, ray 1 must travel $d\sin\theta_d$. Thus, the total path length difference between rays 1 and 2 is $d(\sin\theta_i + \sin\theta_d)$. Now, the nth order bright fringe will be observed when the total path length difference is an integer multiple of the wavelength of light being observed. Thus, for our geometry, the fundamental grating equation for the nth order bright is given by

$$n\lambda = d(\sin\theta_i + \sin\theta_d). \tag{3.13}$$
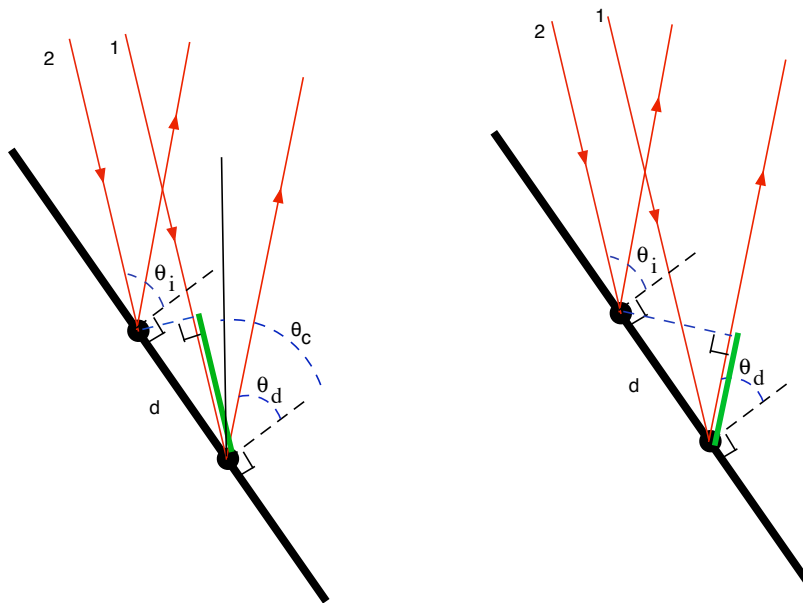
Figure 3.2: Geometric setup for diffraction problem. For the echelle grating used at SSX, both the incident and diffracted rays (shown in red) are on the same side of the grating normal. Here, the dashed black lines are normal to the grating, which has groove spacing d. For the sake of clarity, the blazes of the echelle grating are not shown. (left) Setup for calculation of first path length difference for Ray 1. The blue dashed line is perpendicular to the incident rays. The path length difference, shown by the green line, is $d\sin\theta_i$. We also show the angle bisector (solid black line) of the incident and diffracted rays, which makes angle θ_c with the grating normal. (right) Setup for calculation of the second path length difference for Ray 1. The blue dashed line here is perpendicular to the diffracted rays. The path length difference, again shown by the green line, is given by $d\sin\theta_d$.

Consider an auxiliary line bisecting the angle formed by the incident and diffracted rays. Let θ_c be the angle from the grating normal to this bisector. Then, defining $2\gamma \equiv \theta_d - \theta_i$, we have

$$\theta_i = \theta_c - \gamma \tag{3.14a}$$

$$\theta_d = \theta_c + \gamma \tag{3.14b}$$

Substituting these into 3.13 gives, after some algebra,

$$n\lambda = 2d \sin\theta_i \cos\gamma. \tag{3.15}$$

This equation shows that there is a linear relationship between $\sin\theta_i$ and $n\lambda$. Thus, if we can adjust $\sin\theta_i$, we can adjust the wavelength to which the spectrometer is tuned. This is the operating principle of the sine bar of the spectrometer, which rotates the grating, changing $\sin\theta_i$. The sine bar allows the adjustment of the grating angle through the use of a manual dial or with a stepper motor controller. We have found that using the stepper motor gives us more precise control over the grating angle.

3.4   Dispersion of Spectrometer

As described in the previous section, we may specify the wavelength at which the spectrometer is to observe by choice of $\sin\theta_i$. In practice, however, the light observed by the spectrometer will not always be monochromatic. Thus we wish to know what will happen when light of slightly a slightly different wavelength, say $\lambda + d\lambda$, is incident on the spectrometer.

Let us consider what happens for light that is not of the wavelength for which the spectrometer is set. In this case, we cannot use (3.15) but must use (3.13). From there we see that for the condition that the total path length difference be an integer multiple of the wavelength to hold, $\sin\theta_d$ must change.

From the design of the spectrometer, light of the wavelength for which the spectrometer is set reflects from the grating and is incident on the focusing mirror parallel to its optic axis. From geometric optics, such paraxial rays will then be focused to a point. But, rays that are incident on the mirror at a small angle θ from the optic axis will be focused not to a point on the optic axis but to a point a height x from the optic axis. Specifically, we have

$$x = \theta f \tag{3.16}$$

where f is the focal length of the mirror. This is the operating principle of the spectrometer: light of a different wavelength than what the instrument is set to will have a different θ_d and will show up at a different location governed by (3.16). We now define a quantity known as the dispersion, $D \equiv \frac{d\lambda}{dx}$, which tells how much spread in wavelength there is for a given displacement at the focal point of the focusing mirror. Using the chain rule, (3.13), and (3.16), we find

$$D = \frac{d \cos\theta_d}{nf} = \frac{d \cos(\theta_c + \gamma)}{nf} \tag{3.17}$$

where θ_c may be determined for a given wavelength setting from 3.13.

Now, it is possible to see why the IDS spectrometer is designed to operate at 25th order, for the dispersion improves for large n. It is to observe spectra at such high orders that the IDS spectrometer uses an echelle grating. The reflective grooves of the echelle grating are not flat, but are at a rather large blaze angle θ_b to the plane of the grating. Consequently, one can crudely think of the blazes as reflecting light to higher orders. More correctly, the blazes have a finite width and so diffraction from a single blaze must be taken into account through computing a blaze function, whose effects combine with the fundamental grating equation (3.13) to give the spectrometer output. A more thorough discussion of echelle gratings may be found in [49].

For SSX's spectrometer, we know that $\gamma = 4.98°$ and that $1/d = 316$ G/mm. Our mirrors have focal length 1.33 m. Given that we will be set to observe a 229.687 nm line at 25th order, we find then that at that wavelength,

$$D = 0.032 \text{ nm/mm} \tag{3.18}$$

at the output of the spectrometer.

3.5   Collection and Input Optics

Our collection optics consist of an aperture, an interference filter, a lens, and an optical fiber. Light is collected from a quartz vacuum window at the midplane of SSX. The collection optics are mounted on a pivoting arm that allows the selection of 10 different chords through the plasma, ranging from chords that are nearly radial to nearly tangential. The chords have equal angular spacing, but their spacing in terms of height from the diameter is not uniform.

The first optical element is an aperture stop. In conjunction with the lens and the small diameter of the fiber optic, it limits the angle of the cone of light collected by the spectrometer. The aperture has diameter 15 mm and is located at the focal point of the lens. Then, an interference filter then cuts out extraneous light not near the wavelength under observation. This is particularly necessary to ensure unambiguous interpretation of the spectra, because the grating equation (3.13) can have multiple solutions. That is, the spectrometer's image could contain lines from wavelengths far away from the desired wavelength, but at a different spectral order. The filter used for studying the C III 229.687 nm line has a center wavelength of 229.4 nm, FWHM of 10 nm, and peak transmission of 19%.

After passing through the filter, the light then passes through a plano-convex spherical lens, with focal length 74.2 mm and diameter 25.4 mm. This lens focuses the incident light rays, which may be thought of as parallel to the optical axis, into the entrance of the optical fiber. The fiber is located 2.8 mm past the rear focal point of the lens. The optical fiber itself is 1 m long with core diameter 0.6 mm and numerical aperture 0.22. The fiber has about 80% transmission in the UV.

We note here that the lenses used in the collection optics, as well as all the other lenses in the IDS optical system and the fiber optic, are made of UV-grade fused silica (UVGFS), which has good transmittance over the UV range. The UVGFS lenses have an index of refraction of 1.52 at 229.687 nm. For every UVGFS lens in the IDS system, we also possess a geometrically identical BK7 glass lens. When used for He-Ne laser light
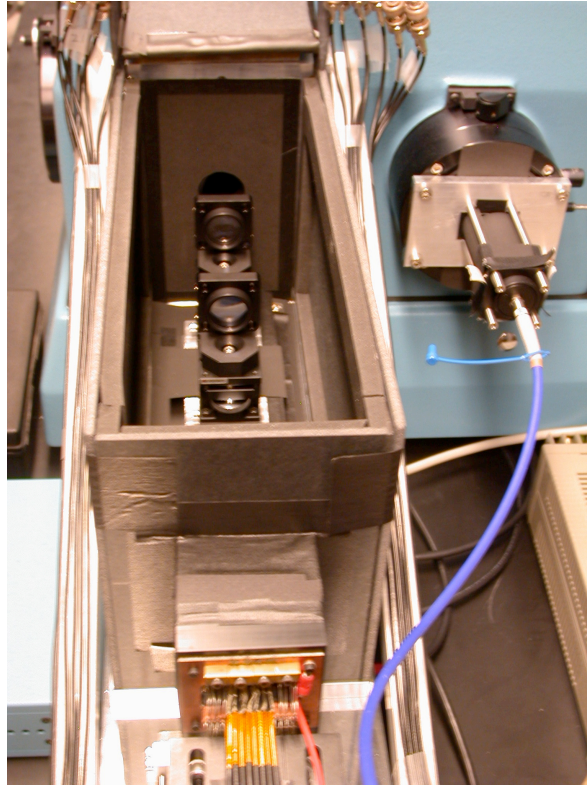
Figure 3.3: Photograph of the exit optics and PMT detector in the light-tight box with the top removed.

in the visible range ($\sim$ 632 nm), the BK7 lenses have the same index of refraction as the UVGFS lenses, and therefore should function the same optically. These lenses were purchased to allow us to perform initial alignment of the IDS optics with visible light from a He-Ne laser, as well as to enable studies of impurity lines in the visible in the future.

Finally, at the spectrometer end of the fiber optic, a 24.2 nm focal length spherical bi-convex lens magnifies the image that comes out of the fiber 2$\times$ before the light enters the spectrometer entrance slit.

3.6   Exit Optics

The output optics serve to magnify the output of the spectrometer 3.7$\times$, which is necessary since our detector has wide pixels. consist of two plano-convex spherical lenses. The focal plane of the spectrometer serves as the object plane for the two-lens system. The first lens is a 49.6 mm focal length lens whose flat surface is located 24.8 mm from the spectrometer focal plane. The second lens is a 99.0 mm focal length lens located 122.6 mm from the spectrometer focal plane. The detector is located 380 mm from the spectrometer focal plane; this distance optimizes the loss of spectral resolution due to poor imaging.

A photograph of the IDS exit optics is shown in Fig. 3.3.

3.7 The Detector, Electronics, and Data Acquisition

After passing through the exit optics, the spectral light is incident on our detector, which for SSX is a photomultiplier tube (PMT) array. The PMT array has large ($\sim$ 1 mm) pixels, which certainly poses challenges for use in an instrument with high spectral resolution. Other detector technologies that have often been used in plasma spectroscopy, such as gated charge-coupled device (CCD) arrays, offer greatly superior spatial resolution. The primary advantage of the PMT array over other technologies, and one of the primary reasons we chose to use it in SSX, is its rapid time response, which has given us submicrosecond time resolution necessary for observing changes in our plasma on the order of the Alfvén time.

For the reader unfamiliar with photomultiplier tubes, we give a brief overview of how they work. Incident photons strike a photocathode, made of a material exhibiting the photoelectric effect. The photocathode is limited by some quantum efficiency and does not output one photoelectron for every sufficiently energetic incident photon. After a photoelectron is ejected from the photocathode, it passes through what is called a *dynode chain.* The electrons are accelerated by some applied voltage from dynode to dynode. As electrons strike a dynode, they cause the dynode to emit a greater number of electrons. Thus, by having a series of dynodes, a measurable pulse of current is generated whenever an incident photon causes the emission of a photoelectron. The accelerating voltage between the dynodes is related to the gain of the PMT. PMT's generally exhibit linear behavior so long as the current in the dynode chain is not too large. Readers interested in learning more about the physics of PMT's are referred to the *RCA Photomultiplier Handbook* [50].

The PMT array used for the IDS experiments is a Hamamatsu H7260A-03 multi-anode PMT array with 32 channels spread in a continuous line. The pixels are 0.8 mm wide and 7 mm high, and the distance between the centers of neighboring pixels is 1 mm. Each pixel is its own PMT with its own dynode chain. Consequently, the response of the 32 channels is non-uniform and varies by up to 17%. Our data analysis codes correct for these non-uniformities based on measurements from the manufacturer. There is also a $\sim$3% cross-talk between neighboring channels. The quantum efficiency at 229.687 nm is about 5%, although the peak quantum efficiency of the tube, at 420 nm, is about 20%. The current pulse resulting from a single photoelectron entering the dynode chain has a 0.6 ns rise time and is 2 ns wide, giving us the fast time response we need.

The PMT array itself is mounted on a two-axis translation stage. This allows the tube to be moved along the optical axis for focusing, and in the dispersive direction to allow for proper optical alignment. The PMT array, translation stage, and exit optics are all enclosed in a light-tight box that we designed and constructed.

We used our LeCroy 100 MHz digital oscilloscopes to acquire the data. While the oscilloscopes had excellent time response and digitization characteristics, they could only acquire up to 12 channels at a time. We usually acquired the 12 channels closest to the center of the PMT array and terminated the rest with 100 Ω resistors; this was more than adequate to observe the desired spectral line fully even with its shifts

and broadening.

3.8   IDS Calibration

Calibration experiments were necessary for several reasons. First, the dispersion of the IDS had to be determined; this would allow the actual (as opposed to computed) magnification of the IDS optics to be determined precisely. Secondly, some sort of absolute wavelength calibration was necessary, to know where on the detector a spectral line with zero Doppler shift would appear. Thirdly, it was necessary to determine the instrument function of the optical system.

Preliminary calibration measurements were performed by manually rotating the grating using the sine bar. However, it was found that the motion of the mechanical dial was not always unambiguous, and so it was necessary to use the stepper motor controller to best control the grating rotation. Initially, when the stepper motor controller was not used, we used the oscilloscope to count the electrical pulses from PMT channels. This method is well described by Ó Murchadha, to which we refer the reader for the details [51]. Instead, when the stepper motor controller was used, we amplified the PMT output signal with a current preamplifier and collected the signal using a USB interface. The current preamplifier was used with a sensitivity ranging from 0.5 nA/V to 1 μA/V, but was typically operated around 10 nA/V.

We first describe the experiment to determine the dispersion. We used a boron hollow cathode lamp, which has spectral lines at 249.677 nm and 249.773 nm. The line spacing is sufficiently small for both lines to fit across the PMT at 23rd order. The separation of the lines at the PMT was found to be 10.38 $\pm$0.05 nm. We found the dispersion to be $9.25\pm0.05 \times 10^{-3}$ nm/mm at this wavelength and spectral order. Since we can find the dispersion at the spectrometer focal plane using (3.18), we can take the ratio of the measured dispersion at the detector to the computed dispersion at the spectrometer focal plane to find the magnification of the IDS exit optics. Since the dispersion at the spectrometer focal plane for this setting is found to be 0.0343 nm/mm, we find that the magnification of the exit optics is 3.70. This value agreed with the value computed from ray trace simulations done by C.D. Cothran. Thus, we are confident in our calculated dispersions. For the C III 229.687 nm line, after magnification, the dispersion is 8.5×10^{-3} nm/mm.

We now describe the absolute wavelength calibration of the IDS system. We used four spectral lamps in these studies: boron, cadmium, antimony, and mercury, and observed 11 different lines. Some of the lines were observed at multiple orders, for a total of 18 values of the dimensionless $n\lambda/d$. A list of these values is given in Table 3.1. The grating was rotated by the stepper motor while the single channel of the PMT closest to the optic axis was observed. We recorded the wavelength counter reading corresponding to the peak response for each spectral line. The expected counter reading for each line was computed, and we plot the differences in counter reading in Fig. 3.4. We find the residual of the plot to be less than $\pm2 \times 10^{-5}$, which gives us an uncertainty of ±6 km/s in our flow velocity measurements.

Finally, we describe our measurement of the instrument function. We rotated the grating to sweep the
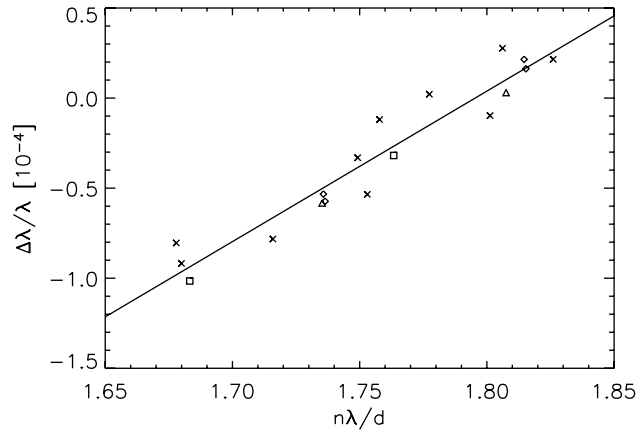
Figure 3.4: Fractional error $\Delta\lambda/\lambda$ for the mechanical wavelength counter plotted against $n\lambda/d$, which is independent of the grating angle. The plot shows a linear trend as $n\lambda/d$ increases, which is straightforward to correct. The diamond points are boron lines, the triangles are cadmium lines, the squares are mercury, and the ×'s are strontium. We note that for the C III 229.687 nm line at 25th order, $n\lambda/d = 1.81453$.

Source	Wavelength (nm)	Order	$n\lambda/d$
B	249.667	22	1.73568
B	249.667	23	1.81458
B	249.773	22	1.73642
B	249.773	23	1.81535
Cd	228.8022	24	1.73524
Cd	228.8022	25	1.80754
Hg	253.6521	21	1.68324
Hg	253.6521	22	1.76339
Sb	226.251	24	1.71589
Sb	230.646	24	1.74922
Sb	231.147	23	1.67998
Sb	231.147	24	1.75302
Sb	231.147	25	1.82606
Sb	244.551	23	1.77740
Sb	247.832	23	1.80124
Sb	252.852	21	1.67793
Sb	252.852	22	1.75783
Sb	259.805	22	1.80616

Table 3.1:
Spectral lines and orders observed during calibration measurements. The groove spacing d is 1/316 mm.
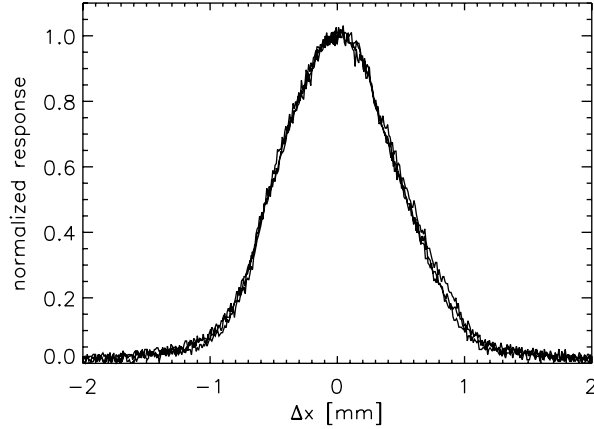
Figure 3.5: Instrument function of IDS system observed at 231.147 nm on the optical axis and at pixels ± 7 mm across the detector. Note that the three instrument functions are identical.

231.147 nm Sb line at 25th order across the PMT for the channel on the optical axis as well as channels 7 mm from the central channel on either side. The three instrument functions are shown centered over each other in Fig. 3.5. All three are clearly identical. Since the spectrometer's entrance slit is rectangular, one would expect the instrument function to be triangular. This is not quite the case. Still, computing the FWHM of the instrument function gives $\Delta x_{\mathrm{FWHM}} = 1.06$ mm. This allows us to compute a parameter called the resolving power, R:

$$R \equiv \lambda/\Delta\lambda_{\mathrm{FWHM}} \tag{3.19}$$

Converting this to wavelength using the predicted dispersion, we find the resolving power to be $R = 2.5 \times 10^4$.

We can also determine the instrument temperature of the IDS from the resolving power; the IDS cannot resolve any smaller temperature. Substituting R for the left side of (3.12) allows us to solve for kT_{inst}:

$$kT_{\mathrm{inst}} = \frac{1}{8\ln 2}R^2 mc^2 \tag{3.20}$$

From the measured instrument functions, we find $kT_{\mathrm{inst}} = 2.9$ eV. The instrument temperature for the C III line should be comparable to this.

Chapter 4

IDS Experiments in SSX

We begin this chapter by describing the SSX device in its current operational state. Along the way, we will briefly discuss the spheromak formation sequence in SSX. Then, for completeness, we will discuss the previous work done at SSX and what that has taught us about spheromaks and reconnection. This discussion is particularly important because it will guide our interpretation of the IDS results. Finally we will describe the actual experiments with single spheromaks, counter-helicity merging, and co-helicity merging for which IDS data has thus far been collected.

4.1   The SSX Device

A photograph of the SSX laboratory is shown in Fig. 4.1.

We first describe the SSX vacuum chamber. The vacuum chamber is cylindrical and is approximately 1 m long and 0.3 m in radius. The chamber is maintained at approximately 2×10^{-7} torr base vacuum pressure. Various vacuum ports at either end of the chamber and at the midplane allow the installation of diagnostics; it is through one such port that the IDS collects light. Inside the chamber, there are a pair of cylindrical copper containers called flux conservers of radius 0.2 m and total length 0.61 m. The flux conservers are coaxial and are installed at opposite ends of the vacuum chamber, with a 2 cm gap between the two flux conservers at the midplane to access the plasma for diagnosis. The flux conservers act as conducting boundaries that contain the plasma and provide the necessary boundary conditions for stable equilibria. A schematic diagram of the SSX experiment is shown in Fig. 4.2.

At either end of the vacuum chamber is a coaxial plasma gun; these form the spheromaks. The formation process is briefly reviewed in the next section. The energy that breaks down the hydrogen in the guns is provided by the large green capacitor banks shown in Fig. 4.1. SSX has 4 such banks, which each have a capacitance of 0.5 mF and may be charged up to 10 kV, for a maximum possible energy $\frac{1}{2}CV^2$ of 25 kJ per bank. In practice, however, only two of the four banks are in use at any time, and the banks are typically charged to about 5 kV. As we will discuss, the guns also require a "stuffing" magnetic field. These fields are created by the stuffing coils around each gun. The stuffing coils themselves are powered by a separate set of capacitors.
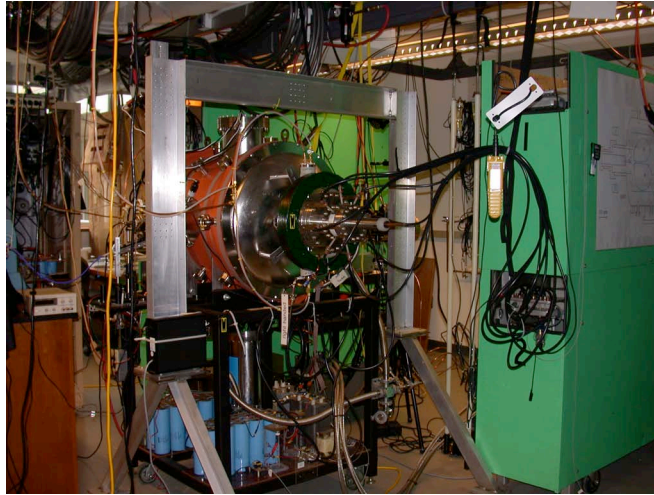
Figure 4.1: Photograph of the SSX laboratory. The vacuum chamber is shown at the center of the photograph. The metal yoke around the vacuum chamber is for a He-Ne laser quadrature interferometer for density measurements. One of the pairs of main capacitor banks (painted green) is at the right. The copper mesh screen room, housing data acquisition and control electronics, is visible in the background, as is the second pair of main capacitor banks.

c)
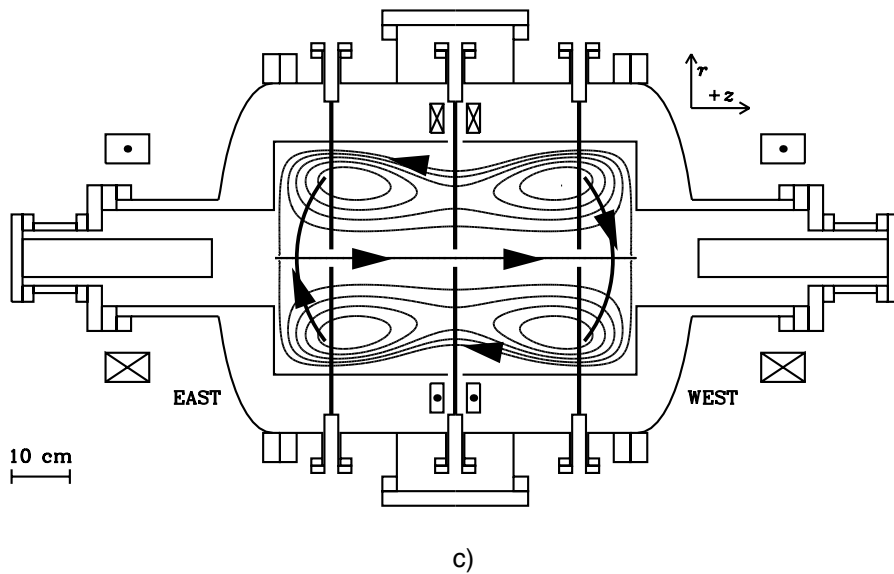
Figure 4.2: Schematic diagram of the SSX device. A side view is shown; the device is rotationally symmetric about the central horizontal axis of the figure. The coils for the guns are at the east and west ends of the device. The pair of coils near the midplane are the reconnection control coils (RCC's). Note the midplane gap in the flux conservers for diagnostic access. The figure shows a distributed array of magnetic probes inserted into the chamber, which were of critical importance in prior work. However, in the IDS experiments described here, there were no magnetic probes installed.

45

Furthermore, in its current configuration, SSX has a pair of reconnection control coils (RCC's) installed at the midplane. The RCC's carry a toroidal current, as shown in Fig. 4.2, and produce an poloidal magnetic field of up to 700 G at the central axis. The RCC's were installed to help stabilize the FRC's formed in counter helicity merging. The RCC coils are powered by yet another set of capacitors. The voltage on these capacitors is easily adjusted, allowing the control of the RCC field.

In addition to the IDS system, the primary diagnostics currently in use at SSX are a He-Ne quadrature interferometer and a soft x-ray detector. The details of the design and operation of these instruments are described by Gray [52] and Falk [53], respectively. The interferometer provides line-integrated measurements of plasma density, and the soft x-ray detector provides a rough measure of electron temperatures. Other diagnostics that have previously been used at SSX but are not presently in use include both distributed and high-resolution magnetic probe arrays, a Langmuir triple probe to measure local densities, a Mach probe to measure local flow, and a retarding grid energy analyzer for measuring energetic ions.

Recently, SSX has installed a new glow discharge cleaning (GDC) system to scour the vacuum chamber of impurities, resulting in lower densities and higher ion temperatures. Since the author was not involved in the design or construction of the GDC system, we do not discuss it in detail here. Essentially, the GDC system fills the SSX chamber with a DC helium glow discharge plasma. A DC voltage is applied across the electrodes of the plasma guns. Helium is introduced and is partially ionized; the ions are accelerated by the gun voltage. The GDC is used to clean the SSX before a day of experimental runs. In typical operation, the GDC uses 100 microtorr of helium with +300 V on the inner electrode and drawing ~ 0.1 A of current to scrub the vacuum chamber walls, for approximately 1 hour. After this, the polarity of the electrodes is reversed to scrub the guns themselves; in this regime, 800 microtorr of helium is used, and the maintenance of a -800 V bias draws 0.05 A of current. This is done for approximately 30 minutes.

Typical plasma parameters at SSX before the use of the GDC include electron density $n_e \sim 10^{15}$ cm^{-3}, temperature $T_i + T_e \sim 30$ eV, magnetic fields $|B| \sim 0.1$ T, and Lundquist number $S \sim 1000$. Preliminary studies indicate that with the use of the GDC system, $n_e \sim 10^{-14}$ cm^{-3}, and $T_i \sim 40$ eV.

4.2   Spheromak Formation

Here we briefly discuss how we form spheromaks in SSX using coaxial plasma guns. A diagram of the process is shown in Fig. 4.3. The guns consist of coaxial, cylindrical inner and outer electrodes. The outer electrode is grounded, while the inner electrode is at some adjustable voltage, which is usually approximately -5 kV peak before RLC decay, when the main capacitor banks discharge. The main capacitor banks are controlled independently. A coaxial, toroidal stuffing coil is external to the gun.

The timing and sequence of the formation process is as follows. We will define $t = 0$ as the time at which the main banks discharge. If the RCC coils are being used, their capacitors are discharged first, at some adjustable timing from $t = -100$ ms to $t = -25$ ms. Then, at $t = -25$ ms, the capacitors for the stuffing coils discharge, and the resulting toroidal stuffing current forms a dipole-like stuffing field. Typical stuffing
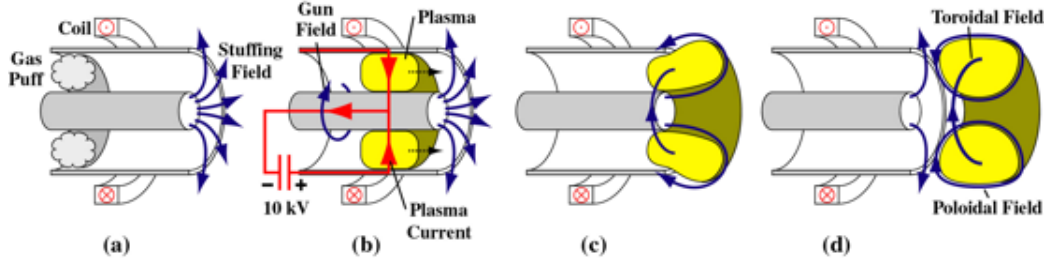
Figure 4.3: The spheromak formation process. (a) Gas is puffed into the space between the inner and outer electrodes, while the current in the stuffing coils forms a dipole-like stuffing field. (b) The main capacitor banks discharge. The gas ionizes, and carries a radial current between the inner and outer electrodes. The axial current along the inner electrode also creates a toroidal gun field. (c) The $\mathbf{J} \times \mathbf{B}$ force between the radial plasma current and the gun field accelerates the plasma out of the gun. (d) The plasma drags along the stuffing field, which reconnects to form the poloidal field of the spheromak.

fluxes in the gun are around 1 mWb. These two coils are energized well before the shot because it takes a comparatively long time for the magnetic flux to soak either into the gun or the chamber. Then, at about $t = -700$ μs, gas valves introduce hydrogen gas into the space between the inner and outer electrodes. This timing is limited by the sound speed of the gas, which takes some time to travel through the lines from the fast gas valves to the guns. Finally, at $t = 0$, the main capacitor banks discharge. Usually, it takes about 20 μs for the formed spheromaks to get out of the guns, and the plasma usually decays by about t=100 μs

When the main capacitor banks discharge, resulting in a high voltage between the inner and outer electrodes, the hydrogen gas between the electrodes ionizes and becomes an electrically conducting plasma. Then, there is a radial plasma current flowing from the outer electrode to the inner electrode. However, the current flowing down the inner electrode creates its own magnetic field, which forms approximately concentric circles around the electrode; this becomes the toroidal field of the spheromak. The $\mathbf{J} \times \mathbf{B}$ force resulting from the interaction of the plasma current and the toroidal magnetic field produced by the current in the inner electrode then accelerates the plasma out of the gun. As the plasma reaches the outside of the gun, however, the plasma runs into the field produced by the stuffing coil. The plasma basically drags the stuffing flux along (essentially due to the frozen-in flux constraint). Then, once there is enough magnetic pressure to stretch out and break off the stuffing field, the stuffing flux reconnects to form the poloidal field of the spheromak.

The polarity of the inner and outer electrodes of the guns cannot easily be changed, so the guns always produce similar toroidal fields. But, the direction of the current in the stuffing coils, the field from which generates the poloidal field of the spheromak, can be changed. This allows changing the direction of the stuffing flux changes the orientation of the poloidal field with respect to the toroidal field. The helicity of the spheromaks can thus be changed, and in particular it is possible to create both "left-handed" and "right-handed" spheromaks. Fig. 4.4 shows a left-handed spheromak. This allows SSX to study both co-helicity and counter-helicity merging, in which the merged spheromaks have the same and opposite handedness,
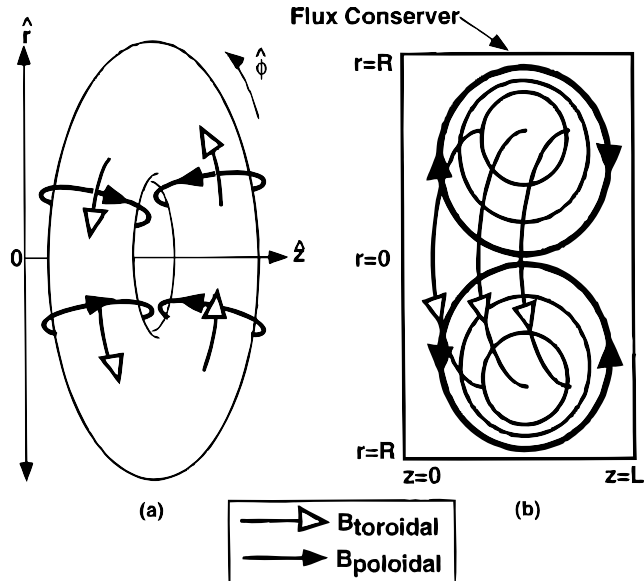
Figure 4.4: (a) and (b) Two views of the structure of a left-handed spheromak. A right-handed spheromak would have either the toroidal or the poloidal fields in the opposite direction. SSX reverses the direction of the poloidal field to produce right-handed spheromaks.

respectively.

Our discussion of the physics of spheromak formation in a coaxial gun has been highly qualitative. Readers interested in a more detailed theoretical treatment are referred to the discussions in Geddes [54] and Turner [55].

4.3 SSX: Prior Work

The SSX was constructed and first came online around 1995. Initially, SSX studied the dynamics and stability of single spheromaks [54]. The single spheromaks were fired into flux conservers of different sizes and diagnosed with magnetic probes, as shown in Fig. 4.5 (a) and (b). It was found that the equilibrium spheromaks were well described as force-free states according to (2.59): $\nabla \times \mathbf{B} = \lambda \mathbf{B}$.

These studies were soon followed by initial reconnection measurements. In these studies, individual flux conservers still surrounded each gun. Gaps in the walls of the flux conservers allowed the spheromaks to partially merge, as shown in Fig. 4.5 (c). In this arrangement, the poloidal and toroidal fields could locally reconnect. Kornack *et al.* studied energetic ions emerging from the midplane reconnection region with a retarding grid energy analyzer (RGEA). They found that a drop in the magnetic energy density correlated with a rise in the flux of outflowing ions moving near the Alfvén speed [56]. The reconnecting magnetic fields were also observed with a 2D probe array [57].

The next important subsequent development at SSX was the construction of a high resolution 3D magnetic
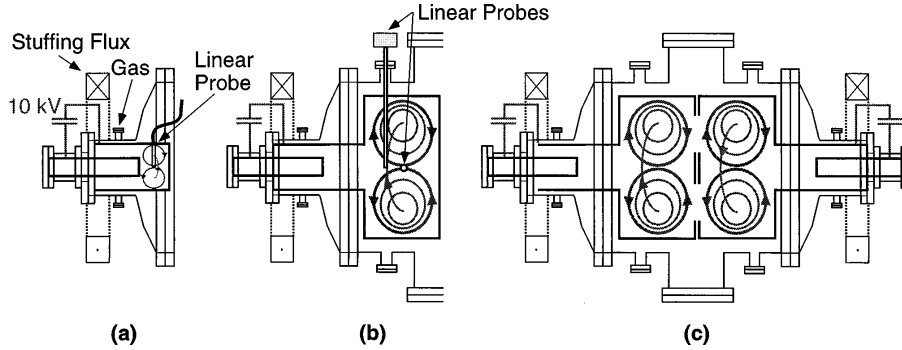
Figure 4.5: Previous configurations of the SSX chamber. (a) Small flux conserver (dark line) for single spheromak formation and equilibrium studies reported in [54]. (b) Large flux conserver for single spheromak studies. (c) Flux conservers with gaps to allow for partial spheromak merging in early reconnection studies.

probe and associated multiplexing data acquisition system by Landreman *et al.* [58] The probe measured 3 vector components of **B** at 200 closely spaced locations in the reconnection region and allowed unprecedented detailed studies of the local magnetic structure of reconnection during counter-helicity spheromak merging. In particular, the observed reconnection events were clearly not two-dimensional and had a significant component perpendicular to the plane of reconnection. Reconnection was also found to occur more rapidly for counter-helicity versus co-helicity flux tubes. Results from these measurements are reported in detail in [59] and [5].

SSX then turned to the study of full spheromak merging and the formation of field-reversed configurations (FRC's). The FRC is an axisymmetric, cylindrical, simply connected plasma with only a poloidal field. At this time, the flux conservers currently in use, which allow the spheromaks to merge fully, were installed. The midplane reconnection control coils were also installed. The magnetic structure of the full merging process was studied with a distributed probe array, with a plane of probes at the midplane and at both ends of the vacuum chamber. This allowed the detailed study of the global structure of reconnection. In addition, the high resolution probe array had a much greater perturbing effect on the plasma in this configuration. The distributed probe array allowed the magnetic fields to be Fourier analyzed. Counter-helicity merging was found to produce an FRC-like object that had little toroidal field in the center but retained a spheromak-like toroidal field at the ends. The FRC tended to remain stable for several Alfvén times before an increase in the $m = 1$ toroidal mode indicated that the FRC succumbed to the tilt instability. This was consistent with simulations. It was also found that co-helicity merging produced a single, long spheromak that rapidly tilted, in agreement with theory. Details of these studies may be found in [60].

4.4   Co-Helicity Shots

IDS data was taken on a number of chords for co-helicity merging prior to the use of GDC. With these shots and all others, the ion temperature and flow velocity were measured. Co-helicity shots were deemed to be

unsuitable for analysis with the Abel inversion discussed in the next chapter, however, as previous magnetic measurements indicated the presence of a strong tilt instability. The plasma would quickly fail to satisfy the Abel inversion's requirement of axisymmetry.

4.5   Counter-Helicity and Single Spheromak Shots

Counter-helicity shots were performed in some of the earliest measurements with the IDS. Light collected from all the chords was observed. After the installation of the GDC system, detailed scans through all the chords were made for the purpose of Abel inversion. In these scans, approximately 10 shots were taken at each chord.

Chapter 5

Results and Analysis

5.1 The Spectra

Recall that raw data from the PMT is digitized by our 100 MHz LeCroy oscilloscopes. We show a sample of the raw IDS data from four pixels below in Fig. 5.1. The data is from a counter-helicity shot and the light is collected along Chord # 3, which nearly passes through the center of the chamber. No GDC was used in the data presented in this section, or in any section until Sec. 5.5.

After it is saved, the data is processed by an IDL routine that reads in the data for each pixel, smoothes it into microsecond bins, and then displays the resulting spectra. The code also applies a correction for the non-uniform response of the pixels in the PMT array, with the correction data being provided by the manufacturer.

We display a sample spectrum in Fig. 5.2. Here, the lineshape is clearly Gaussian with a Doppler shift, as is visible from the overlaid Gaussian fit. The signal shown is the voltage reading from the oscilloscope, which is proportional to the photon count incident on each pixel, with the data binned into 1 μs bins. This effectively bins 10 data points together. Error bars would arise from the standard deviation of the binned data points; we do not plot them here since they are small. The flux of photons is sufficiently intense during all times of interest that rather than detecting individual electrical pulses due to incident photons, we measure an essentially continuous photocurrent. The horizontal axis is labeled in units of velocity, where we have used the dispersion of the system to measure the wavelength shift and (3.7) to convert it to a velocity.

5.2 Double-Peaked Spectra

At SSX, we have on numerous occasions observed double-peaked line structures during counter-helicity merging. We have not observed these structures during co-helicity merging or during single spheromak shots. An example of such a structure is shown in Fig. 5.3. Such a line structure clearly involves light with two different Doppler shifts, from plasma flowing both towards the observer and away from the observer. The flows we observe are nearly Alfvénic, up to about 0.6 v_A. We also note that these bi-directional structures are transient, usually not lasting for more than a few microseconds. During that time, they also evolve
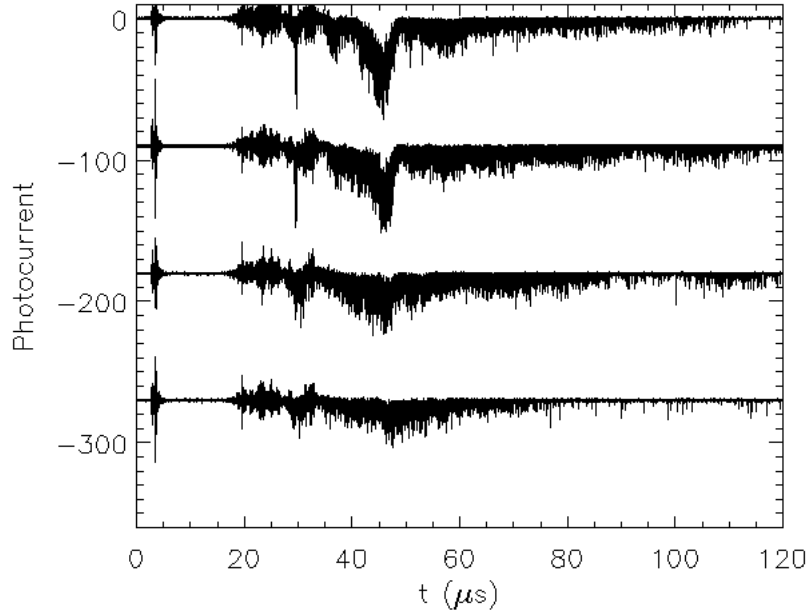
Figure 5.1: Raw signals from the four channels of the IDS closest to the optical axis during a counter-helicity shot, offset. During the shot, a chord that is almost a diameter was observed. On the horizontal axis, $t = 0$ corresponds to the time at which the banks fire. On the vertical axis, the separation between channels corresponds to 400 μA of photocurrent. We show only 4 channels here for clarity; up to to 12 channels are observed at any given time in practice.
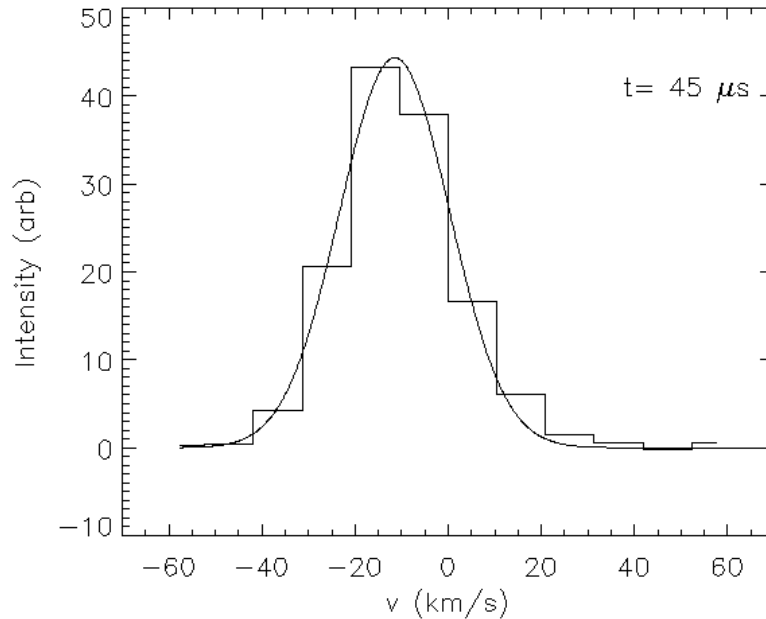
Figure 5.2: Spectrum from an IDS counter-helicity shot at $t = 45$ μs after the banks fire. This spectrum is taken from the same run as the raw data shown in Fig. 5.1. The points of the spectrum are shown as horizontal bars; we have overlaid a Gaussian fit to the data as a continuous line.

52
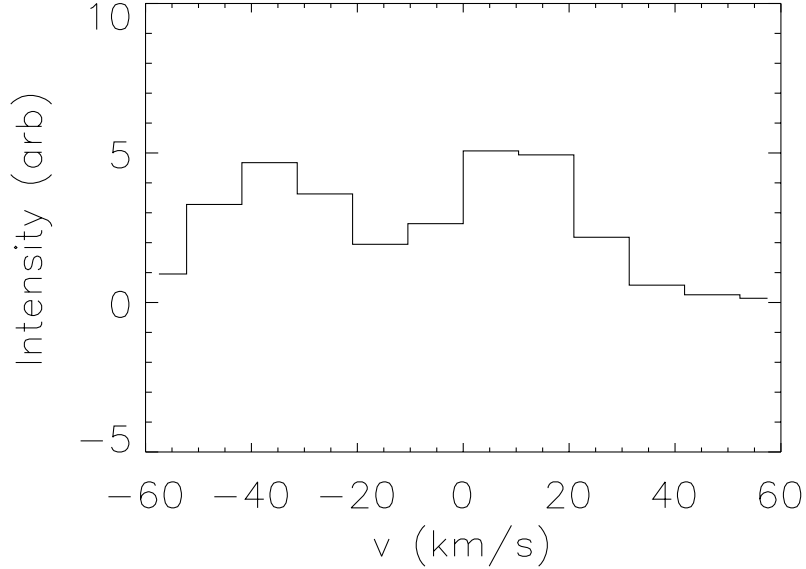
Figure 5.3: Typical double-peaked line structure arising during a counter-helicity shot.

rapidly. This is best illustrated through a time series of lineshapes, an example of which is shown in Fig. 5.4. We emphasize that the data shown are from a single counter-helicity shot.

5.3 Measuring Flow and Temperature

We can proceed to perform two other basic analyses. From computing the centroid (first moment) of the spectral line and calculating its shift, the flow velocity of the plasma can be determined. We show a plot of the flow velocity for the same counter-helicity shot in Fig. 5.5. In plots like this, data before about 30 μs and after about 80 μs should generally be neglected. Outside this time range, the amount of light collected from the plasma, which either has not fully reached the midplane or is decaying, is small. For such weak signals, minor fluctuations can give rise to large apparent shifts in the first moment.

We can also compute the second moment (standard deviation) of the data. Then, using (3.12), we can deduce the plasma ion temperature. A plot of T_i for the same counter-helicity shot is shown below in Fig. 5.6. As long as the lineshape remains roughly Gaussian, we can be confident in these temperature measurements. It is clearly observed, however, that sometimes the lineshape is not Gaussian. An example is shown in Fig. 5.7. Determining the plasma temperature by computing the second moment of this "flat-top" spectrum is likely to be erroneous. Such a line profile could arise if the flow along the chord was nonuniform. In particular, it is not difficult to imagine this profile resulting from the superposition of two Gaussian lines corresponding to light with different Doppler shifts. Clearly, simply computing the second moment of a double-peaked spectrum would also lead to an erroneous temperature measurement. The main ramification

53
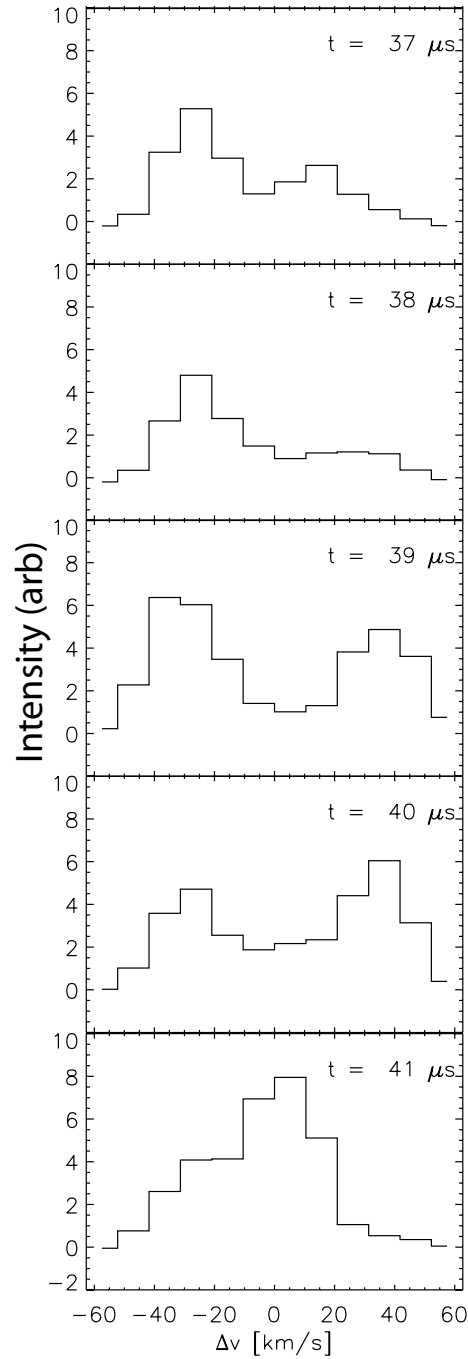
Figure 5.4: Time series of the evolution of the C III 229.687 nm line over a single counter-helicity shot. A double-peaked line structure suggestive of bi-directional plasma flow forms after 38 μs and decays at 41 μs. The structure evolves rapidly at the microsecond time scale. Such structures are frequently observed during counter-helicity merging.
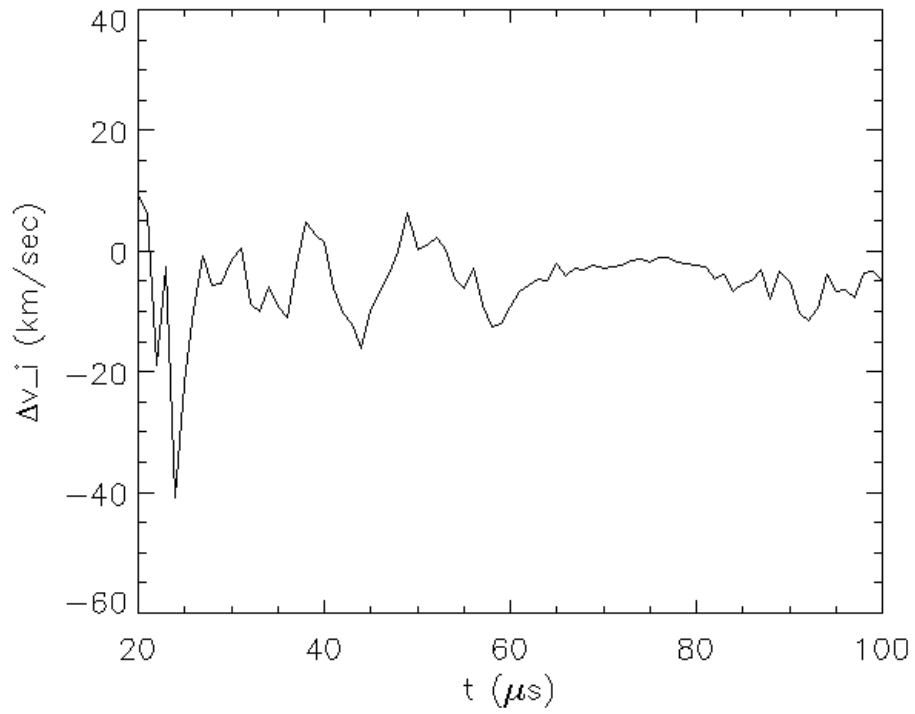
Figure 5.5: Flow profile from a counter-helicity shot.
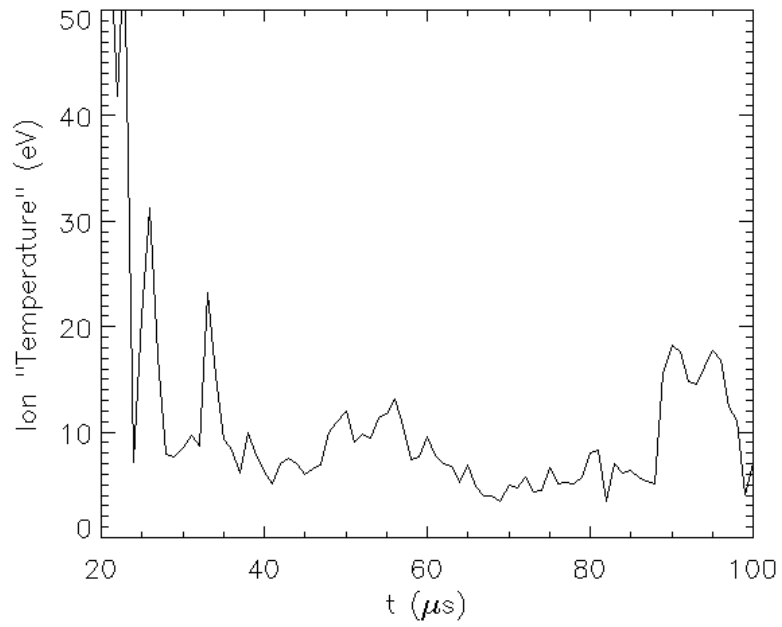
Figure 5.6: Temperature profile from a counter-helicity shot.
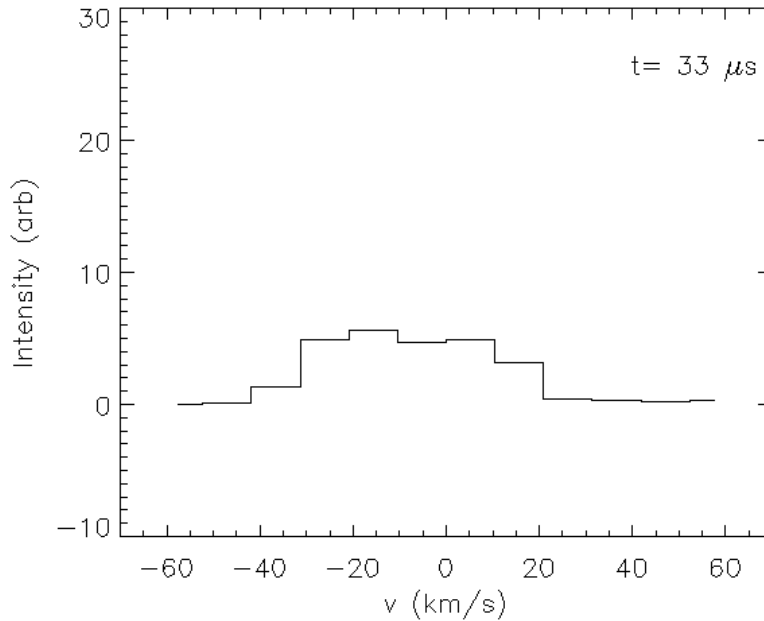
Figure 5.7: "Flat-top" spectrum from a counter-helicity shot. Computing the plasma temperature from the width of the line in this frame is probably erroneous.

of this is that our IDS temperature measurements should not always be interpreted literally.

5.4   Averaged Measurements and Fourier Analysis

We performed averaging of the flow and temperature profiles for several shots to determine if there was any global structure that could be determined. We display plots of averaged flow and temperature for a series of counter-helicity shots on Chord #3, which is nearly a diameter, below in Fig. 5.8 and Fig. 5.9, respectively.

To see if any general oscillations could be detected, we also performed Fourier decompositions of the averaged flow and ion temperature time histories. We display the results in Fig. 5.10 and Fig. 5.11, respectively.

5.5   The Abel Inversion

We have noted that in our IDS system we measure the relevant quantities (emissivity, flow velocities, and ion temperatures) integrated along a chord through the plasma. One would, however, like to have some more precise knowledge of how these quantities vary through the plasma. This is not an uncommon problem in plasma physics, and indeed in other areas of physics such as optics. If one is willing to make some strong assumptions, it turns out that there is a way to determine radial profiles of plasma quantities. This method is known as Abel inversion. Our discussion of the Abel inversion draws largely from Hutchinson [61].

56
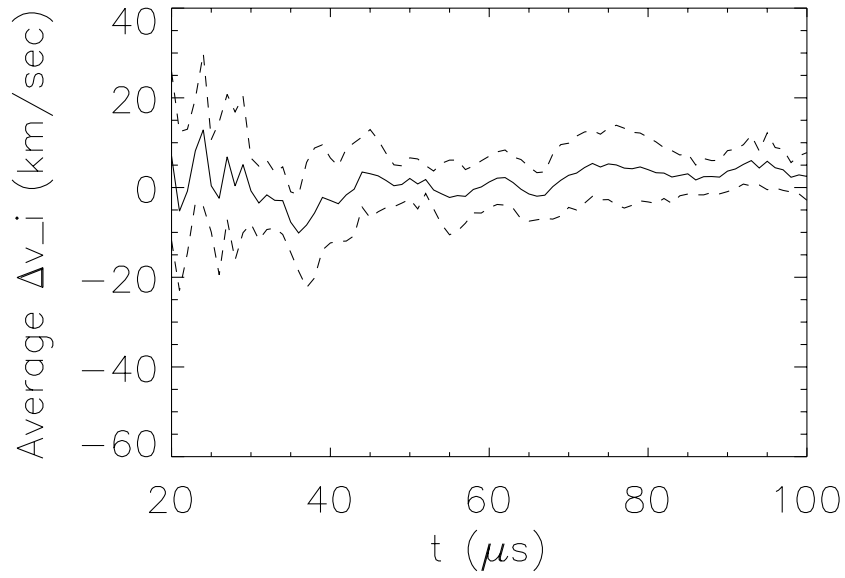
Figure 5.8: Time history of the average flow for 6 counter-helicity shots. The error is shown by the dashed lines, which represent the standard deviation of the flows.
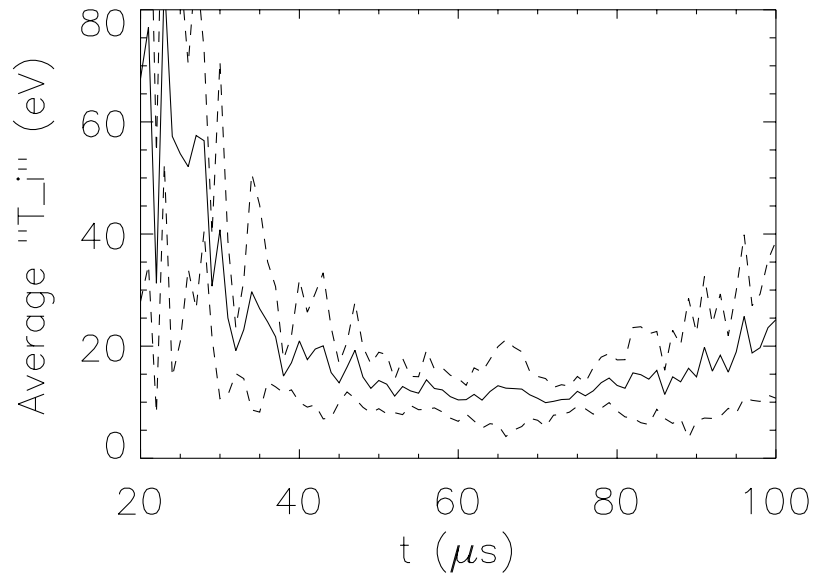
Figure 5.9: Time history of the average ion temperature for 6 counter-helicity shots. The error is shown by the dashed lines, which represent the standard deviation of the temperatures.

Flow Spectral Analysis
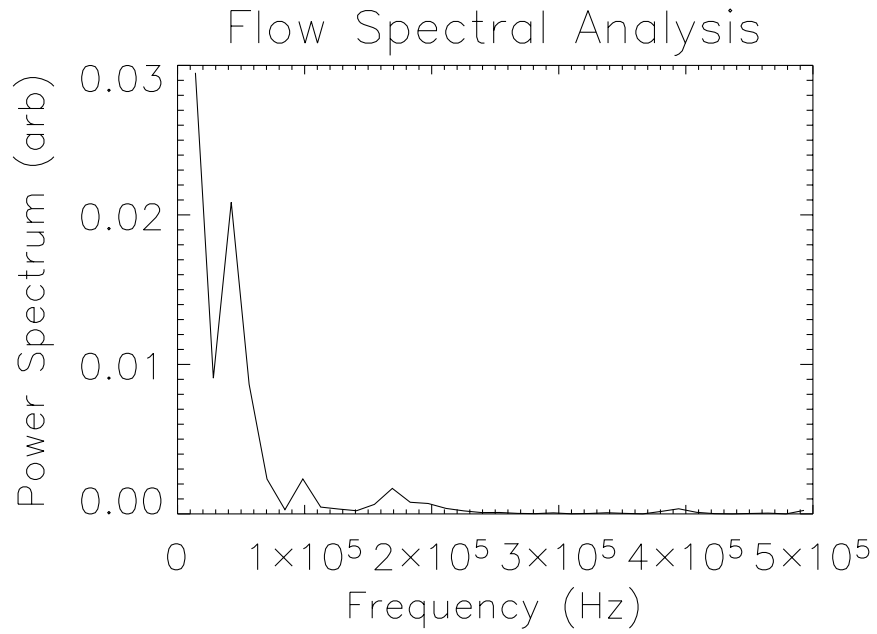
Figure 5.10: Fourier decomposition of the time history of the average flow for 6 counter-helicity shots.

Temperature Spectral Analysis
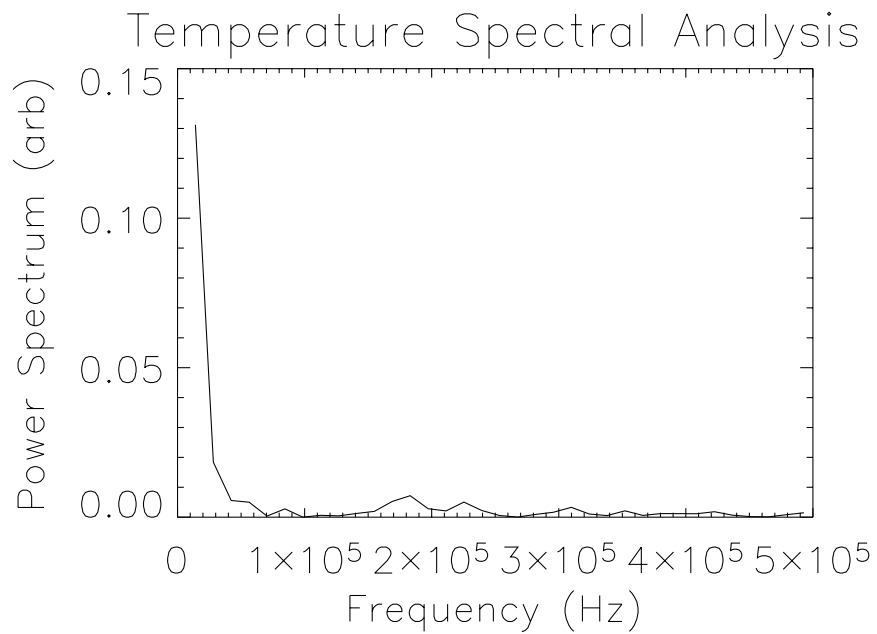
Figure 5.11: Fourier decomposition of the time history of the average ion temperature for 6 counter-helicity shots.

The two strongest assumptions of the Abel inversion are as follows. First, the plasma must be axisymmetric, such that any plasma quantity ϵ is only a function of the radial coordinate r. Secondly, $\epsilon(r)$ must vanish at the outer edge of the plasma.

Consider, then, a cylindrically symmetric plasma with radius R. We illustrate the relevant geometry in the figure. Suppose that we are interested in determining the radial profile of some plasma scalar quantity $\epsilon(r)$, but only have knowledge of chord-integrated measurements through a slice of the cylinder. Let $I(y)$ denote the measurements, where y is the height of the chord above the diameter. Also, let x describe the distance along the chord.

A chord-integrated measurement along a chord at height y is given by

$$I(y) = \int_{-\sqrt{R^2-y^2}}^{\sqrt{R^2-y^2}} \epsilon(r)\, dx. \tag{5.1}$$

Changing the variable of integration from x to r and using the condition of axisymmetry allows us to express the chord measurements as

$$I(y) = 2\int_{y}^{R} \frac{\epsilon(r)r\, dr}{\sqrt{r^2 - y^2}}. \tag{5.2}$$

The preceding equation (5.2) is known as Abel's integral equation and may be solved for $\epsilon(r)$. Although the proof is beyond the scope of this thesis[1], it can be shown that this equation has the solution

$$\epsilon(r) = -\frac{1}{\pi}\int_{r}^{R} \frac{dI}{dy} \frac{dy}{\sqrt{y^2 - r^2}} \tag{5.3}$$

so long as $\epsilon(R) = 0$. The result of (5.3) cannot be blindly applied, however, particularly in real experimental situations where one only has a finite number of measurements of $I(y)$. In particular, the derivative $\frac{dI}{dy}$ will tend to amplify any noise in the data.

5.6 Performing the Abel Inversion in SSX

Finding a fruitful algorithm to perform Abel inversion on actual plasma data, which is often noisy, is not as simple as the results of the last section might suggest. Many published algorithms for performing Abel inversions involve fitting $I(y)$ to various mathematical functions or expanding $I(y)$ in terms of a set of orthogonal functions, and then numerically applying (5.3) or a variant thereof. Such techniques include fitting with cubic polynomials [62], cubic splines [63], and expansion in terms of Hermite polynomials [64].

Given that Abel inversion might not be easy to perform with SSX data, due to the inversion method's assumption of axisymmetry, we felt that it would be best to try a simple algorithm first before committing to something that would be significantly more computationally intensive. We thus applied the geometric method for determining the Abel inversion of plasma emissivity described by Cho and Na [65].

Here we briefly describe the algorithm of Cho and Na as applied to cylindrical plasmas. In this algorithm, we assume the light comes from n evenly spaced chords through the plasma, with the chords separated by

---

[1]Or perhaps we should say that for readers who have way too much time on their hands, the proof is left as an exercise.
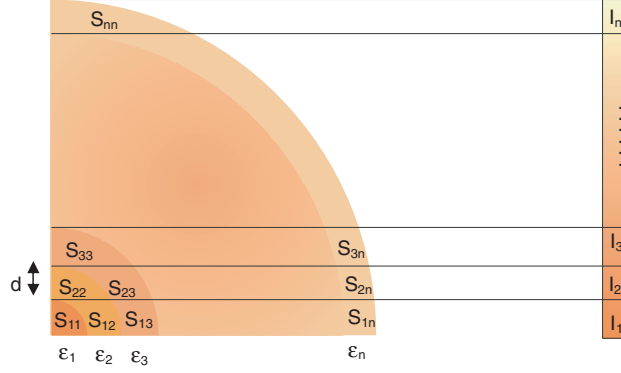
Figure 5.12: Geometrical setup for the Abel inversion algorithm of Cho and Na. They assume that one observes light from n evenly spaced chords through the plasma and thus measures the chord-integrated intensity I along n chords. They then divide the plasma into n annular rings and slice the annular rings for each chord. The resulting pieces of the plasma have area S_{ij}. A chord measurement I_j thus involves light coming from all the pieces along that chord. Figure from [65].

a distance d. We then divide our plasma into n concentric, annular rings of thickness d. Then, consider one quadrant of the cylinder and further divide the rings with horizontal, parallel slices at every chord height. Thus, the quadrant of the plasma is geometrically divided into pieces of area S_{ij}, where i denotes the ith radial ring and j the chord height. In the subsequent discussion we will use S_{ij} both to mean the area of the element and as a label to refer to the element with that area. This geometric division is shown in Fig. 5.12.

We label the chord-averaged measurements $I_1 \ldots I_n$. Then, all the plasma light influencing the measurement I_j comes from area elements $S_{jj}, S_{j+1,j}, \ldots, S_{jn}$ – that is, all the area elements along the chord. Let ϵ_m denote the value of the emissivity at the mth radial annular ring. Then it may be shown that

$$
\begin{aligned}
I_1 &= \frac{2}{d}(S_{11}\epsilon_1 + S_{12}\epsilon_2 + \ldots + S_{1n}\epsilon_n) \\
I_2 &= \frac{2}{d}(S_{22}\epsilon_2 + S_{23}\epsilon_3 + \ldots + S_{2n}\epsilon_n) \\
I_n &= \frac{2}{d}S_{nn}\epsilon_n
\end{aligned}
\tag{5.4}
$$

The preceding equations (5.4) essentially discretize (5.1). But, they may also be expressed as matrices:

$$
\begin{pmatrix} I_1 \\ I_2 \\ \vdots \\ I_n \end{pmatrix} = \frac{2}{d} \begin{pmatrix} S_{11} & S_{12} & \ldots & S_{1n} \\ 0 & S_{22} & \ldots & S_{2n} \\ \vdots & \vdots & \ddots & \vdots \\ 0 & 0 & \ldots & S_{nn} \end{pmatrix} \begin{pmatrix} \epsilon_1 \\ \epsilon_2 \\ \vdots \\ \epsilon_n \end{pmatrix}
\tag{5.5}
$$

Then the vector of emissivities is given by

$$
\overrightarrow{\epsilon} = \frac{d}{2}[S]^{-1}\overrightarrow{I}
\tag{5.6}
$$

It remains to geometrically compute the areas S_{ij}. It is straightforward to show that

$$
S_{ij} = \begin{cases} (P_{i,j} - P_{i+1,j}) - (P_{i,j-1} - P_{i+1,j-1}) & i \leq j \\ 0 & i > j \end{cases}
\tag{5.7}
$$

where

$$P_{ij} = \begin{cases} \frac{1}{2}(jd)^2\theta_{ij} - \frac{1}{2}((i-1)d)^2\tan(\theta_{ij}) & i \leq j \\ 0 & i > j \end{cases} \tag{5.8}$$

and

$$\theta_{ij} = \begin{cases} \cos^{-1}((i-1)/j) & i \leq j \\ 0 & i > j \end{cases} \tag{5.9}$$

This algorithm was implemented using an IDL code. The code `abelinvertmatrix.pro` computes the area matrix $[S]$. Then, the main code code `masterabel2.pro` reads in the data, calls `abelinvertmatrix.pro`, and performs the linear algebra needed to determine the inverted emissivity. These two codes are shown in Appendix D.

In practice, we begin with a set of Abel scan shots. For each of the 10 or so shots with the spectrometer observing a given chord, we compute the emissivity at every microsecond. We then perform an average over all of the shots on that chord to determine a smoothed chord emissivity for every microsecond. The emissivities are then further binned in time before they are read by `masterabel2.pro`. We have considered bins of 1, 2, 5, and 10 μs.

5.7   Results of the Abel Inversion

We present results from our Abel inversion of the plasma emissivity from single spheromak and counter-helicity shots. We show the results for the 5 μs time binning.

Fig. 5.13 shows a plot of the Abel inverted emissivity $\epsilon(r)$ for a single spheromak shot at $t = 35$ μs. Fig. 5.14 shows the Abel inverted emissivity for a counter-helicity shot at $t = 45$ μs. The dashed lines shown are the errors.

We computed the errors in these figures as follows. When we averaged together all the runs that collected IDS data from a single chord, we computed the standard deviation at each time interval. This random error was much larger than any other source of error that could be realistically included in the analysis. We thus had an error vector corresponding to the chord-averaged emissivities, $\vec{\sigma_I}$. Since each element in the output radial emissivity vector is a weighted sum of elements of the chord emissivity vector, we can apply the standard error propagation formula. Specifically, the error in the radial emissivity $\vec{\sigma_\epsilon}$ is given by

$$\vec{\sigma_\epsilon} = \sqrt{\frac{d^2}{4}[S^2]^{-1}\vec{\sigma_I^2}} \tag{5.10}$$

Here, the square root represents taking the square root of every element in the vector resulting from the matrix multiplication under the square root, $\vec{I^2}$ is the vector in which every element of $\vec{\sigma_I}$ is squared, and likewise $[S^2]^{-1}$ is the matrix in which every element of $[S]^{-1}$ is squared. Note that due to the diagonal nature of the matrix $[S]$, computing radial emissivities near $r = 0$ involve summing over more terms. Consequently, the error in the terms near $r = 0$ is comparatively larger. One problem to note in this analysis is that the emissivity is not constrained to be positive. Thus negative emissivities arise, as is the case in 5.14. This is of course unphysical.

61
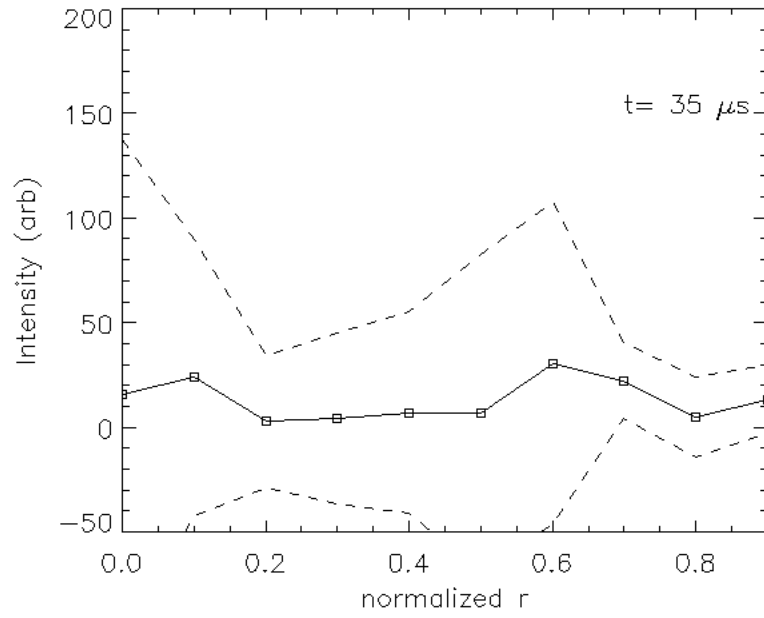
Figure 5.13: Abel inverted emissivity for a single spheromak shot.
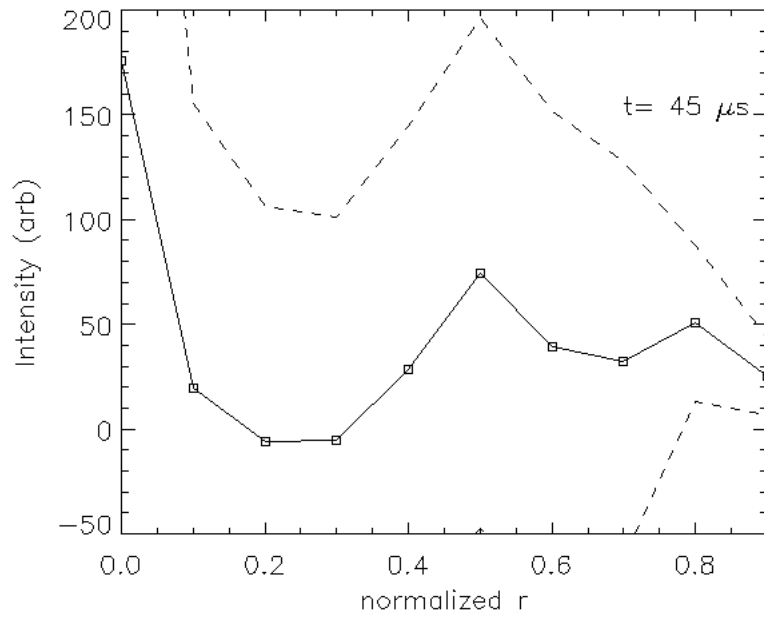
Figure 5.14: Abel inverted emissivity for a counter-helicity shot.

Chapter 6

Discussion and Conclusions

6.1 Interpretation of Spectra

We must keep several things in mind when interpreting the IDS spectra. First, it is open to question whether or not the carbon impurity ions are effectively in equilibrium with the majority hydrogen ions. We thus show in Appendix A that the collision time in the SSX plasma between C III ions and the majority hydrogen ions in the plasma is approximately 0.2 μs. So, when we observe dynamics on the microsecond time scale, it is a fairly safe assumption that the emitting carbon ions are in equilibrium with the majority ions[1].

Also, if we are to measure temperature by Doppler broadening, we must be sure to account for other broadening effects. We show in Appendix B that natural broadening, pressure broadening, and Zeeman broadening are negligible. Since the instrument function is approximately Gaussian, we may merely subtract off the instrument temperature from the measured standard deviations of the spectral lines, rather than going through a formal deconvolution. We also show in Appendix C that atmospheric fluctuations in the laboratory should not affect our results. However, in looking at these spectra, it is important to remember that they are from light collected not from a localized volume of plasma, but rather from light coming from a chord in the plasma. In particular, it would seem unphysical to assume that when the IDS observes a Doppler shifted line, all the plasma along the chord is flowing at the same speed. This should be kept in mind when interpreting our data, and highlights the need for some sort of inversion technique.

6.2 Flow

The role of flow in reconnection is clearly important, as evidenced by the Sweet-Parker model. At SSX, however, flow may be important after most of the reconnection has occurred as well. Here we describe one possible model for the generation of sheared flow during counter-helicity merging shots at late times.

The following argument, suggested by M.J. Schaffer, concerns sheared flow in an FRC. Previous magnetic measurements have shown that toroidal fields remain near the ends of the FRC's made by spheromak merging

---

[1] In another favorite analogy of M. Brown, the impurity ions may be thought of as being carried along with the plasma even though they are much more massive than the majority ions, much as both heavy cars and lightweight debris are swept away by the destructive waters of a tsunami.
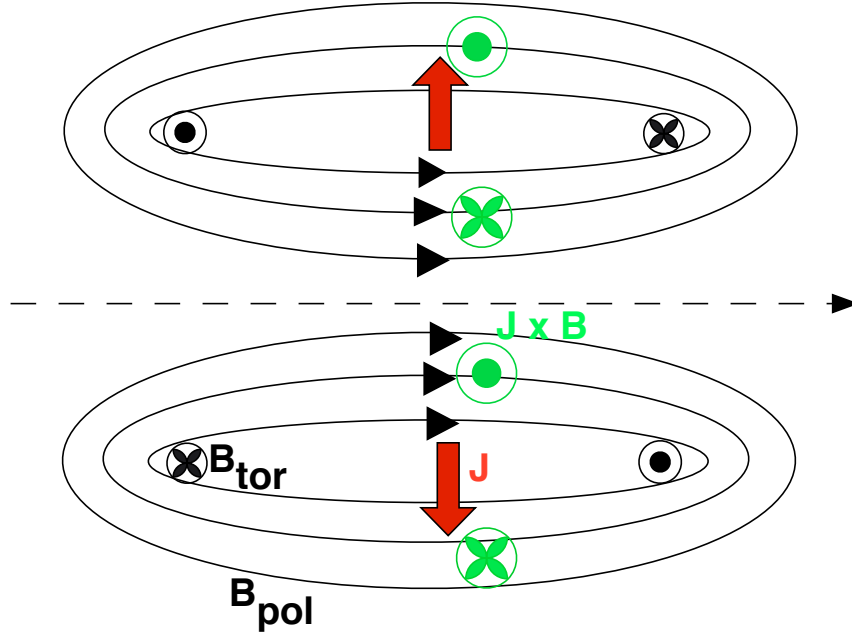
Figure 6.1: Diagram for argument that sheared flows may exist in SSX during counter-helicity merging shots. Magnetic field lines and vectors are shown in black. Currents are shown in red, and the resulting $\mathbf{J} \times \mathbf{B}$ forces are shown in green.

at SSX. The physical situation is shown in Fig. 6.1. Looking at the remaining toroidal field, it is clear that there must be a radial current density as shown by the red arrows due to Ampère's law. This current, however, will interact with the poloidal magnetic field of the FRC, producing a $\mathbf{J} \times \mathbf{B}$ force. The directions of the $\mathbf{J} \times \mathbf{B}$ vectors are shown in green; these are forces that will act on the plasma. Note that the $\mathbf{J} \times \mathbf{B}$ force will tend to exert a torque plasma near the central axis and plasma far from the central axis in opposite directions. These torques must be counteracted for a plasma in mechanical equilibrium; viscous drag resulting from sheared flow could do it. A three-dimensional diagram of the same physics is shown in 6.2.

What is particularly heartening is that preliminary simulations of SSX performed at PPPL have shown that sheared magnetic field lines corresponding to magnetic field being dragged along with a plasma with this flow profile are possible. On the other hand, IDS observations along nearly tangential chords have not indicated persistent strong toroidal flows. This does cast some doubt on the hypothesis. Still, SSX will continue to study this possibility in more detail in the future.

6.3 Bi-Directional Flows

We believe that the double-peaked spectra described in Sec. 5.2 are due to bi-directional flows resulting from magnetic reconnection. Recall that such flows were observed by Innes *et al.* on the sun. If our double-peaked
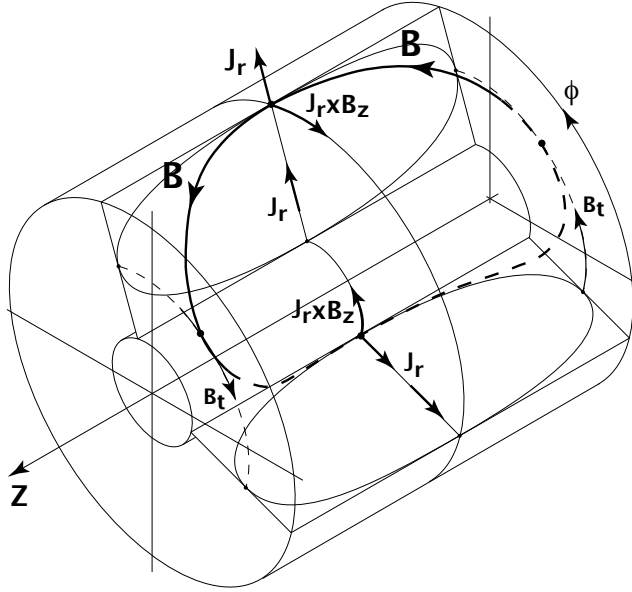
Figure 6.2: Another view of the possible sheared flow in the FRC's made at SSX.

spectra are indeed due to reconnection outflows, they would be the first measurements of such outflows in the laboratory.

It seems clear that the observed double-peaked lineshapes are due to bi-directional plasma flows; no other effects could be reasonably supposed to be responsible for them. But are these flows due to reconnection? During these runs, no magnetic diagnostics were installed at SSX. Without direct magnetic evidence, the onset of these flows cannot be correlated with reconnection with absolute certainty.

It appears unlikely, however, that these flows could be caused by anything other than reconnection. First of all, these double-peaked structures are not observed during single spheromak and co-helicity shots. In these shots, significant reconnection of the poloidal fields does not occur; this provides perhaps the strongest indirect evidence that the observed bi-directional flows are correlated with reconnection. Moreover, the timing of these events, which typically occur around 40 ± 10 μs after the banks fire, matches the timing of reconnection as measured when SSX operated with full merging with the distributed probe array.

These events, as well as their relationship to reconnection, clearly warrant further study. Incontrovertibly correlating these flows with reconnection observed using magnetic probes at the midplane may be difficult. In particular, fully inserting the complete set of distributed probes at the midplane would interfere with the line of sight of the IDS. The argument that the bi-directional flows at about the same time as reconnection could also be suspect if the plasma dynamics in these studies, without magnetic probes in the SSX, differ from those previously observed. This cannot be ruled out since the magnetic probes surely exert at least some perturbation on the plasma through, for instance, the formation of a sheath. But while further investigation is necessary, there does not at present seem to be any strong competing hypothesis for the cause of these

observed bi-directional flows other than magnetic reconnection.

6.4   Fourier Analysis

The results of the Fourier analysis are preliminary but at least seem plausible. It is of interest to note that the three peaks in Fig.5.10 are located at 0.42, 0.98, and 1.68×10^5 Hz. The values are not exact, but the frequencies are approximately related by a factor of 2. Moreover, recall that the Alfvén speed in SSX is approximately 10^5 m/s. Since the length scale at SSX is about 1 m, $1/\tau_A$ is on the same order of magnitude as the frequencies shown in Fig.5.10.

The cause of the periodic behavior, if it indeed exists, is not immediately clear. If most of the light is emitted where reconnection is occurring, then perhaps the periodicity in flow could be caused by some global oscillation in the plasma that causes the reconnection region to move in and out of the line of sight. A plasma rotating around the machine near the Alfvén speed could give rise to behavior with about the right frequency, but this seems less physically plausible.

We also note that the peak in Fig. 5.11 near 1.8×10^5 Hz is close to the last significant flow Fourier peak. The behavior here is not very clear. Further studies, particularly with magnetic probes in the plasma, may yield further insight, and this method of analysis might perhaps be more definitively tied to something physical.

6.5   Abel Inversion

The plasma emissivity depends on temperature and density and as such is a quantity worth examining. Abel inversions at SSX have also been performed with a different algorithm which models the *output* radial emissivities as cubic splines and adjusts their parameters to fit the data. Qualitatively, the inversion results from the method described here are generally consistent with the cubic spline method, although the cubic spline results are much smoother. One problem with the method described in this thesis, which essentially discretizes the Abel integral, is that the value of the emissivity at $r = 0$ is not constrained in any way, as mathematically required in the solution of the Abel integral equation.

While this analysis has been useful, extending it to other plasma parameters would not be easy. Even this has been difficult; particularly for counter-helicity merging, the shot-to-shot variability is sufficiently large that the error bars are often larger than the size of the measurement. The other parameters we would be most interested in inverting would be flow and temperature. Inverting the flow would require a robust knowledge of where the light was coming from – that is, the inverted emissivity. Moreover, flow is inherently a *vector* quantity; it would be necessary to somehow separate the contributions of different components of the vector flow from different elements of the plasma to the composite lineshape. Inverting the temperature would require knowledge of the inverted flow as well, and would be most difficult to invert. In particular, sheared flows along the line of sight could give rise to spectral broadening, so any inversion of temperature

would have to separate this effect from Doppler broadening. The temperature measurements are themselves sometimes difficult to interpret, particularly for counter-helicity shots with "flat-top" and double-peaked spectra that cannot be well-described by a single Gaussian. Finally, one must recall that the entire Abel inversion relies on an assumption of axisymmetry, the validity of which in SSX is questionable at best, particularly late in time for counter-helicity shots.

There are spectroscopic plasma diagnostics that get around the difficulties mentioned here by making local measurements. One example is the IDS probe used at Madison and on MRX. Such a probe, however, would likely exert a significant perturbation on the plasma because of its size. Other spectroscopic diagnostic techniques that make local measurements exist as well. CHERS, or charge exchange recombination spectroscopy, involves injecting a neutral beam of atoms into the plasma. The atoms in the neutral beam interact with the charges in the plasma and radiate. By having an IDS line of sight perpendicular to the atomic beam, one can be certain that the observed radiation is coming from the region in which the atomic beam and the line of sight cross. A similar technique called laser induced fluorescence (LIF) uses a laser to excite transitions in the plasma. An IDS line of sight perpendicular to the laser beam would also be capable of making a localized spectroscopic measurement. Both of these techniques are discussed in some more detail by Hutchinson [61]. Unfortunately, both CHERS and LIF require a significant investment in costly equipment, and thus would not be practical to implement on SSX in the near future.

6.6   Future Work

Much remains to be done with the IDS instrument experimentally. Thus far, only the C III 229.687 line has been observed in the plasma, although we have all the equipment necessary to study other UV and visible lines. Other impurities such as oxygen and nitrogen are known to exist in the IDS plasma. One interesting study would be to compare flows and temperatures measured by observing light from different atoms. In the future, it might also be more suitable to dope the SSX plasma with a carbon-containing gas, such as methane, which would provide better control over the amount of impurity in the plasma.

Of primary importance, however, will be the re-installation of magnetic probes and their use alongside the spectroscopic measurements. This will perhaps allow the correlation of events such as the bi-directional flows with magnetic reconnection. Currently, fine magnetic probes to better resolve small-scale magnetic structure are under development. Secondly, more extensive studies of the plasmas formed after glow discharge cleaning will be necessary. Preliminary results indicate that the GDC allows the SSX to access lower plasma densities and higher ion temperatures. It is not yet known, however, how the GDC affects electron temperature. In general, the details of reconnection in the plasma after GDC remain to be studied.

The Abel inversion discussed in this thesis clearly has only limited utility for determining radial profiles of flow and ion temperature. Other numerical techniques for interpreting the IDS data should be investigated.

Finally, it will be of great interest to compare the experimental results of SSX with custom simulations. Collaborations to simulate SSX are already in place with PPPL and the University of Wisconsin, Madison

through the recently-formed CMSO (Center for Magnetic Self-Organization). In particular, it may be very interesting to combine simulation results and a spectral emission model to calculate what an IDS system would theoretically observe, and compare this with what the IDS actually does see.

6.7   Concluding Summary

We have constructed and calibrated a new high-resolution ion Doppler spectroscopy system at SSX. Using this system, we have measured chord-averaged flows and ion temperatures. We have also made pioneering measurements of bi-directional flows due to magnetic reconnection in a laboratory plasma. An Abel inversion of the plasma emissivity has been performed. Now that a significant amount of experience has been gained with the IDS system at SSX, it is hoped that this will remain a fruitful diagnostic in the future.

Appendix A

IDS Confidence Check: Calculation of Collision Frequency

We have been interested in measuring the temperature of the SSX hydrogen plasma by ion Doppler spectroscopy using carbon ions. The astute reader might have noted that what really is being measured is the temperature of the carbon ions, and might be wondering whether the impurity ion temperature $T_{i,imp}$ measured through Doppler broadening is a good measure of the majority ion temperature $T_{i,maj}$ that is what we are trying to diagnose. This is a legitimate concern which we address in this Appendix.

The question at hand is essentially this: are the carbon ions in thermal equilibrium with the majority hydrogen ions? We will argue that they are by computing a collision frequency for impurity ion–majority ion collisions, and showing that the collisions occur faster than any relevant timescale in the plasma. First, however, we must derive an expression for the collision frequency.

A.1 Derivation of Collision Frequency

The derivation here closely follows that of Hutchinson [61], in particular as outlined in his Problem 6.12. We will calculate the rate dW/dt at which the impurity ions gain energy from collisions with majority ions. Then we will take $(dW/dt)/kT_{i,maj}$ as the effective collision frequency[1].

We first consider the dynamics of a single collision between a massive impurity ion of mass m_i and charge eZ_i, and a majority ion of mass m_m and charge eZ_m. The interaction between the majority and impurity ion is dominated by the Coulomb force. The interaction potential is just

$$U = -\frac{1}{4\pi\epsilon_0}\frac{Z_i Z_m e^2}{r} = -\frac{\kappa}{r} \tag{A.1}$$

where we define $\kappa \equiv \frac{Z_i Z_m e^2}{4\pi\epsilon_0}$. We consider the majority ion to be scattering off a much more massive impurity ion. This problem, the Rutherford scattering problem, is treated in most texts on classical mechanics, such as Thornton [47]. If we assume that the impurity ion is immobile, then from classical mechanics, it is possible to show by invoking conservation of energy and angular momentum that the momentum p transferred in the

---

[1]Since $kT_{i,maj}$ has units of energy, our proposed effective collision frequency has the correct units of time^{-1}.

collision is

$$p = \frac{2\kappa}{vb} \tag{A.2}$$

where v is the speed of the incident majority ion and b is the impact parameter for the collision. The energy W transferred in a single collision is just $p^2/2m_i$, so

$$dW_{indiv} = \frac{2\kappa^2}{m_i v^2 b^2} \tag{A.3}$$

Now, we must find the total energy transferred in unit time when there are many incident majority ions. In particular, we need to integrate (A.3) over b and v.

To do the integration over b, we will consider an annulus of space with a given impact parameter. The differential area of this annulus is $2\pi b\, db$. In unit time dt the effective volume occupied by scattering particles is $v\, dt$. Finally, assuming a Maxwellian speed distribution, the density of ions with speed v is given by $f(v)\, dv$, where

$$f(v)\, dv = 4\pi n_i \left(\frac{m_m}{2\pi k T_i} \right)^{3/2} v^2 \exp\left[-\frac{m_m v^2}{2kT_i} \right] dv \tag{A.4}$$

Here we are taking n_i and T_i to be the majority ion density and temperature in the plasma. Then, the total energy gained in unit time is

$$dW = dW_{indiv}\, 2\pi b\, db\, v\, dt\, f(v)\, dv \tag{A.5}$$

Dividing through by dt and integrating over all impact parameters and speeds, we find

$$\frac{dW}{dt} = \frac{(4\pi)^2 \kappa^2 n_i}{m_i} \left(\frac{m_m}{2\pi k T_i} \right)^{3/2} \int_{b_0}^{\infty} db \int_0^{\infty} v \exp\left[-\frac{m_m v^2}{2kT_i} \right] dv \tag{A.6}$$

Let us first look at the integral over b. We have taken the lower limit to be b_0, the closest distance a majority ion with speed v can approach the impurity ion. Even so, this integral unfortunately diverges. But should we really be integrating up to $b = \infty$? Indeed not, Debye shielding will prevent the impurity ion from feeling the electrostatic influence of very distant majority ions. Thus it is customary to cut off this integral at some maximal b_{max}. The result of the integral over b is then called the Coulomb logarithm, $\ln \Lambda$, where $\Lambda \equiv b_{max}/b_0$. The Coulomb logarithm depends on the plasma density and temperature but turns out to be relatively insensitive even to order of magnitude variations in these parameters. The interested reader is referred to Goldston [2] for further discussion of the Coulomb logarithm.

The integral over v, fortunately, is much easier to deal with and is found in standard tables. Then, substituting for κ, we find that

$$\frac{dW}{dt} = \left(\frac{Z_i Z_m e^2}{4\pi\epsilon_0} \right)^2 \frac{8\pi n_i}{m_i} \left(\frac{m_m}{2\pi k T_i} \right)^{1/2} \ln \Lambda \tag{A.7}$$

Now, dividing by kT_i, and rearranging to make the functional dependences as clear as possible, we find the collision frequency to be

$$\nu = \left(\frac{e^2}{4\pi\epsilon_0} \right)^2 \frac{8\sqrt{\pi}}{\sqrt{2}} Z_i^2 Z_m^2 \frac{\sqrt{m_m}}{m_i} \frac{n_i}{(kT_i)^{3/2}} \ln \Lambda \tag{A.8}$$

70
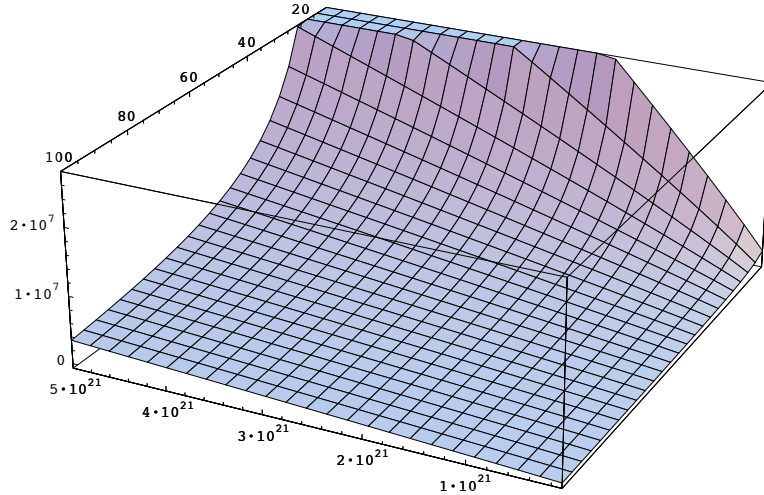
Figure A.1: Collision frequency as a function of density and ion temperature at SSX. The horizontal axis is plasma density in units of m^{-3}, and the axis running into the page is the ion temperature in eV.

A.2 The Collision Frequency at SSX

We have used A.8 to compute the collision frequency at SSX. From [2], the Coulomb logarithm in our plasma should be approximately $\ln \Lambda \sim 10$. We were able to better estimate the Coulomb logarithm from a formula given on p. 35 of the *NRL Plasma Formulary* for mixed ion-ion collisions [66]. That equation was

$$\ln \Lambda = 23 - \ln \left[\frac{ZZ'(\mu + \mu')}{\mu kT' + \mu' kT} \left(\frac{nZ^2}{kT} + \frac{n'Z'^2}{kT'} \right)^{1/2} \right] \tag{A.9}$$

Here the primed and unprimed variables refer to the two species of colliding ions, and μ is the mass of the ions in units of the proton mass. In performing our calculations, we made a conservative estimate of the collision frequency by overcalculating the Coulomb logarithm. In particular, we assumed that the densities of the impurity and majority ions were equal, when this was certainly not the case. This still should not have affected the Coulomb logarithm by more than a factor of order unity.

For $n_i = 10^{15}$ cm^{-3} and $T_i = 30$ eV, we found $\nu = 3.85 \times 10^6$ s^{-1}. This means the collisions are occurring several times faster than the 1 μs timescale we are observing at, and also faster than the Alfvén time in the plasma, $\tau = v_A/L \sim 2$ μs.

Finally, we plot the collision frequency as a function of density and temperature in Fig. A.1. As seen from the plot, the frequency does drop sharply with increased temperature and decreased density. Thus there may be some cause for concern as the GDC decreases the plasma density and increases the temperature.

71

Appendix B

Broadening in the IDS System

In this thesis we have been discussing an optical diagnostic that measures ion temperature from the width of an impurity spectral line. Recall the derivation in Chapter 3 of the Doppler broadening due to temperature. Is Doppler broadening the primary cause of broadening in the C III line we are diagnosing, or are other effects of comparable importance? Here we address this question by discussing several other broadening mechanisms and showing that they are negligible. The reader interested in further information about mechanisms of spectral line broadening is referred to the excellent discussion in Hutchinson [61] and to the book by Griem [67]. Throughout this appendix, recall that the expected minimum Doppler broadening is $\Delta\lambda/\lambda = 4 \times 10^{-5}$, as described in Section 3.1.

B.1 Natural Broadening

Atomic states tend to have finite lifetimes. As a consequence, atomic transitions occur; it is such a transition that gives rise to the C III line we observe with the IDS. But, from the energy-time uncertainty principle

$$\Delta E \Delta t \geq \frac{\hbar}{2} \tag{B.1}$$

in quantum mechanics, a state with a finite lifetime does not have a definite energy[1]. According to Hutchinson, the relevant lifetime τ for a spectral line that arises from a transition from a given upper atomic level i is

$$\frac{1}{\tau} = \frac{1}{2}\Sigma_j A_{ij} \tag{B.2}$$

Here, the A_{ij} are Einstein A coefficients for radiative transition from state i to a lower state j, and the summation is over all lower states that an atom in state i can transition to. Now, since $E = \hbar\Delta\omega$, we find that

$$\Delta\omega = \frac{1}{2\tau} \tag{B.3}$$

Using the fact that $\Delta\omega/\omega \approx \Delta\lambda/\lambda$ for small differences, and that $\omega = 2\pi c/\lambda$, we find

$$\Delta\lambda = \frac{\lambda^2}{4\pi c\tau} \tag{B.4}$$

---

[1]We note that the energy-time uncertainty principle is different from that governing non-commuting operators, time not being an operator in quantum mechanics.

Then, using (B.2), it follows that the spread in wavelength due to natural broadening is given by

$$\Delta\lambda = \frac{\lambda^2}{8\pi c}\Sigma_j A_{ij} \tag{B.5}$$

A search of the *NIST Atomic Spectra Database* at

`http://physics.nist.gov/cgi-bin/AtData/main_asd`

for all the spectral lines of C III that involve a transition to the $2s(^2S)2p$ level, including the 229.687 nm line of interest, revealed 109 lines. Surely, not all of these lines contribute to the width of the actual line of interest, but nonetheless this provides a conservative estimate. For these 109 lines, we found $\Sigma A_{ij} = 9.07 \times 10^{10}$ s^{-1}. Substituting this value into (B.5) gives $\Delta\lambda/\lambda = 2.76 \times 10^{-6}$ for the C III 229.687 nm line. This is an order of magnitude below the expected Doppler broadening and is thus negligible.

B.2 Pressure Broadening

The Stark effect occurs when an external electric field perturbs the energy levels of some atom, generally causing the energy levels to be raised as well as spreading out formerly degenerate levels. The Stark effect is treated in most introductory textbooks on quantum mechanics, such as Shankar [68]. In a plasma, while there are in general no large-scale electrostatic fields, the electric fields of other charged elements in the plasma can affect the energy levels of a radiating impurity ion. In a plasma, the Stark effect causes some spread in energy that broadens a spectral line. This broadening is known as Stark broadening and is usually lumped with a number of other effects which are collectively known as pressure broadening. These other effects include resonance broadening, due to the radiator's interactions with neutral atoms, and van der Waals broadening, due to interactions with other atoms, but the Stark broadening dominates these effects in most plasmas [69].

In general, the theory of Stark broadening is very complicated, and even a qualitative discussion of such calculations is beyond the scope of this thesis. The interested reader is referred to Hutchinson [61] for a useful summary of the theory, as well as to the books by Griem on this subject [69, 67]. It turns out that detailed calculations of Stark broadening have been done for a few, mostly hydrogenic, atoms and ions. Some empirical formulae for extending known Stark calculations to heavier atoms have been formulated, but are not valid for the plasma parameters in SSX [70].

Even so, we can proceed to make an estimate of the Stark broadening. Griem [69] has calculated Stark broadening for He II. The Stark width $\Delta\lambda_S$ is given by

$$\Delta\lambda_S = \left(\frac{n_e}{C(n_e, T)}\right)^{2/3} \tag{B.6}$$

(see Eqn. 14-8 of [69]). Here n_e is the electron density and $C(n_e, T)$ is a parameter dependent on the density and plasma temperature which is the main result of the Stark calculations. For the He II line at 468.6 nm, for $T = 80,000$ K and $n_e = 10^{17}$ cm^{-3}, Table 14-8 gives $C(n_e, T) = 1.65 \times 10^{16}$ Å$^{-3/2}$cm^{-3};

these listed parameters most closely match the SSX plasma. From this, given the actual density $n_e \approx 10^{-14}$ cm^{-3} in SSX, we find from (B.6) that $\Delta\lambda_S = 3.32 \times 10^{-2}$ Å. For a line of wavelength 229.687 nm, this gives $\Delta\lambda_S/\lambda \approx 1 \times 10^{-5}$. This is smaller than the expected Doppler broadening.

Our estimate here is probably a gross overestimate, however. First of all, the calculation was for a singly ionized helium line, and lines from multiply ionized atoms exhibit less Stark broadening [69]. Ions of greater charge would tend to further repel oppositely charged particles, and would thus experience smaller electric fields due to those charged particles. Moreover, the Stark coefficients $C(n_e, T)$ generally increase with increasing temperature, leading to a decreased broadening. This too makes physical sense; as we found in Appendix A, increasing plasma temperatures tend to decrease the frequency of Coulomb collisions, and thus would probably decrease the frequency and strength of perturbing interactions giving rise to Stark broadening. From this, we can thus conclude that pressure broadening for the C III 229.687 nm line in SSX should be negligible.

B.3 Zeeman Broadening

The Zeeman effect, like the Stark effect, spreads out energy levels in an atom, but due to a magnetic field. Similarly, the Zeeman effect can give rise to the Zeeman broadening of a spectral line in a plasma. Griem finds that for lines from hydrogenic ions, the minimum magnetic field B_c for which magnetic effects become comparable to Doppler broadening is given by

$$B_c \geq \left(\frac{m_e kT}{2 m_r E_H} \right)^{1/2} Z^2 \frac{n_i + n_f}{n_i^2 n_f^2} \frac{e}{a_0^2} \tag{B.7}$$

(see Eq. 411 of [67]). Here m_e is the electron mass, m_r is the radiator mass, E_H is the ground state energy of hydrogen (13.6 eV), n_i and n_f are the principal quantum numbers of the initial and final levels of the transition, and a_0 is the Bohr radius. C III is not hydrogenic, but this formula should still be useful for estimation. For $kT \approx 20$ eV at SSX, and for $n_i = n_f = 2$ for the C III 229.687 nm line, we find from (B.7) that $B_c \geq 9.9 \times 10^4$ G. Since the magnetic fields at SSX are about 1 kG, they are almost two orders of magnitude below the critical field. Thus, Zeeman effects should be negligible as well.

Appendix C

Atmospheric Effects on the Index of Refraction

C.1 The Index of Refraction of Air

In any medium other than a vacuum, light propagates not at speed c but at speed c/n, where n is the index of refraction. For this reason, if a source is generating electromagnetic radiation at frequency ν, the wavelength of the radiation will be given by λ_0/n, where λ_0 is the vacuum wavelength.

Since ion flow measurements in the IDS system under construction at SSX depend on observations of the plasma along a single line of sight, an absolute wavelength calibration is necessary. If changes in the index of refraction due to fluctuations in the temperature, pressure, or relative humidity of the laboratory air sufficiently affect the wavelength of the light emitted from the plasma, erroneous measurements of flow would therefore result. Thus it behooves us to at least estimate the magnitude of these effects to determine whether they will need to be accounted for. We note that the current dispersion D of the spectrometer is 0.032 nm/mm. Our PMT array has pixels 1 mm wide, but exit optics magnify the spectrometer output by a factor of 4. Thus we should be concerned if atmospheric fluctuations cause the wavelength to change by 0.008 nm or more.

We do not attempt to compute n in air from first principles. Two different equations have been computed: the Edlen equation and the Ciddor equation. Both, however, are difficult to use. A more thorough discussion of these equations may be found at on the NIST website at

`http://emtoolbox.nist.gov/Wavelength/Documentation.asp`

In this discussion we use the results in the *CRC Handbook*, computed from the Edlen equation [71]. There, results are given for $(n-1) \times 10^8$ in dry air at 15 °C and 101.325 kPa, containing 0.045% CO_2 by volume. At other temperatures and pressures, the tabulated values are to be multiplied by

$$\frac{p[1 + p(60.1 - 0.972t) \times 10^{-10}]}{96095.43(1 + 0.003661t)} \tag{C.1}$$

where t is in °C and p is in Pa. We may thus use this result to examine the effects of pressure and temperature.

To approximately consider the effects of relative humidity, we make use of the shop-floor formula given in the NIST documentation. For p in kPa, t in Celsius, and relative humidity RH, the approximate index of refraction is

$$n = 1 + \frac{7.86 \times 10^{-4} p}{273 + t} - 1.5 \times 10^{-11} RH(t^2 + 160) \tag{C.2}$$

Using this, we account for relative humidity.

C.2 Pressure Effects

If we define $X \equiv (n - 1) \times 10^8$, we can use the Chain Rule to get

$$\frac{d\lambda}{dp} = \frac{d\lambda}{dn} \frac{dn}{dX} \frac{dX}{dp} \tag{C.3}$$

Assuming that the pressure in the lab is 1 atm (101.325 kPa), the temperature is 20 °C, and that we are looking at 230 nm light ($\sim$ 229.7 nm), we find that $n = 1.0003027$ and that

$$\frac{d\lambda}{dp} = -6.8733 \times 10^{-7} \text{ nm/Pa.} \tag{C.4}$$

So, if we expect fluctuations on the order of 3 inches of mercury, or approximately 10 kPa, we can estimate

$$\Delta\lambda = \frac{d\lambda}{dp} \Delta p = 6.8733 \times 10^{-3} \text{ nm} \tag{C.5}$$

Such a dramatic pressure variation is unlikely, except in the event of very severe weather such as a hurricane. We conclude from this that the effect of pressure fluctuations should be less than our resolution.

C.3 Temperature Effects

In a similar way we can account for temperature variations. At the same conditions as listed above, we find

$$\frac{d\lambda}{dt} = 2.3807 \times 10^{-4} \text{ nm/°C} \tag{C.6}$$

So, if we estimate lab temperature fluctuations to be about 10 °C, or 18 °F, which is a conservatively large estimate, we find $\Delta\lambda = 0.00238$ nm.

C.4 Humidity Effects

We use the shop-floor formula given by NIST as described in §1. Then,

$$\frac{d\lambda}{dRH} = \frac{\lambda_0}{n^2} \cdot 1.5 \times 10^{-11}(t^2 + 160) \tag{C.7}$$

Making an order of magnitude estimation, the term involving λ_0 is of order 10^2. Suppose also that $t^2 + 160 \approx 5 \times 10^2$. Then we find $\frac{d\lambda}{dRH} \approx 10^{-6}$ nm/%RH. Clearly, this is negligible.

We confirm this using the NIST index of refraction Edlen equation calculator, at the webpage previously listed. At 300 nm, 20 °C, and 1 atm, an increase in the relative humidity from 0% to 100% increased the wavelength by 0.00023 nm, which is consistent with our estimate.

C.5   Conclusions

In conclusions, we find that the atmospheric effect which is most likely to disturb our measurements is pressure, followed by temperature. As long as the pressure in the lab remains fairly constant, we should have no problems. We have not, however, considered the possibility of simultaneous changes in temperature and pressure, in which case the changes in n due to each could be additive.

Appendix D

Codes for Abel Inversion

We exhibit the main codes used for the Abel inversion described in Ch. 5. The main code is `masterabel2.pro`:

```
; Jerome Fung
; 2/21/06

pro masterabel2, rundate, bintime, saveout = saveout

; compute number of rows
nelts = 200 ; data count starts 20 us before t = 0
bintime = float(bintime) ; just to be safe
nrows = floor(nelts/bintime)
nchords = 10.0
d = 1/nchords

; obtain file names
bintimestr = strtrim(string(floor(bintime)), 2)
impfilename = './output/'+rundate+'/abelinput'+bintimestr+'.dat'
stdfilename = './output/'+rundate+'/abelstdev'+bintimestr+'.dat'

abeldata = fltarr(nchords, nrows)
abelstds = fltarr(nchords, nrows)
abelresult = fltarr(nchords, nrows)
abelreserr = fltarr(nchords, nrows)
rundate2 = ''

; read input from abelbinner.pro

openr, lun, impfilename, /get_lun
    readf, lun, rundate2 ; get the run date (not needed now)
    readf, lun, abeldata
free_lun, lun

openr, lun, stdfilename, /get_lun
    readf, lun, rundate2 ; get the run date (not needed now)
    readf, lun, abelstds
free_lun, lun

print, 'Data read in'
timebase = findgen(nrows)*bintime - 20
```

```
; Calculate Abel inversion matrix
S = abelinvmatrix(nchords)
sinv = invert(s)
sinv2 = sinv^2


; *OPEN GREAT LOOP*

for maincount = 0, nrows -1 do begin
    print, 'Analyzing t = ', timebase[maincount]
    abelinput = abeldata[*, maincount]
    abelinstd = abelstds[*, maincount]
    abelinstd2= abelinstd^2
    abelresult[*, maincount] = (d/2.0)*sinv##abelinput ; doing the inversion
    abelreserr[*, maincount] = sqrt((d^2/4.0)*sinv2##abelinstd2)
endfor

; *CLOSE GREAT LOOP*

; write the output
if keyword_set(saveout) then begin

    outfilename = './output/'+rundate+'/abelresult'+bintimestr+'.dat'
    outerrsname = './output/'+rundate+'/abelerrors'+bintimestr+'.dat'

    openw, lun, outfilename, /get_lun
        printf, lun, rundate
        printf, lun, nrows
        printf, lun, bintime
        printf, lun, abelresult
    free_lun, lun

    openw, lun, outerrsname, /get_lun
        printf, lun, rundate
        printf, lun, nrows
        printf, lun, bintime
        printf, lun, abelreserr
    free_lun, lun

endif


end
```

Function called by above code to calculate the matrix $[S]$ of Equation (5.7): `abelinvmatrix`

```
function abelinvmatrix, dim

; calculates abel inversion matrix according to Cho/Na paper

d = 1 / float(dim)

; first calculate theta_ij and p_ij according to eqns. 8 and 9
; Recall that IDL convention for matrices [col, row].
```

```
; Set up n x n matrices
theta = double(fltarr(dim, dim))
p     = fltarr(dim, dim)
s     = fltarr(dim, dim)

; double loop to calculate theta and p
for i = 0, dim-1 do begin
    for j = 0, dim-1 do begin
        if i le j then begin
            theta[j,i] = acos( i / (j+1.0))
            if i ne 0.0 then begin
             p[j,i]      = (1/2.0)*((j+1)*d)^2*theta[j,i] - $
                 (1/2.0)*(i*d)^2*tan(theta[j,i])
            endif else begin ; account for i = 1 case
             p[j,i] = (1/2.0)*((j+1)*d)^2*theta[j,i]
            endelse
        endif else begin
            theta[j,i] = 0
            p[j,i]     = 0
        endelse
    endfor
endfor

; double loop to calculate S_ij now (eqn. 10)
for i = 0, dim-1 do begin
    for j = 0, dim-1 do begin
        if i le j then begin
            if (i lt (dim-1)) AND (j gt 0.0) then begin
                s[j,i] = (p[j,i]-p[j,i+1]) - (p[j-1,i]-p[j-1,i+1])
            endif
            if (j eq 0.0) then begin ; these two cases at boundaries of matrix
                s[j,i] = p[j,i]-p[j,i+1]
            endif
            if (i eq dim-1) then begin
                s[j,i] = p[j,i] - p[j-1,i]
            endif
        endif else begin
            s[j,i] = 0
        endelse
    endfor
endfor

return, s

end
```

Acknowledgements

I would first like to thank my advisor, Prof. Michael Brown, for all his guidance over two summers of research at SSX and in the writing of this thesis. I am also greatly indebted to SSX postdoctoral researcher Dr. Christopher Cothran for his guidance and especially for his patience in teaching me a great deal about plasmas, optics, and experimental physics in general. It has been a pleasure and honor to work with Mike and Chris during my undergraduate career at Swarthmore. I would also like to thank Prof. Carl Grossman for taking the time to critically read this thesis.

I also would like to thank Steve Palmer, whose advice and assistance in machining a number of parts for the IDS was important. Thanks also to Jim Haldeman for his advice and his generosity with equipment. My thanks also go to our collaborator Dr. Michael Schaffer of General Atomics, whose profound plasma experience and physical insight I benefited from.

I would also like to thank my fellow SSX'ers during Summer 2005 – Marc Chang, Jason Horwitz, Victoria Swisher, and Brie Coellner – for making the lab a pleasant and convivial place. I am particularly grateful to Marc Chang for his diligent work in upgrading our data acquisition software. I am also indebted to the previous SSX'ers upon whose work my own has built, in particular Aongus Ó Murchadha, who performed preliminary work with the IDS system.

I also want to thank the entire Department of Physics & Astronomy at Swarthmore College for a very fulfilling four years. I cannot begin to express my appreciation of the diligence and patience of the faculty in the courses and seminars I have had here. I would like to thank Prof. Peter Collings in particular for being a fabulous advisor during my freshman and sophomore years. My thanks also to my classmates in physics, from whom I have learned a great deal. Over the years I've also benefited a great deal from advice from various physics alums, including Matt Landreman '03, Robin Smith '03, and Rachel Sapiro '04.

On a personal note, I would like to thank my parents for their encouragement of my efforts. My thanks also to my friends at Swarthmore, especially to Blake Setlow for teaching me LaTeX, and to Jillian Waldman and Bethany Ziss for their constant support. Finally, I would like to thank the members and officers of the Swarthmore Fire & Protective Association for all they have taught me; it has been a privilege to serve with Company 14 during my time at Swarthmore.

Bibliography

[1] F. F. Chen, *Introduction to Plasma Physics and Controlled Fusion*, Plenum Press, New York, second edition, 1984.

[2] R. J. Goldston and P. H. Rutherford, *Introduction to Plasma Physics*, Institute of Physics Publishing, Philadelphia, 1995.

[3] D. A. Gurnett and A. Bhattacharjee, *Introduction to Plasma Physics: With Space and Laboratory Applications*, Cambridge UP, 2005.

[4] M. Landreman, *The Three-Dimensional Structure of Magnetic Reconnection in SSX*, Senior honors thesis, Swarthmore College, 2003.

[5] C. Cothran, M. Landreman, M. Brown, and W. Matthaeus, Geophys. Res. Lett. **30**, 1213 (2003).

[6] H. Isobe et al., Astrophys. J. **566**, 528 (2002).

[7] H. Isobe, H. Takasaki, and K. Shibata, Astrophys. J. **632**, 1184 (2005).

[8] M. Brown, C. Cothran, and J. Fung, Phys. Plasmas , In press (2006).

[9] M. G. Kivelson and C. T. Russell, editors, *Introduction to Space Physics*, Cambridge UP, 1995.

[10] Z. Mikik, D. D. Schnack, and G. V. Hoven, Astrophys. J. **338**, 1148 (1989).

[11] E. R. Priest, A. Hood, and U. Anzer, Astrophys. J. **344**, 1010 (1989).

[12] D. E. Innes et al., Nature **386**, 811 (1997).

[13] D. E. Innes, P. Brekke, D. Germerott, and K. Wilhelm, Solar Physics **175**, 341 (1997).

[14] R. Stenzel and W. Gekelman, J. Geophys. Res. **86**, 649 (1981).

[15] R. Stenzel and W. Gekelman, Phys. Rev. Lett. **42**, 1055 (1979).

[16] M. Yamada, Y. Ono, A. Hayakawa, M. Katsurai, and F. Perkins, Phys. Rev. Lett. **65**, 721 (1990).

[17] Y. Ono, A. Morita, and M. Katsurai, Phys. Fluids B **5**, 3691 (1993).

[18] Y. Ono, M. Inomoto, T. Okazaki, and Y. Ueda, Phys. Plasmas **4**, 1953 (1997).

[19] Y. Ono, T. Matsuyama, K. Umeda, and E. Kawamori, Nucl. Fusion **43**, 649 (2003).

[20] M. Yamada et al., Phys. Plasmas **4**, 1936 (1997).

[21] H. Ji et al., Phys. Rev. Lett. **80**, 3256 (1998).

[22] H. Ji et al., Physics of Plasmas **6**, 1743 (1999).

[23] S. Hsu et al., Phys. Rev. Lett. **84**, 3859 (2000).

[24] S. Hsu et al., Phys. Plasmas **8**, 1916 (2001).

[25] M. Yamada, Earth Planets Space **53**, 509 (2001).

[26] S. C. Hsu, *Experimental Study of Ion Heating and Acceleration during Magnetic Reconnection*, PhD thesis, Princeton University, 2000.

[27] G. Fiksel, D. den Hartog, and P. Fontana, Rev. Sci. Instrum. **69**, 2024 (1998).

[28] Y. Ren et al., Phys. Rev. Lett. **95**, 055003 (2005).

[29] E. Priest and T. Forbes, *Magnetic Reconnection: MHD Theory and Applications*, Cambridge UP, 2000.

[30] J. Gafert et al., Plasma Phys. Control. Fusion **39**, 1981 (1997).

[31] S. Morita and M. Goto, Rev. Sci. Instrum. **74**, 2375 (2003).

[32] J. Rice, E. Marmar, F. Bombarda, and L. Qu, Nucl. Fusion **37**, 421 (1997).

[33] D. den Hartog and R. Fonck, Rev. Sci. Instrum. **65**, 3238 (1994).

[34] H. McLean et al., Rev. Sci. Instrum. **72**, 556 (2001).

[35] J.Ghosh et al., Phys. Plasmas **11**, 3813 (2004).

[36] U. Shumlak et al., Phys. Rev. Lett. **87**, 205005 (2001).

[37] D. den Hartog and R. Gollingo, Rev. Sci. Instrum. **72**, 2224 (2001).

[38] D. J. Griffiths, *Introduction to Electrodynamics*, Prentice Hall, Upper Saddle River, third edition, 1999.

[39] J. Lyman Spitzer and R. Härm, Phys. Rev. **7**, 509 (1953).

[40] P. M. Bellan, *Spheromaks*, Imperial College Press, 2000.

[41] E. Priest and T. Forbes, *Magnetic Reconnection: MHD Theory and Applications*, Cambridge UP, 2000.

[42] E. N. Parker, J. Geophys. Res. **62**, 509 (1957).

[43] R. M. Kulsrud, Earth Planets Space **53**, 417 (2001).

[44] J. Birn et al., Geophysical Research Letters **32**, L06105 (2005).

[45] C. Geddes, *Spheromak Equilibrium Studies on SSX*, Senior honors thesis, Swarthmore College, 1997.

[46] J. B. Taylor, Rev. Mod. Phys. **58**, 741 (1986).

[47] S. T. Thornton and J. B. Marion, *Classical Dynamics of Particles and Systems*, Thomson Brooks-Cole, Belmont, fifth edition, 2004.

[48] F. Reif, *Fundamentals of Statistical and Thermal Physics*, McGraw-Hill, New York, 1995.

[49] C. Palmer and E. Loewen, *Diffraction Grating Handbook*, Newport, sixth edition, 2005.

[50] R. Engstrom, *RCA Photomultiplier Handbook*, RCA, 1980.

[51] A. O. Murchadha, *Ion Temperature and Flow Velocity Measurements in SSX-FRC*, Senior honors thesis, Swarthmore College, 2005.

[52] T. Gray, *Density studies on SSX*, Senior honors thesis, Swarthmore College, 2001.

[53] A. Falk, *Dynamics of field-reversed configuration in SSX*, Senior honors thesis, Swarthmore College, 2003.

[54] C. Geddes, T. Kornack, and M. Brown, Phys. Plasmas **5**, 1027 (1998).

[55] W. Turner et al., Phys. Fluids **26**, 1965 (1983).

[56] T. Kornack, P. Sollins, and M. Brown, Phys. Rev. E **58**, R36 (1998).

[57] M. Brown, Phys. Plasmas **6**, 1717 (1999).

[58] M. Landreman, C. Cothran, M. Brown, M. Kostora, and J. Slough, Rev. Sci. Instrum. **74**, 1965 (2361-2368).

[59] M. Brown et al., Phys. Plasmas **9**, 2077 (2002).

[60] C. Cothran et al., Phys. Plasmas **10**, 1748 (2003).

[61] I. H. Hutchinson, *Principles of Plasma Diagnostics*, Cambridge UP, second edition, 2002.

[62] K. Bockasten, J. Opt. Soc. Am. **51**, 943 (1961).

[63] M. Deutsch and I. Beniaminy, J. Appl. Phys. **54**, 137 (1982).

[64] C. Maldonado, A. Caron, and H. Olsen, J. Opt. Soc. Am. **55**, 1247 (1965).

[65] Y. Cho and S.-J. Na, Measurement Science and Technology **16**, 878 (2005).

[66] J. Huba, *NRL Plasma Formulary*, Naval Research Laboratory, 2002.

[67] H. R. Griem, *Spectral Line Broadening by Plasmas*, Academic Press, 1974.

[68] R. Shankar, *Principles of Quantum Mechanics*, Kluwer Academic/Plenum Press, second edition, 1994.

[69] H. R. Griem, *Plasma Spectroscopy*, McGraw-Hill, 1974.

[70] R. Lee, J. Appl. Phys. **58**, 612 (1985).

[71] D. R. Lide, editor, *CRC Handbook of Chemistry and Physics*, CRC Press, 85th edition, 2005.